YBa$_2$Cu$_3$O$_x$ Josephson junctions on a bicrystal sapphire substrate for devices in the millimeter and submillimeter wavelength ranges

A. D. Mashtakov, K. I. Konstantinyan, G. A. Ovsyannikov, and E. A. Stepantsov

Institute of Radio Engineering and Electronics, Russian Academy of Sciences, Moscow
(Submitted September 1, 1998)
Pis'ma Zh. Tekh. Fiz. **25**, 1–8 (April 12, 1999)

High-temperature superconducting Josephson junctions on bicrystal sapphire substrates were fabricated and investigated experimentally. The critical parameters of the junctions satisfy the constraints for the design of devices in the millimeter and submillimeter wavelength ranges. The results of dynamic measurements show that in these junctions the superconducting current exhibits a sinusoidal dependence on the phase difference of the superconducting wave functions of the electrodes, and a simple resistive model is used to analyze their microwave properties. At the same time, the temperature dependence of the critical current of the junctions differs appreciably from that typical of tunnel junctions with s-superconductors and may be explained as d-type pairing of the superconducting electrodes and an SNS junction. © *1999 American Institute of Physics.* [S1063-7850(99)00104-4]

Josephson junctions fabricated using high-temperature superconductors (HTSCs) at liquid-helium temperature $T=4.2$ K have various parameters appreciably superior to those of their low-temperature analogs. These include the normal-state resistance R_N, the critical frequency $f_C = \Phi_0 I_C R_N$, where Φ_0 is the magnetic flux quantum and I_C is the critical current, and the capacitance C. For comparison we note that for niobium Josephson junctions with $f_C \cong 600$ GHz, $R_N \cong 10–30\,\Omega$, and McCumber parameter $\beta_C = 2\pi f_C R_N C \approx 1$, which characterizes the junction capacitance C on which the profile of the current–voltage characteristic and thus the presence or absence of hysteresis depend, estimates[1] indicate that shunted Josephson junctions of submicron dimensions $S \approx 0.1\,\mu\mathrm{m}^2$ must be fabricated with a critical current density $j_C \geq 10^4$ A/cm^2, which is extremely difficult to achieve even with the well-developed technology for fabricating niobium tunnel junctions. The absence of hysteresis on the current–voltage characteristics of HTSC Josephson junctions eliminates the need for shunting, and the potentially high values of f_C allow these junctions to be used at frequencies higher than the niobium gap.

However, aspects involved in the stable fabrication of high-quality HTSC Josephson junctions have not yet been resolved. The most reproducible junctions having a critical current spread of $\pm 12\%$ per chip are fabricated on SrTiO$_3$ bicrystal substrates,[2] but because of their high permittivity $\varepsilon > 1000$ they are unsuitable for microwave applications. Single-crystal sapphire having a relatively low permittivity $\varepsilon \approx 9.5$ (parallel to the principal crystallographic axis) and low losses (tan $\delta \approx 10^{-8}$ at 72 GHz and $T=4$ K) (Ref. 3), which is the traditional material used in microwave electronics, is one of the most promising substrate materials. Vale *et al.*[2] and Kunkel *et al.*[4] reported YBa$_2$Cu$_3$O$_x$ (YBCO) Josephson junctions on sapphire bicrystals, although the literature contains no information on the correspondence between the parameters obtained from static data on the current–voltage characteristics and those obtained from dynamic measurements nor on the noise parameters, which are particularly important for applications in sensitive detectors in the millimeter and submillimeter wavelength ranges. Here we report the fabrication and measurements of the dynamic parameters of Josephson junctions consisting of YBCO films on bicrystal sapphire substrates having the parameters $f_C = 300–700$ GHz, $R_N \cong 10–30\,\Omega$, and $\beta_C \approx 1$ at $T=4.2$ K.

The Josephson junctions were fabricated on the $(1\underline{1}02)$ plane of sapphire substrates consisting of two crystals for which the $\langle 11\underline{2}0 \rangle$ directions were at angles of $\pm 12°$ to the plane of the interface. The YBCO film was fabricated by first depositing a 40–80 nm thick CeO$_2$ epitaxial buffer layer by rf magnetron sputtering from a metallic Ce target at 750 °C in order to prevent Al atoms from diffusing into the YBCO film. The CeO$_2$ buffer layer was deposited at a pressure of 1.2 Pa in an Ar–O$_2$ gas mixture with a partial pressure ratio of 1:1. A YBCO epitaxial film was deposited on the CeO$_2$ surface by diode sputtering in a dc discharge at a high oxygen pressure of 4×10^2 Pa (Ref. 5). A 50 nm thick YBCO lower layer was then deposited at a lower substrate surface temperature of 725 °C to prevent chemical interaction between the YBCO and the CeO$_2$ (Ref. 5). The 100 nm-thick main upper YBCO layer was deposited at a substrate surface temperature of 780 °C which improved the structure of the film and its superconducting properties. The films were cooled for 1 h in an O$_2$ atmosphere and then coated with a 100 nm polycrystalline CeO$_2$ layer which acts as a mask for the subsequent technological processes. Thin-film YBCO bridges 5 μm wide and 10 μm long crossing the bicrystal interface were initially formed in the upper CeO$_2$ layer by rf plasma etching in Ar and the YBCO was then subjected to liquid chemical etching in a 0.5% ethanol solution of Br$_2$ through the CeO$_2$ mask.

Figure 1 shows typical temperature dependences of the
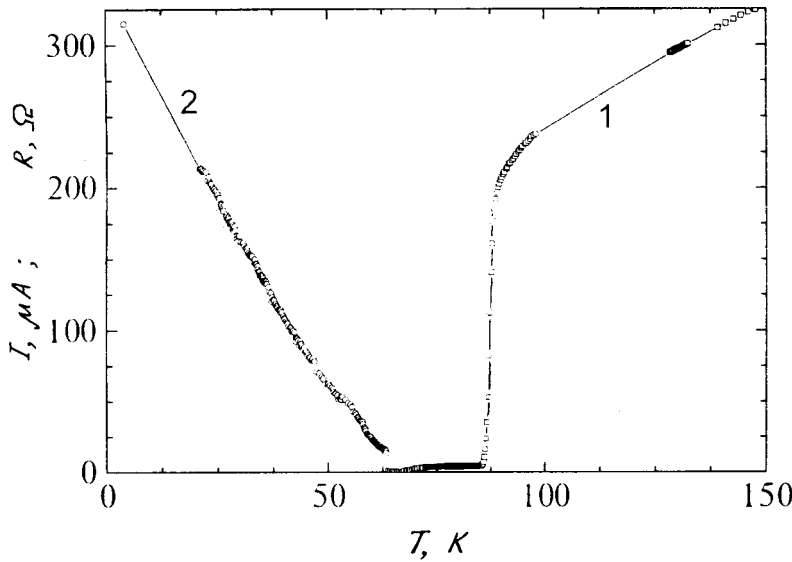
FIG. 1. Temperature dependence of the resistance $R(T)$ (1) and critical current $I_C(T)$ (2) for a YBCO Josephson junction on the (1$\underline{1}$02) plane of a sapphire bicrystal with a misorientation angle of 24°.

resistance of the Josephson junction $R(T)$ and the critical current $I_C(T)$. It can be seen that at low temperatures a nearly linear dependence $I_C(T)$ is observed, which differs appreciably from the known theoretical dependence for superconductor–insulator–superconductor (SIS) tunnel junctions but is similar to that calculated by Tanaka and Kashiwaya[6] for Josephson junctions fabricated using d-type pairing superconductors with an infinitely narrow barrier and a misorientation angle close to the experimental value. It should be noted that for $T \ll T_C$ an almost linear dependence $I_C(T)$ is observed for SNS Josephson junctions where N is a normal metal.[7]

The results of measurements of the static parameters of the samples at $T = 4.2$ K are presented in Table I. The thickness of the CeO_2 buffer layer was 80 nm for series BC3 and 40 nm for series BC5. The structures of samples BC3-A and BC5-A consisted of chains of three Josephson junctions connected in parallel. The critical temperature of the YBCO film in the bridges was in the range $T_C \cong 86–88$ K. At $T \approx 77$ K a thermally activated phase slip process was caused by thermal fluctuations (the current amplitude of the fluctuations was $I_t = 4\pi k_B T/\Phi_0 \approx 6\,\mu$A), which broadened the current–voltage characteristic of the Josephson junction[8] and a non-zero critical current was observed at lower temperatures $T < 70$ K. The curve $R(T)$ shows a characteristic "shelf" in the range 86–67 K. At temperatures $T \sim T_C$ where thermal

fluctuations predominate, the approximated dependence $I_C(T)$ is closer to the quadratic dependence $I_C \sim (1 - T/T_C)^2$. This behavior of $I_C(T)$ near T_C may be observed both for s-superconductors and in Josephson junctions fabricated from d-type superconductors, as was predicted by Barash *et al.*[9] The departure of the HTSC electrodes from s-type pairing may be reflected in the functional dependence of the superconducting current I_S on the phase φ and thus in the appearance of a nonsteady-state Josephson effect, as was shown by Tanaka and Kashiwaya[6] and Barash *et al.*[9]

In order to estimate the dependence $I_S(\varphi)$, we measured the current–voltage characteristics of the Josephson junctions at temperatures between the critical temperature T_C and $T = 4.2$ K under the action of millimeter external electromagnetic radiation. Figure 2a shows a family of current–voltage characteristics for junction BC5-2 obtained for various powers P_e of the electromagnetic radiation. In this case, the amplitude of the critical current was suppressed by the action of the magnetic field which ensures that the frequencies are approximately equal $f_C \approx f_e \cong 100$ GHz. An analysis of the experimental dependences of the amplitudes I_C and the Shapiro steps I_n ($n=1,2,3$) on the power P_e (Fig. 2b) showed that the microwave dynamics of these Josephson junctions is accurately described by a simple resistive model.[7] Note that the value $f_C \cong 106$ GHz determined using an independent current–voltage characteristic was also close to its "microwave" analog determined using the maximum of the first Shapiro step $I_{1\,\text{max}}$, $f_{C1} \cong 90$ GHz, and from the zeros of the curves $I_n(P_e)$ (χ-criterion[7]), $f_{C\chi} \cong 100$ GHz. The frequency ratios f_C/f_{C1} for samples BC3-1 and BC5-1 were 337/345 and 330/335 GHz/GHz, respectively. The overall deviation of the frequency f_C from their microwave estimates was of order $\pm 5\%$.

Kleiner *et al.*[10] showed that the deviation of the curve $I_S(\varphi)$ from sinusoidal gives rise to subharmonic (fractional n/m) Shapiro steps whose amplitude is proportional to the corresponding harmonic of the Fourier expansion of $I_{S(\phi)}$ with respect to $\sin(n\phi)$. A detailed study of the current–voltage characteristics of the Josephson junctions, including

TABLE I. Junction parameters measured at liquid helium temperature $T = 4.2$ K. The notation is given in the text.

Sample	I_C, μA	R_N, Ω	$I_C R_N$, μV	f_C, GHz
BC3-1	93	7.5	697.5	337
BC3-2	100	13	1300	628
BC3-A*	100	13.5	1350	650
BC5-1	19	36	680	330
BC5-2	64.2	23	1496	723
BC5-A*	46.2	21.4	990	479

*Parameters for a single sample calculated from measurements of a chain of three parallel-connected junctions.
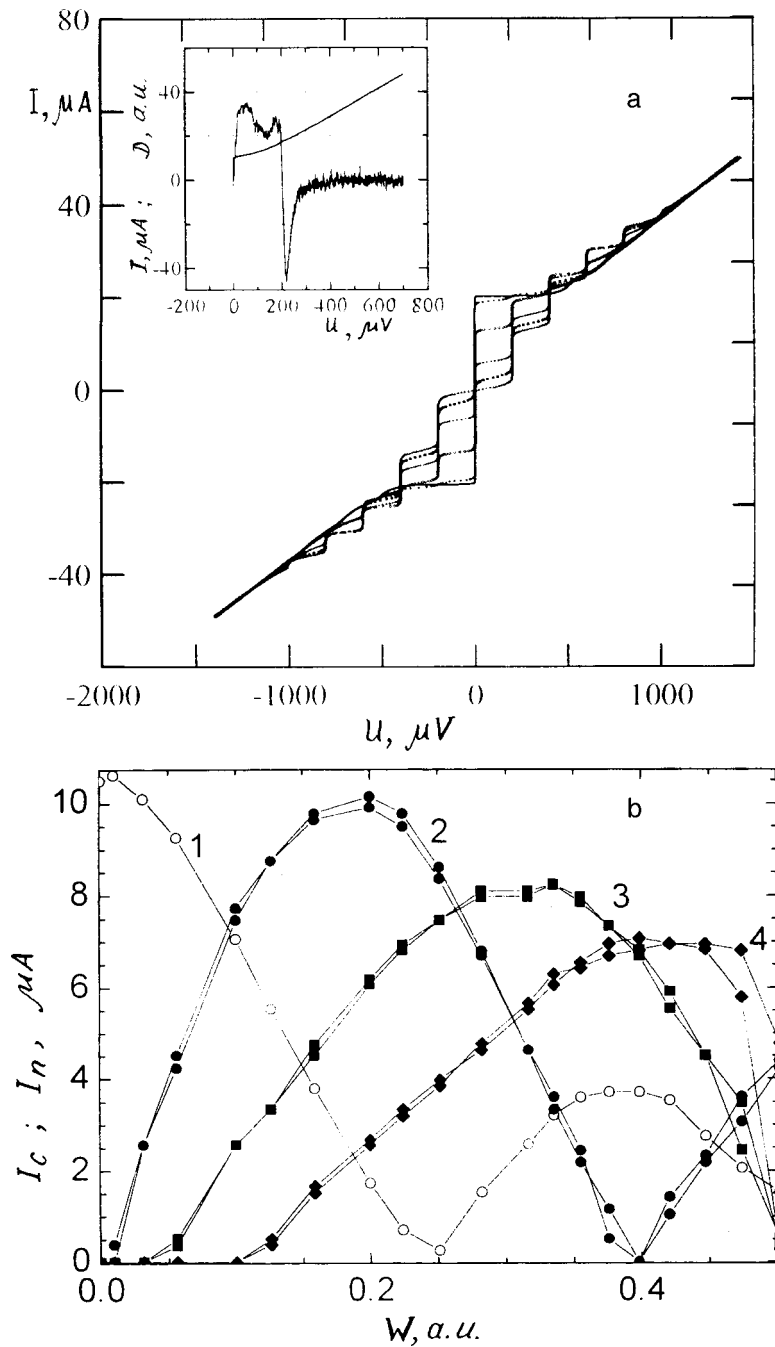
FIG. 2. Influence of microwave irradiation at power P_e and frequency $f_e \cong 100$ GHz on junction BC5-2 of width $w = 5$ μm, $R_N \cong 23$ Ω, and $I_C \cong 11$ μA (suppressed by the action of a weak static magnetic field) at $T = 4.2$ K: a—family of current–voltage characteristics at various power levels P_e (the inset shows the detector response of the Josephson junction (D) to a weak signal at the same frequency); b—power dependence of the critical current (1) and the amplitudes of the Shapiro steps $n = 1$ (2), $n = 2$ (3) and $n = 3$ (4) on the right and left branches of the current–voltage characteristic.

those at $T = 4.2$ K ($T/T_C \approx 0.05$), under the action of a microwave field reveals no $\sin(2f)$ and $\sin(nf)$ components in $I_S(\phi)$ to within 5%. Note that for the case of a Josephson junction fabricated of d-type superconductors calculated in Ref. 6, for which $I_C(T)$ is linear, the dependence $I_S(\phi) \approx \sin(\phi)$ is also predicted. We note that the appearance of subharmonics may also be caused by an inhomogeneous current distribution over the junction width[7,11] and/or by the high capacitance of the Josephson junction. In our case, the uniformity of the current distribution was also confirmed experimentally by the ''Fraunhofer'' dependence $I_C(H)$ and the absence of hysteresis on the current–voltage characteristic indicates the junction has a low capacitance C. Using the resistive Josephson junction model we estimate $\beta_C \approx 1$ and therefore $C = \varepsilon \varepsilon_0 S/t$ from the independent current–voltage

characteristic, where t is the thickness of the junction tunnel barrier and S is the area of the junction. We obtain $C \cong 13.5$ fF and the ratio $t/\varepsilon \approx 2.7$ Å. Note that this value of C agrees with the data given in the literature for other types of HTSC Josephson junction (see Ref. 12, for example) where C was estimated from the resonant Fiske characteristics in the tunnel junction model.

The noise properties of these samples were estimated by measuring (using a procedure similar to that described by Ovsyannikov *et al.*[13]) the line width Δf of the natural Josephson oscillation from the profile of the selective detector response $\eta(V)$ at 100 GHz. This dependence is shown in the inset to Fig. 2a. The values of $\Delta f \approx 15$ GHz were four times broader than the theoretical values predicted by the resistive

Mashtakov *et al.*

model. This line broadening has frequently been observed in the literature (see Refs. 4 and 13, for example). Note that for $V > 300\,\mu$V the curve $\eta(V)$ approaches zero. In this case, measurements of the noise response using a cryogenic low-noise amplifier at 1.5 GHz revealed a linearly dependent increase in the noise level as a function of the junction voltage caused by the presence of shot noise whose level, according to our estimates, was insufficient to explain the observed broadening of the oscillation line.

[1] V. N. Gubankov, K. I. Konstantinyan, and V. P. Koshelets, Zh. Tekh. Fiz. **53**, 1639 (1983) [Sov. Phys. Tech. Phys. **28**, 1009 (1983)].

[2] L. R. Vale, R. H. Ono, and D. A. Rudman, IEEE Trans. Appl. Supercond. **7**, 3193 (1997).

[3] V. B. Braginsky and V. S. Ilchenko, Phys. Lett. **120**, 300 (1987).

[4] G. Kunkel, G. Hechtfischer, M. Frommberger *et al.*, Tech. Phys. Lett. **7**, 3339 (1997).

[5] A. D. Mashtakov, I. M. Kotelyanskiĭ, V. A. Luzanov *et al.*, Pis'ma Zh. Tekh. Fiz. **23**(19), 8 (1997) [Tech. Phys. Lett. **23**, 738 (1997)].

[6] Y. Tanaka and S. Kashiwaya, Phys. Rev. B **56**, 892 (1997).

[7] K. K. Likharev and B. T. Ul'rikh, *Systems with Josephson Junctions* [in Russian], Moscow State University Press, Moscow (1978), 446 pp.

[8] C. L. Lin, W. J. Chang, M. Y. Li *et al.*, Physica C **269**, 291 (1996).

[9] Yu. S. Barash, A. V. Galaktionov, and A. D. Zaikin, Phys. Rev. B **52**, 665 (1995).

[10] R. Kleiner, A. S. Katz, A. G. Sun *et al.*, Phys. Rev. Lett. **76**, 2161 (1996).

[11] K. I. Konstantinyan, A. D. Mashtakov, G. A. Ovsyannikov *et al.*, Zh. Eksp. Teor. Fiz. **107**, 1742 (1995) [JETP **80**, 971 (1995)].

[12] H. R. Yi, D. Winkler, and T. Claeson, Appl. Phys. Lett. **66**, 1677 (1995).

[13] G. A. Ovsyannikov, A. D. Mashtakov, I. M. Kotelyanski *et al.*, in *Extended Abstracts of ISEC 97*, Germany, Vol. 2 (1997), p. 76.

Translated by R. M. Durham

Investigation of the growth characteristics of epitaxial GaN layers on sapphire by microcathodoluminescence

A. S. Usikov, V. V. Tret'yakov, V. V. Lundin, Yu. M. Zadiranov, B. V. Pushnyĭ, and S. G. Konnikov

A. F. Ioffe Physicotechnical Institute, Russian Academy of Sciences, St. Petersburg
(Submitted December 1, 1998)
Pis'ma Zh. Tekh. Fiz. **25**, 9–17 (April 12, 1999)

A study was made of the growth regimes of undoped epitaxial GaN layers under various substrate nitriding conditions. It was observed that at a nitriding temperature of $\sim 1000\,^{\circ}\mathrm{C}$ films are formed with typical growth characteristics in the form of hexagonal pyramids separated by a smoothed surface. The cathodoluminescence pattern in the pyramids revealed a fine structure in which a region of donor–acceptor recombination could be identified. The formation of acceptor levels in this region was attributed to intrinsic structural defects in the GaN layers with unsaturated (broken) bonds. The presence of a donor–acceptor recombination line in mirror-smooth epitaxial films may indicate that these films contain this type of structural defect. © *1999 American Institute of Physics.* [S1063-7850(99)00204-9]

INTRODUCTION

Gallium nitride and solid solutions based on group III nitrides are presently attracting considerable interest because of the possibility of developing optoelectronics devices operating in the visible and ultraviolet as well as devices for high-temperature electronics.[1] Despite the significant progress achieved in the manufacture and commercialization of this type of device,[2] more detailed studies of the properties of the as-grown material to improve the parameters of optoelectronics devices continue to remain the focus of attention among researchers.[3] In the present paper we study the spatial inhomogeneities of the microcathodoluminescence over area and thickness in epitaxial GaN layers grown on (0001) sapphire substrates.

EXPERIMENT

Gallium nitride layers were grown by vapor-phase epitaxy from metalorganic compounds.[4] The processes were carried out in an inductively heated horizontal reactor in a hydrogen stream at a reduced pressure of 200 mbar. The initial components were ammonia and trimethyl gallium. The epitaxial layers were intentionally not doped.

The growth procedure included treating the substrate surface in an ammonia stream at $500–1000\,^{\circ}\mathrm{C}$ to nitride the surface, depositing a thin buffer layer around 220 Å thick at a lower temperature ($\sim 510\,^{\circ}\mathrm{C}$), annealing the buffer layer, and then epitaxial growth of the main layer at high temperature ($\sim 1040\,^{\circ}\mathrm{C}$). Gallium nitride was used as the buffer layer. Typical growth rates and epitaxial layer thicknesses were $2.5–3\ \mu\mathrm{m/h}$ and $3–4\ \mu\mathrm{m}$, respectively. Depending on the nitriding temperature (T_n), the epitaxial layers either exhibited typical hexagonal growth pyramids (Fig. 1a) ($T_n \sim 1000\,^{\circ}\mathrm{C}$) or they were mirror-smooth ($T_1 \sim 500\,^{\circ}\mathrm{C}$).

The microcathodoluminescence was observed using a defocused electron beam of up to 200 μm diameter via the optical system of a Camebax microanalyzer. At $\times 800$ magnification and a probe current density of up to $\sim 200\ \mathrm{A/cm^2}$,

the resolution of the recording system was $\sim 1\ \mu\mathrm{m}$ and the microcathodoluminescence pattern was recorded on photographic film using a special attachment. The microcathodoluminescence spectra were obtained at room temperature and at liquid-nitrogen temperature. The electron probe energy was between 5 and 15 keV and the probe current was $\sim 5–100\ \mathrm{nA}$. The spectra were recorded using a grating monochromator with a dispersion of $\sim 2\ \mathrm{nm/mm}$ and a photon counting system.

The microcathodoluminescence distribution over the layer thickness was investigated using a method of layer-by-layer dry etching in a specialized Rokappa system. Etching regimes which did not give rise to defects revealed by the microcathodoluminescence were as follows: accelerating voltage of Ar gun 500 V, current density $\sim 0.5\ \mathrm{mA/cm^2}$, and sample temperature $25\,^{\circ}\mathrm{C}$. The samples were etched uniformly to a depth of $\sim 0.5–1\ \mu\mathrm{m}$ at a rate of 220 Å/min.

RESULTS AND DISCUSSION

Figure 1a shows an optical image of the surface of layers exhibiting hexagonal pyramids. Films with a similar surface morphology were obtained earlier and described by Akasaki *et al.*[5] However, our investigation revealed a spatial fine structure in the microcathodoluminescence image in the hexagonal pyramids (Fig. 1b) which may be described as follows. The yellow spot at the center of the pyramid was surrounded by a violet region which merged into pale blue at the edges. The spot at the center of the pyramid may be absent. In addition, small yellow (white) spots were observed at the boundary between the dark blue–violet and pale blue regions. A similar microcathodoluminescence pattern, but with a lower contrast and typical structural details almost twice as large, was observed on the smoothed surface between the pyramids.

The variation in the film structure with depth was investigated by observing the microcathodoluminescence pattern after layer-by-layer dry etching in steps of up to $\sim 1.5\ \mu\mathrm{m}$.
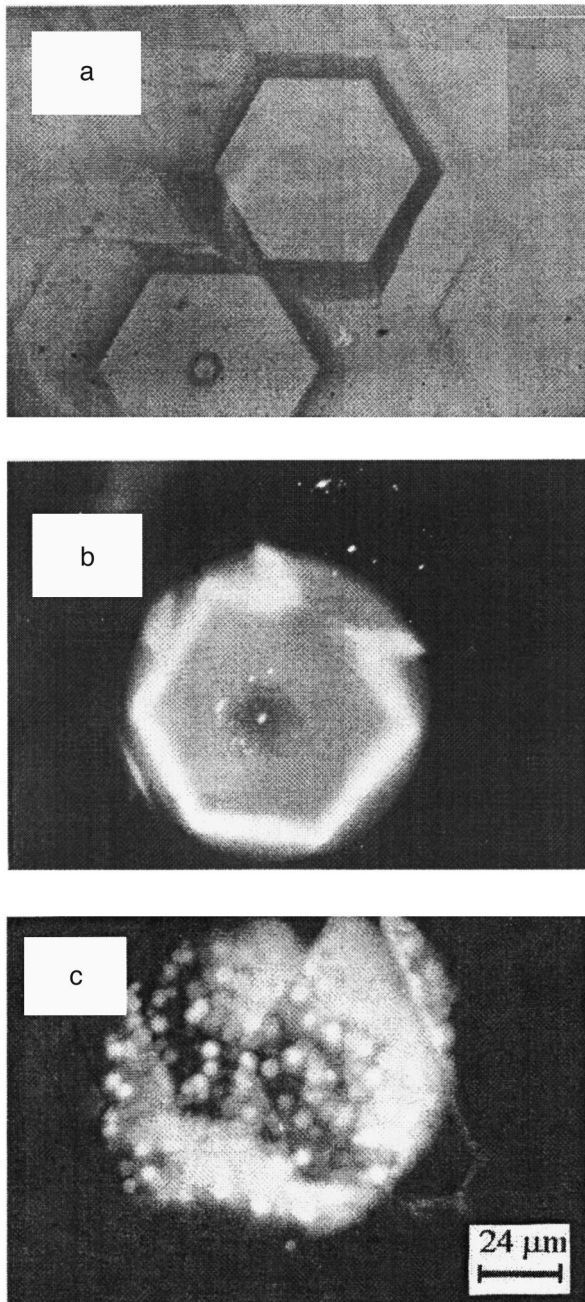
FIG. 1. a—Typical surface morphology of epitaxial GaN films with hexagonal pyramids; b—Microcathodoluminescence image of hexagonal pyramid after etching at a depth of ~3.5 μm. The white field around the pyramid is the luminescence of the sapphire substrate (dark red) and the buffer layer (yellow). At the center of the pyramid there is a region of yellow glow (2.2 eV defect band) surrounded by a dark blue region (2.8 eV band), and at the edge 3.4 eV exciton luminescence. The microcathodoluminescence spectra are shown in Fig. 2; c—Microcathodoluminescence image of half-planes in region of smoothed surface between pyramids revealed by etching to a depth of approximately 2 μm.

The largest changes in the microcathodoluminescence image were observed in the regions of smoothed surfaces between the pyramids. It can be seen from Fig. 1c that this region consists of a set of {0001} half-planes inclined at a small angle and not completely overlapping. At the center of each half-plane there is a yellow spot. The half-planes also include many other spots. As the layer thickness decreases in the etching process, the number of spots and their size increase, indicating that the yellow spots are localized in the low-temperature buffer layer. Note that the microstructure characteristics of GaN layers have already been studied in Refs. 6–8. Qian *et al.*[6] observed misoriented structural blocks and in Ref. 7 noted that misorientation of the *c* axis may cause the formation of screw dislocations in the direction of growth. At the center of the upper part of the pyramids, Ponce *et al.*[8] observed screw dislocations in the form of hillocks with penetrating holes between a few and tens of nanometers in diameter. We also observed similar hillocks on the growth pyramids in our layers when these were examined using a high-resolution scanning microscope.

As a result of this comparative analysis of the published data and the observed microcathodoluminescence pattern, we propose the following model for the formation of the epitaxial layer. Deposition of the buffer layer is accompanied by the formation of nucleation centers. Subsequent annealing of the buffer layer at high temperature causes crystallization, growth, and coalescence of these nuclei.[9] The film then grows as a result of the planes of islands of screw dislocations reaching the surface (with the formation of minipyramids) or as a result of the migration of steps by two-dimensional nucleation (edge zone of the pyramids). The minipyramids begin to grow from a defect (either the substrate or a nucleus). Since each pyramid is most likely characterized by a single type of structural defect (we postulate that its formation is attributed to the growth of screw dislocations), these minipyramids are a good object for studying the interaction between a particular type of defect and impurities during the doping of GaN. A study of the characteristics of this interaction should provide an understanding of the mechanisms for the doping of GaN films, especially with Si and Mg.

Figure 2a shows the microcathodoluminescence spectra obtained at 300 K for various parts of the pyramids after etching. In the central part of the pyramid, in addition to an edge ultraviolet band with a maximum at $E \sim 3.47$ eV and a yellow defect band with $E \sim 2.2$ eV, we observed a weak near-ultraviolet band with $E \sim 2.8$ eV which determines the color of this region. The intensity of the edge- and near-ultraviolet bands is a linear function of the excitation rate, whereas the yellow band in the central region saturates and is more clearly defined at low rates of excitation. In the microcathodoluminescence spectra from the central part of various pyramids at 77 K (Fig. 2b) the 2.8 eV band is transformed into a luminescence line at ~3.2 eV. As the rate of excitation decreases, this line separates into various bands. The $E \sim 3.26$ eV line corresponds to donor–acceptor recombination while the additional long-wavelength lines are probably its phonon replicas.[9,10] In the spectra at the edge of the pyramids this line is barely visible, although the edge ultraviolet band from this region has a high intensity with a smaller half-width (~58 meV at 77 K) which indicates that the material near the edge of the pyramids is of higher quality.

Thus, we can assume that acceptor levels occur near the $E \sim 2.8$ eV near-ultraviolet band. Bearing in mind that these layers were *n*-type and were not specially doped, we can attribute the appearance of acceptor levels to intrinsic de-
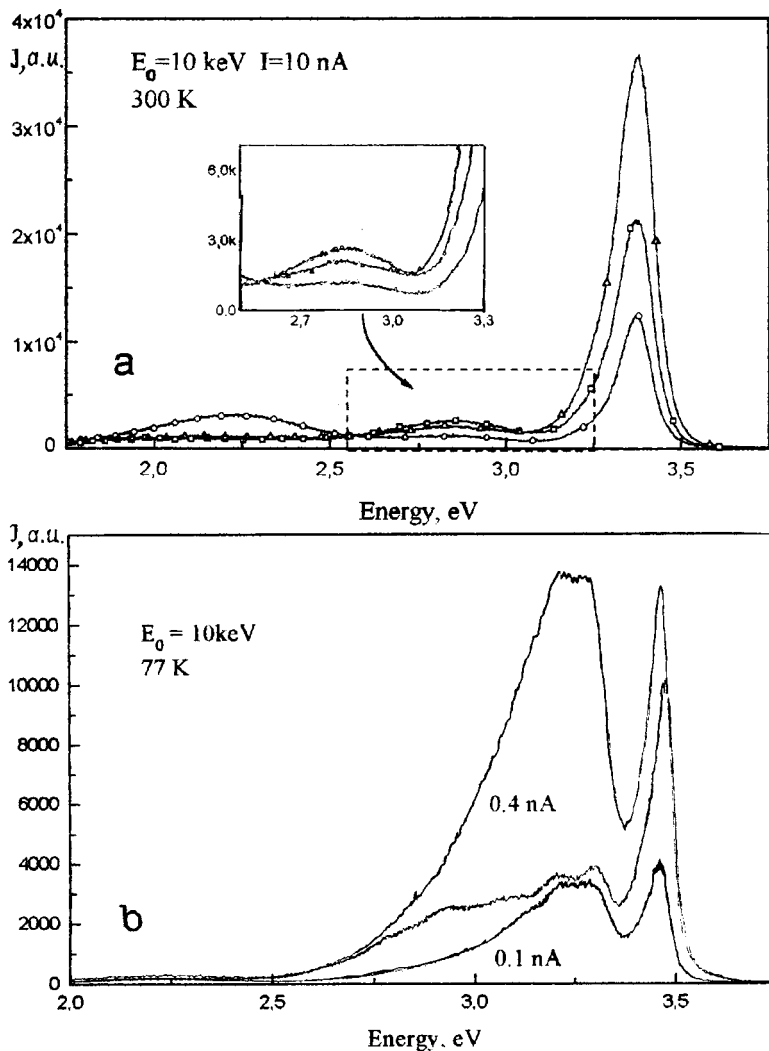
FIG. 2. a—Microcathodoluminescence spectra from different parts of pyramid after etching to a depth of $\sim 2\,\mu$m. b—spectra obtained at liquid-nitrogen temperature from the central regions of various pyramids at different rates of excitation.

fects. The regions where the $E \sim 2.8$ eV band was observed are close to the points where islands of screw dislocations occur and are probably formed by a spiral growth mechanism. These regions may contain unsaturated (broken) bonds which lead to the formation of acceptor levels and their appearance as a result of donor–acceptor recombination. Larger quantities of these unsaturated bonds should also be present at the center of the pyramid (in the nucleus of the screw dislocation). However, an intense yellow defect band (with $E \sim 2.2$ eV) is observed in these regions which indicates that the structure of the deep levels differs from that in the $E \sim 2.8$ eV regions. The mechanisms responsible for their formation have not yet been sufficiently well studied. Bearing in mind that the yellow defect band is localized near the interface, we attributed its appearance to an elevated concentration of carbon near the buffer layer as a result of incomplete breakdown of the initial components and the formation of complexes. The presence of pores in the nucleus of a screw dislocation may promote the diffusion of carbon at the center of the pyramid.

These characteristic bands in the microcathodoluminescence spectra were also observed in the photoluminescence spectra of specular layers of GaN and AlGaN which did not

exhibit hexagonal growth pyramids. We observed that as for the films with pyramids, the intensity of the yellow defect and near-ultraviolet bands depends on the growth conditions of the buffer layer. However, the spectra of a multilayer undoped double heterostructure consisting of a 0.5 μm thick GaN layer, a 2 μm thick AlGaN layer, a 0.3 μm thick GaN active layer, and a 0.08 μm thick AlGaN upper layer revealed edge emission only from the GaN active layer and the AlGaN upper layer,[11] with no $E \sim 2.8$ eV band. This confirms that the $E \sim 2.8$ eV band is attributable to structural growth defects which grow through the first GaN layer but may be stopped at the heterointerface or in the thick AlGaN layer.

CONCLUSIONS

A microcathodoluminescence study has been made of undoped GaN layers grown on sapphire by MOCVD as a function of the nitriding conditions of the substrate surface. The spatial distribution of the microcathodoluminescence was studied in typical growth regions of the layers and at various depths over the layer thickness using a method of dry

etching with an Ar ion beam. At a nitriding temperature of $\sim 1000\,°C$ the films exhibit growth characteristics in the form of hexagonal pyramids separated by a smoothed surface. The pyramids reveal a fine structure in which a region of donor–acceptor recombination can be identified. We attribute the presence of acceptor levels in this region to unsaturated (broken) bonds in structural defects caused by this region being formed by a spiral growth mechanism. The presence of a donor–acceptor band in mirror-smooth undoped epitaxial GaN films may indicate that this type of structural defect is present in these films.

[1] F. A. Ponce and D. P. Bour, Nature (London) **386**, 351 (1997).
[2] S. Nakamura, in *Proceedings of the International Symposium on Blue Laser and Light Emitting Diodes*, Chiba University, Japan, 1996.
[3] S. Keller, D. Kapolnek, B. P. Keller, Y. Wu, B. Heying, J. S. Speck, U. K. Mishra, and S. P. Denbaars, J. Phys. Soc. Jpn. **35**, L285 (1996).
[4] W. V. Lundin, B. V. Pushnyi, A. S. Usikov, M. E. Gaevski, M. E. Baidakova, and A. V. Sakharov, Inst. Phys. Conf. Ser. No. **155**, 319 (1997).
[5] I. Akasaki, H. Amano, Y. Koide, K. Hiramatsu, and N. Sawaki, J. Cryst. Growth **98**, 209 (1998).
[6] W. Qian, M. Scowronski, M. De Graef, K. Doverspike, L. B. Rowland, and D. K. Gaskill, Appl. Phys. Lett. **66**, 1252 (1995).
[7] W. Qian, S. Roher, M. Scowronski, K. Doverspike, L. B. Rowland, and D. K. Gaskill, Appl. Phys. Lett. **67**, 2284 (1995).
[8] F. A. Ponce, D. P. Bour, W. Götz, and P. J. Wright, Appl. Phys. Lett. **68**, 57 (1996).
[9] M. Ilegems and R. Dingle, Appl. Phys. **44**, 4234 (1973).
[10] A. Salvador, W. Kim, O. Aktas, A. Botchkarev, Z. Fan, and H. Markoc, Appl. Phys. Lett. **69**, 2692 (1996).
[11] A. S. Usikov, W. V. Lundin, U. I. Ushakov, M. B. Stepanov, B. V. Pushnyi, N. N. Faleev, N. M. Shmidt, and V. V. Tretyakov, in *Abstracts of the 48th Annual Meeting of the Electrochemical Society*, 1997, p. 2113.

Translated by R. M. Durham

Optical limiting of laser radiation in dispersed liquid-crystal structures with fullerenes

N. V. Kamanina and L. N. Kaporskiĭ

All-Russia Scientific Center ''S. I. Vavilov State Optics Institute,'' Russian Science Center, St. Petersburg
(Submitted October 16, 1998)
Pis'ma Zh. Tekh. Fiz. **25**, 18–24 (April 12, 1999)

Reverse saturable absorption (optical limiting) in liquid crystal composites based on polyimides and polyvinyl alcohol with added fullerenes was investigated at the laboratory level. It was established that laser radiation was attenuated tenfold in these structures. The experimental data were compared with the transmission of similar systems without fullerene additives. © *1999 American Institute of Physics.* [S1063-7850(99)00304-3]

INTRODUCTION

The prospects for research and subsequent applications of thin films of liquid crystal droplets dispersed in a polymer base[1)] are presently indisputable. This is primarily because these systems retain many of the properties of the polymer matrix, especially the film-forming capacity and high mechanical strength, and second combine the unique electrooptic properties of a liquid-crystal mesophase. These systems can operate without polarizing devices, which substantially enhances the brightness of displays,[1] they have faster switching times,[2] no particular constraints are imposed on the orienting surfaces,[1,3] and problems of threshold and hysteresis are easily resolved.[4]

The mechanism for the action of PDLC-based cells is as follows.[4] A liquid crystal is selected, in this case a nematic, whose ordinary refractive index n_0 is close to the refractive index of the polymer matrix n_p. In the initial state a refractive index gradient exists as a result of the arbitrary orientation of the liquid crystal director at the liquid-crystal droplet–polymer interface, and this is responsible for strong scattering of light by the composite. When an electrical or optical stimulus is applied, for the light propagating normally to the surface of the cell $n_0 \simeq n_p$, the refractive index gradients are very small, the liquid crystal director is oriented in the direction of the field or in the direction of the electric vector of the light wave, no scattering takes place, and the system becomes transparent. The fact that the liquid crystal is partially heated on exposure to an intense optical or electrical stimulus[5] also helps to equalize the refractive indices. When the electrical or optical stimulus is removed, the composite returns to the initial dispersive state.

Recently, the addition of fullerene clusters has been used to effectively control the transmission of liquid-crystal[6] and polymer[7–9] systems. This not only regulates the laser irradiation thresholds but also substantially attenuates the laser radiation. In addition, systems with added fullerenes are used to record holograms,[8] for frequency doubling and trebling,[10] and also as laser switches.[11]

The aim of the present paper is to investigate the optical limiting effect in light-controlled dispersed liquid-crystal structures with added fullerenes.

EXPERIMENT

The initial dispersed mixture was prepared by carefully mixing a polymer and a nematic in the ratio 3:2 to obtain a homogeneous emulsion. Finely dispersed fullerene powder (mixed C_{60} and C_{70}) was either added to the initial liquid crystal or was added to the tetrachloroethane during preparation of the polyimide solution. The emulsion was poured onto a substrate with calibrated spacers and was dried to remove the solvent. The thickness of the samples was $\sim 10\,\mu m$ and the size of the nematic droplets in the polymer matrix was 2–$3\,\mu m$. The nematic was formed of ZhK999, ZhK1289, and E7 (BDH) and the polymer base comprised 3% and 6.5% tetrachloroethane solutions of polyimide 6B and a 10% aqueous solution of polyvinyl alcohol.

The second harmonic of a pulsed neodymium laser ($\lambda = 532$ nm) was used to investigate the optical limiting of laser radiation. The diameter of the radiation spot on the sample was ~ 3 mm. The radiation intensity was varied by using calibrated light filters. In our experiment the dimensionless parameter k^*R, where $k^* = 2\pi n_p/\lambda$ and R is the droplet radius, was in the range 96–104, i.e., $k^*R \gg 1$, and according to the classification put forward by Zharkova and Sonin,[4] anomalous diffraction occurs for ''optically soft'' droplets.

RESULTS AND DISCUSSION

The main experimental results are plotted in Figs. 1a and 1b.

It was established that under the action of millijoule laser radiation, the radiation is attenuated by at least a factor of 10–15 for all the fullerene-containing samples.

In general, the principle of optical limiting for media containing fullerenes is based on the fact that the absorption of a $\lambda = 532$ nm photon by a C_{60} or C_{70} molecule is accompanied by the formation of a triplet-state molecule with an absorption cross section greater than that for the unexcited molecule.[12,13] The absorption increases as the laser radiation intensity increases because of the enhanced population of excited states. In our experiment the pulse duration is $\tau_p \sim 15$ ns, and the singlet–triplet interaction time is ~ 1.2 ns (Ref. 11). We then have $\tau_p > \tau_{S_1 \rightarrow T_1}$ and the triplet state acts as a store for excited states. In this case reverse saturable
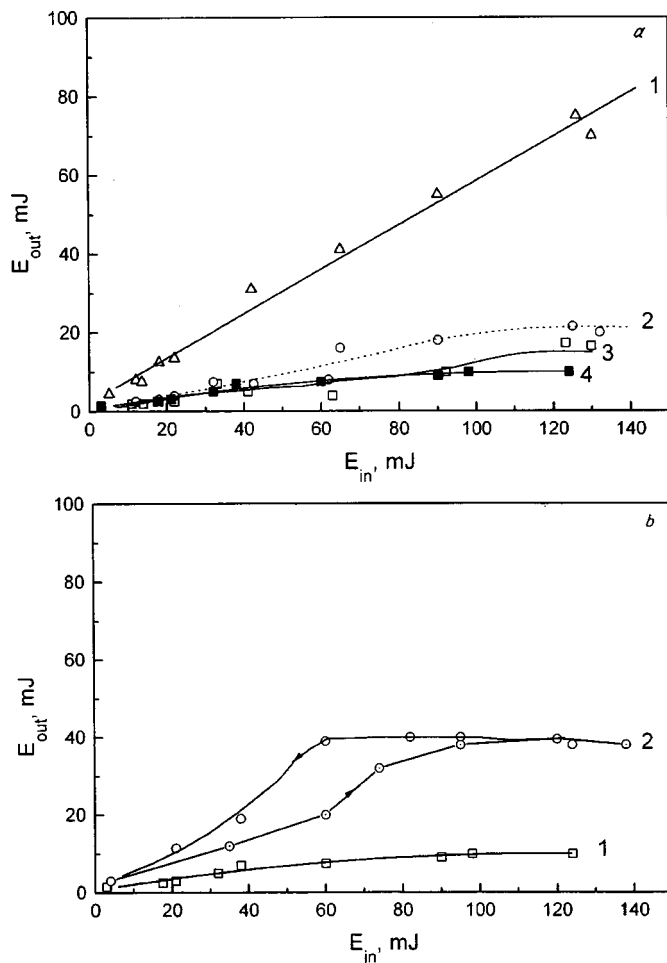
FIG. 1. Output radiation energy from samples (E_{out}) versus input radiation energy (E_{in}). a: *1*—structure consisting of 3% polyimide 6B and ZhK999 without fullerene; *2*—fullerene-containing structure comprising 6.5% polyimide 6B and ZhK999; *3*—fullerene-containing structure comprising 3% polyimide 6B and ZhK999; *4*—fullerene-containing structure comprising polyvinyl alcohol and liquid crystal E7; b: *1*—fullerene-containing structure comprising polyvinyl alcohol and liquid crystal E7; *2*—structure comprising polyvinyl alcohol and liquid crystal E7 without fullerene (the arrows indicate the forward and reverse profile of the curve).

absorption and consequently the principle of the optical limiting of laser radiation is accomplished via the $T_1 \rightarrow T_n$ channel. The population, saturation, and decay of the levels involved in the optical limiting process is accurately described by a six-level scheme and was analyzed in detail in Refs. 10–12. In our experiments we recorded an increase in absorption with increasing illumination intensity, followed by saturation, and limiting for all fullerene-containing samples.

We draw attention to the characteristics of the dispersed systems manifest in the optical limiting effect. It can be seen from Fig. 1a that the behavior of curves *2* and *3* differs slightly. For the same ratio of nematic to polymer and the same amount of added fullerene, saturation is observed at higher illumination intensities for the PDLC with a 6.5% polyimide solution than that for the 3% polyimide base. In the first case, saturation occurs at $\sim 0.7-0.8 \, \text{J/cm}^2$ whereas in the second case it occurs at around $0.4 \, \text{J/cm}^2$. It would seem that the optically denser medium should have a lower saturation level and not the reverse, as was recorded experi-

mentally. This difference may be attributed to the orientation of the liquid crystal dipoles along the polymer–liquid-crystal walls; as the illumination intensity increases, this influence of the walls lasts longer for the 6.5% polyimide than for the 3% polyimide. It is also possible that for different polymer concentrations there is a particular effective ratio n_0/n_p which is responsible for the existence of a different scattering component even for light incident normally on the sample.

Curve *4* shows the onset of optical limiting for a fullerene-containing PDLC based on polyvinyl alcohol. It is worth noting that the behavior of the curves $E_{out} = f(E_{in})$ is almost the same for the ZhK1289 and E7 systems. The output power is limited by a factor of $\sim 12-15$ for ZhK1289 and E7, respectively, because n_0 and n_p are more accurately matched for E7 ($n_0 = 1.525$; Ref. 14) and polyvinyl alcohol ($n_p = 1.54$) compared with ZhK1289 ($n_0 = 1.50$; Ref. 2).

In addition to studying the optical limiting in fullerene-containing dispersed systems, we also investigated similar structures without fullerenes in order to distinguish the normal bleaching of liquid crystal composites under the action of intense laser radiation from the reverse saturable absorption effect. The results of comparative experiments are plotted in Fig. 1b. It can be seen that in the absence of fullerenes for sample E7 with polyvinyl alcohol the level of transmission is 30–40% (curve *2*), which reduces the transmitted radiation by a factor of 1.7–2.5 for different levels of illumination and not by an order of magnitude, as in Fig. 1b, curve *1*. In addition, we recorded hysteresis on the transmission curve *2*, which is not at variance with the long-term memory of nematics in liquid-crystal composites[4] observed after the optical action has been reduced.

Note that in the optical limiting effect we observed no hysteresis loops for any of the samples. However, bearing in mind the influence of the liquid-crystal polymer walls on the reorientation of the nematic in droplets, we cannot categorically exclude the appearance of hysteresis in fullerene-containing PDLCs. Hysteresis may be observed in a narrower range of illumination intensities compared with that proposed in our experiment.

CONCLUSIONS

These investigations have shown the potential usefulness of fullerene-containing dispersed liquid-crystal systems as laser switches which limit the laser radiation power in the range $\leqslant 0.4 \, \text{J/cm}^2$. Note that this range may be extended in either direction by additional electrical control of these systems which, even allowing for attenuating inhomogeneities at the nematic droplet–polymer interface, leads to threshold reorientation of the liquid crystal director in the electric field as a result of a Fréedericksz transition.

[1)]Subsequently called liquid-crystal composite or polymer dispersed liquid crystal PDLC.

[1]E. Shimada and T. Uchida, J. Phys. Soc. Jpn. **31**, L352 (1992).

[2]N. A. Vasilenko, M. A. Groznov, V. M. Mokshin, V. S. Myl'nikov, S. S. Topol', V. V. Trukhtanov, V. V. Shvets, and L. N. Soms, Zh. Tekh. Fiz **61**(4), 80 (1991) [Sov. Phys. Tech. Phys. **36**, 418 (1991)].

[3]R. Yamaguchi and S. Sato, J. Phys. Soc. Jpn. **31**, L254 (1992).

[4]G. M. Zharkova and A. S. Sonin, *Liquid-Crystal Composites* [in Russian], Nauka, Novosibirsk (1994), 214 pp.

[5]F. Simoni, G. Cipparrone, C. Umeton, G. Arabia, and G. Chidichimo, Appl. Phys. Lett. **54**, 896 (1989).

[6]V. V. Danilov, A. G. Kalintsev, N. V. Kamanina, and S. A. Tul'skiĭ, Pis'ma Zh. Tekh. Fiz. **24**(9), 66 (1998) [Tech. Phys. Lett. **24**, 359 (1998)].

[7]A. Kost, L. Tutt, M. B. Klein, T. K. Dougherty, and W. E. Elias, Opt. Lett. **18**, 334 (1993).

[8]V. P. Belousov, I. M. Belousova, V. G. Bespalov, V. P. Budtov, V. M. Volynkin, V. A. Grigor'ev, O. B. Danilov, A. P. Zhevlakov, A. G. Kalintsev, A. N. Ponomarev, S. A. Tul'skiĭ, and E. Yu. Yutanova, Opt. Zh. **64**(9), 82 (1997) [J. Opt. Technol. **64**, 870 (1997)].

[9]N. V. Kamanina, L. N. Kaporskii, and B. V. Kotov, Opt. Commun. **152**, 280 (1998).

[10]H. Hoshi, N. Nakamura, Y. Maruyama, T. Nakagawa, S. Suzuki, H. Shiromaru, and Y. Achiba, J. Phys. Soc. Jpn. **30**, L1397 (1991).

[11]V. P. Belousov, I. M. Belousova, V. P. Budtov, V. V. Danilov, O. B. Danilov, A. G. Kalintsev, and A. A. Mak, Opt. Zh. **64**(12), 3 (1997) [J. Phys. (Moscow) **64**, 1081 (1997)].

[12]S. Couris, E. Koudoumas, A. A. Ruth, and S. Leach, J. Phys. B: At. Mol. Opt. Phys. **28**, 4537 (1995).

[13]A. V. Eletskiĭ and B. M. Smirnov, Usp. Fiz. Nauk **163**(2), 33 (1993) [Phys. Usp. **36**, 202 (1993)].

[14]F. Simoni, G. Gipparrone, and C. Umeton, Appl. Phys. Lett. **57**, 1949 (1990).

Translated by R. M. Durham

Thermoelectrodynamic loss of material by a solid armature in a railgun as a cause of velocity limitation

É. M. Drobyshevskiĭ, É. N. Kolesnikova, and V. S. Yuferev

A. F. Ioffe Physicotechnical Institute, Russian Academy of Sciences, St. Petersburg
(Submitted October 29, 1998)
Pis'ma Zh. Tekh. Fiz. **25**, 25–32 (April 12, 1999)

It is shown that even when monolithic electrically conducting bodies (armatures) are accelerated in a railgun, redistribution of the current as a result of Joule diffusion allowing for the drop in the electrical conductivity with heating may lead to the appearance of negative mechanical stresses in the object. Assuming that the strength of the material is reduced or melting occurs, this causes a loss of material which can initiate shunting arcs behind the armature at a velocity of ~ 1 km/s. © *1999 American Institute of Physics.* [S1063-7850(99)00404-8]

1. It is usually assumed that the velocity skin effect is responsible for limiting the acceleration of a solid, electrically-conducting armature to 1–1.5 km/s. In the standard two-dimensional approximation, this effect concentrates the current toward the rear edge of the moving armature, causing overheating at this point and melting. The melt is entrained by the rails and the melt wave moves over the contact surface of the armature toward its front edge. As a result, the solid-state sliding contact is destroyed and replaced by an arc,[1] which causes catastrophic erosion of the solid surfaces and a drop in the acceleration efficiency. However, the experiments do not provide unambiguous confirmation of this scenario[2] and show that far more complicated processes develop.[3]

One such process may involve softening of some of the material, which then separates and is ejected from the main body of the armature as a result of the extremely nonuniform distribution of ampere forces in the armature and the resultant internal stresses, even in the one-dimensional case. As the armature is accelerated, the magnetic field and current will diffuse from its rear surface inward, causing a release of Joule heat, accompanied by heating and melting of the material. If the electrical conductivity of the material drops fairly sharply during heating, the maximum of the current density shifts from the surface toward the inside of the armature.

It is then easy to envisage a situation where the volume ampere force acting per unit mass and accelerating the heated layer is weaker than the ampere force per unit mass of the column of still unheated material pushed by it. As a result, tensile stresses may be created inside the armature. If, as a result of this thermoelectrodynamic effect (we use the term "dynamic" in its mechanical meaning), these stresses exceed the strength of the heated solid material or become zero in some volume of the melt, the rear layer of the armature may become detached from the main body, continuing (in the ideal case of electrical contact with the rails) to move with a lower acceleration than the rest of the armature. This lost material can induce low-voltage shunting arcs in the railgun channel.

2. In order to illustrate the possible occurrence of this effect, we shall analyze the acceleration of an armature under the action of an electric current in the two-dimensional approximation usually used to study the velocity skin effect.[1] In this case, the entire magnetic field is concentrated in the region bounded by the rails and the armature, which is a fairly rough approximation but can substantially simplify the problem. We shall confine our analysis to the case where the thickness of the skin layer formed around the rear wall of the armature is less than its characteristic dimensions. Then, neglecting the thermal conductivity, we obtain the following one-dimensional equations to calculate the distribution of the magnetic induction B and enthalpy H everywhere in the armature, apart from the corner regions:

$$\frac{\partial B}{\partial t} = \frac{\partial}{\partial x}\left(D \frac{\partial B}{\partial x}\right), \tag{1}$$

$$\frac{\partial H}{\partial t} = \rho\left(\frac{1}{\mu_0} \frac{\partial B}{\partial x}\right)^2, \tag{2}$$

where ρ is the resistivity, $D = \rho/\sigma\mu_0$ is the magnetic field diffusion coefficient, and the enthalpy H is given by

$$H = \begin{cases} c_S \gamma_S T, & T < T_m, \\ c_S \gamma_S T_m + \varepsilon Q, & T = T_m, \\ c_S \gamma_S T_m + \varepsilon Q + c_L \gamma_L (T - T_m), & T > T_m, \end{cases} \tag{3}$$

where T is the temperature, c is the specific heat, γ is the density, T_m and Q are the melting point and the heat of fusion, the subscripts "S" and "L" refer to the solid and liquid phase, respectively, and ε is the fraction of molten material defined as $\varepsilon = (H - c_S \gamma_S T_m)/Q$. Quite clearly we find $\varepsilon = 0$ for $T < T_m$ and $\varepsilon = 1$ for $T > T_m$. We subsequently assume that $\gamma_S = \gamma_L = \gamma = $ const.

The boundary and initial conditions for Eqs. (1)–(2) are given by

$$B = \mu_0 I/d \quad \text{for} \quad x = 0, \quad B = 0 \quad \text{for} \quad x = l,$$

$$B = 0 \quad \text{and} \quad H = c_S \gamma_S T_0 \quad \text{for} \quad t = 0, \tag{4}$$

where I is the current flowing through the armature, d is the width of the armature (rails), l is its length, and T_0 is the initial temperature.
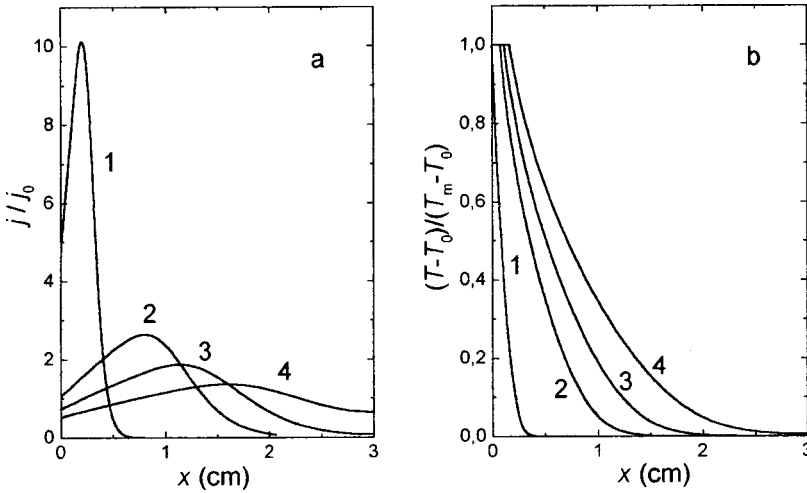
FIG. 1. Distribution of current density (a) and temperature (b) in the skin layer near the back of an aluminum armature with $d=3$ cm for $J=I_0/d=35$ MA/m. Curves *1* correspond to $t=t_L=74\,\mu$s when the armature begins to melt, *2*—$t=1$ ms, *3*—$t=2$ and *4*—$t=t_d=3.82$ ms, when the melt begins to become detached.

The temperature dependence of D in the solid phase was approximated by $D_S=D_0(1+\alpha(T-T_0))$, whereas in the liquid phase D was assumed to be constant and equal to D_L. In the two-phase region where $T=T_m$ the diffusion coefficient was defined as $D=(1-\varepsilon)D_S+D_L$.

The stresses near the rear wall of the armature were also calculated using the one-dimensional model

$$\sigma_x=\int_0^x((j\times B)_x-\gamma a)dx=\frac{B^2(0)-B^2(x)}{2\mu_0}-\gamma ax, \quad (5)$$

where j is the current density ($j_0=I_0/ld$) and a is the acceleration of the armature, which was determined assuming that the magnetic pressure acting on the rear wall of the armature is equal to the total inertial force $B^2(0)/2\mu_0=\gamma al$. On account of the two-dimensional nature of the problem, this last expression gives a greater acceleration for the same linear current density $J=I_0/d$ than in the three-dimensional case. Equation (5) fairly accurately describes the pressure distribution in the liquid phase, whereas in the solid phase it can be used for approximate estimates.

3. For the calculations we assumed that the total current I increases linearly from 0 to $I_0=$const over the time τ_0. The calculations were made for the simplest armature shape, i.e., cubic ($d=l$), and initially for the most commonly used light aluminum armature. The following parameters were used:[4] $\gamma=2700$ kg/m^3, $T_0=293$ K, $T_m=933$ K, $c_S=1000$ J/kg·K, $c_L=1177$ J/kg·K, $Q=400$ kJ/kg, $D_0=0.0216$ m^2/s, $D_L=0.16$ m^2/s, and $\alpha(T_m-T_0)=3.5$. We took $\tau_0=10\,\mu$s and assumed that $J=I_0/d$ varied in the range 35–60 MA/m. The calculations confirm that the armature may be damaged under the influence of the thermoelectrodynamic effect. A slightly unexpected result was that in all the one-dimensional cases investigated by us (for $d=1$, 3, and 9 cm) melting of the material in the rear layers preceded the appearance of negative stresses in these layers. Quite clearly, the negative stresses initially occur directly at the rear surface of the armature (where $d\sigma_x/dx|_{x=0}=0$), and if this contains liquid phase material damage and separation will take place continuously.

Figure 1 shows typical plots of the current penetration and temperature distribution in the rear layer of an Al arma-

ture. Note that for the case shown in Fig. 1, the rear surface of the armature did not melt completely before becoming detached at time $t=t_d$. In this case, when we have $T=T_m=$const a zone forms consisting of a mixture of solid and liquid phases. At current densities $J\geqslant40$ MA/m melting begins at $t<50\,\mu$s and by the detachment time $t=t_d$ the back of the armature has melted completely (for current densities $J=40$ MA/m the detachment time is $t_d=3.24$ ms; at $J=45$ MA/m $t_d=2.72$ ms; at $J=50$ MA/m $t_d=2.16$ ms; and at $J=60$ MA/m $t_d=1.5$ ms). Calculations made for various Al alloys, which generally have lower electrical conductivity and lower T_m, give similar results. A variation of τ_0 within one order of magnitude does not alter the general pattern.

Aluminum has a relatively low melting point and its electrical conductivity depends fairly weakly on temperature so that current flowing through the same site for a fairly long time melts the material. Thus, in our search for a light metal having properties suitable for developing an armature which undergoes damage later in the acceleration, we made calculations for Ti ($\gamma=4500$ Kg/m^3, $T_m=1880$ K, $c_S=550$ J/kg·K, $c_L=600$ J/kg·K, $Q=315$ kJ/kg, $D_0=0.34$ m^2/s, $\alpha(T_m-T_0)=6$ (Refs. 4 and 5) and Be $\{\gamma=1840$ kg/m^3, $T_m=1560$ K, $c_S=2500$ J/kg·K, $D_0=0.032$ m^2/s, $\alpha(T_m-T_0)=12.8$; $\sigma=30[1-(T-T_0)/(T_m-T_0)]$ MPa$\}$ (Refs. 4 and 6).

As in an aluminum armature, negative stresses only appear in a titanium armature after the liquid phase has formed, despite the high melting point. This is primarily because of the low electrical conductivity of titanium and the consequent rapid heating of the material at a high rate of current diffusion inside the armature. Allowance for phase transitions in Ti at $T\leqslant1150$ K, when the electrical resistance stops increasing, does not significantly alter the picture.

If we disregard its toxic properties, the most interesting armature material is beryllium, which is a light refractory metal with a relatively high electrical conductivity. As a result, negative stresses appear near the rear surface of a Be armature before it melts (Fig. 2). Assuming that the tensile strength σ decreases linearly with temperature close to T_m, we find that these stresses even cause solid rear sections to separate from the armature. In this case, the speed reached by
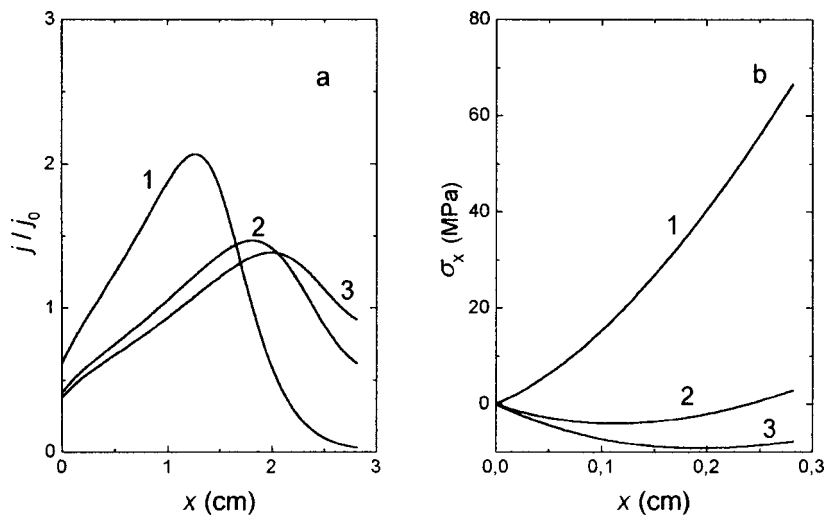
FIG. 2. Distribution of current density (a) and mechanical stresses (b) in the skin layer near the back of a beryllium armature with $d = 3$ cm for $J = 45$ MA/m. Curve *1* corresponds to $t = 1$ ms, *2*—$t = 2$, and *3*—$t_d = 2.33$ ms when the solid back layers begin to become detached from the armature.

the Be armature before damage is slightly higher than that for an Al armature.

4. These results are generally qualitative, indicating some new prospects for delaying the crisis where the acceleration process transitions to arcing and providing a possible explanation for the phenomena observed in real accelerators.

Quite clearly, since real configurations are three-dimensional, as a result of the faster diffusion of the field near the edges and corners, tensile (tangential) stresses may appear considerably earlier and thus may even appear in the solid material of the low-melting Al alloy armatures usually used. Bearing in mind the drop in strength with temperature, the thermoelectrodynamic effect can then cause various sections of the accelerated armature to be ejected before they melt.

At this point it is convenient to note that effects involving a reduction in strength and in some sense, liquefaction of the material, i.e., the loss of long-range order in the structure, the formation of new dislocations, and an increase in their propagation velocity, are promoted, regardless of the Joule heating, by the flow of large electrical currents ($j \sim 10^5 - 10^6$ A/cm^2, electroplasticity)[7] and also by intense ultrasonic ($f \sim 10^5 - 10^6$ Hz) vibrations (acoustoplasticity).[8] These vibrations inevitably occur under conditions where the armature experiences pinch vibrations and electrical explosions at contact constrictions,[3] and also as a result of the motion of an object in contact with the uneven eroded channel walls. Large-amplitude vibrations should also be generated by cumulative microejections of material from surface cavities, and so on. Vibrations are possibly responsible for the ''splintered wood'' appearance at sites where the armature undergoes enhanced Joule heating.[2] So far, no attention has been paid to the reduction in the strength of an armature under the action of current and vibrations.

It is also worth noting that the velocity skin effect may be treated as a particular case of the thermoelectrodynamic effect.

5. The appearance of a large quantity of small heated particles, droplets, and vapor ejected from the armature in the railgun channel must obviously stimulate parasitic electrical breakdowns which go over to arc discharges. Although

the physics of high-current arc discharges in metal vapor has not yet been developed in detail,[9] we know that the characteristic voltage for a short (~ 1 cm) arc is ~ 30–50 V. If the electrical conductivity of the plasma is reduced, the magnetic field actually doubles or trebles this value, i.e., to ~ 100 V. However, for the typical inductance of the rails per unit length $L' \approx 0.3$ μH/m these values are also characteristic of the induction back-emf $\Delta U_L = L'IV$, which must be additionally applied to the breech part of the rails for the current $I \approx 500$ kA to pass through the system at $V \approx 1$ km/s. Measurements made at the exit edge of the channel indicate that the purely Ohmic voltage drop for a solid armature is small, only ~ 10 V (Ref. 10). Thus, it is quite conceivable that after the inter-rail potential difference has reached $\Delta U_L \sim 100$ V, the formation of relatively stable arcs behind the armature, initiated by metal ejected from the armature, will limit the velocity of a solid electrically conducting armature to around $V \sim 1$ km/s.

[1] P. B. Parks, J. Appl. Phys. **67**, 3511 (1990).

[2] D. Kirkpatrick and D. Haugh, IEEE Trans. Magn. **33**, 109 (1997).

[3] É. M. Drobyshevskiĭ, B. G. Zhukov, R. O. Kurakin, S. I. Rozov, M. V. Beloborodyĭ, and V. G. Latypov, Pis'ma Zh. Tekh. Fiz. **25**(6), 89 (1999) [Tech. Phys. Lett. **25**, 245 (1999)].

[4] *Handbook of Physical Quantities*, edited by I. S. Grigor'ev and E. Z. Meĭlikhov [in Russian], Énergoatomizdat, Moscow (1991), 1232 pp.

[5] U. Zwicker, *Titan und Titanlegierungen* (Springer-Verlag, Berlin, 1974; Metallurgiya, Moscow, 1979, 511 pp.)

[6] G. F. Silina, Yu. I. Zarembo, and L. É. Bertina, *Beryllium: Chemical Technology and Metallurgy* [in Russian], Atomizdat, Moscow (1960), 120 pp.

[7] H. Conrad and A. F. Sprecher, in *Dislocations in Solids. Vol. 8, Basic Problems and Applications*, edited by F. R. N. Nabarro (North-Holland, Amsterdam, 1989), Chap. 43, pp. 497–541.

[8] A. B. Lebedev, Mater. Sci. Forum **210–213**, 519 (1996).

[9] Yu. P. Raĭzer, *Gas Discharge Physics* (Springer-Verlag, New York, 1991; Nauka, Moscow, 1987, 592 pp.)

[10] R. A. Marshall, IEEE Trans. Magn. **31**, 209 (1995).

Translated by R. M. Durham

Chemical potential of a binary solution

S. V. Bulyarskiĭ and V. V. Prikhod'ko

Ulyanovsk State University
(Submitted October 20, 1998)
Pis'ma Zh. Tekh. Fiz. **25**, 33–37 (April 12, 1999)

The chemical potential of a binary solution is calculated using the Gibbs free energy method. With the aid of certain assumptions on the microscopic structure of the solution, the well-known expression is derived for a simple solution. It is shown that the empirical interaction parameter is expressed in terms of the change in enthalpy and entropy accompanying the exchange of atoms between the pure components. © *1999 American Institute of Physics.*
[S1063-7850(99)00504-2]

The chemical thermodynamics of solutions has so far remained a semiempirical science based on using relationships characteristic only of ideal substances. Parameters whose physical meaning remains unclear are introduced to describe real substances. In particular, according to Guggenheim (see Ref. 1), simple binary solutions are solutions whose excess free energy is $G^E = \alpha(T)x(1-x)$, where $\alpha(T)$ is some interaction parameter. Calculations of this parameter made by Swalin[2] for regular solutions using a quasichemical reaction method are unsatisfactory because they do not explain the relationships observed in practice. We propose an algorithm to calculate the chemical potential of a binary solution based on a microscopic analysis of the Gibbs free energy. This approach has recently been successfully used to calculate the stoichiometry of solids.[3] It will be shown subsequently that this method can be used to obtain an expression for the chemical potential of a simple solution and to clarify the physical meaning of the interaction parameter.

In order to write the Gibbs free energy of a binary solution, we shall divide the volume occupied by the liquid into cells such that each cell contains only one atom. This model is justified by the fact that the liquid frequently conserves the short-range order characteristic of the crystalline state. Each atom in the solution is surrounded by a certain number of others, which include atoms of both the first and second components. We shall assume that each atom in the binary solution has the same number of nearest neighbors. This implies first that the coordination numbers of both components in the pure state are the same and second, that the sizes of atoms of both components are approximately the same.

Let us assume that an atom of component 1 has m nearest neighbors. This atom can then be surrounded by m like atoms, $m-1$ like and 1 unlike, $m-2$ like and 2 unlike atoms, and so on. Consequently, the free energy assigned to this atom may have values of g_0, g_1, g_2, and so on. Similarly, for atoms of component 2 surrounded by m neighbors, we have the possible energies h_0, h_1, and so on. The probability of an atom being surrounded by $m-n$ atoms of component 1 and n atoms of component 2 is proportional to $C_m^n N_1^{m-n} N_2^n$, where N_1 and N_2 are the numbers of atoms of components 1 and 2 in the system, and C_m^n is a binomial coefficient which allows for the number of possible configu-

rations of neighbors around the atoms. In order to obtain a total probability of unity, this must be divided by the normalizing factor $\sum_{n=0}^{m} C_m^n N_1^{m-n} N_2^n = (N_1 + N_2)^m$.

Hence the Gibbs free energy of a binary solution calculated per atom is written as

$$G = N_1 \sum_{i=0}^{m} p_i g_i + N_2 \sum_{i=0}^{m} p_i h_i - kT \ln \frac{(N_1 + N_2)!}{N_1! N_2!}, \quad (1)$$

where

$$p_i = \frac{C_m^i N_1^{m-i} N_2^i}{(N_1 + N_2)^m}.$$

We calculate the chemical potential of the first component:

$$\mu_1 = \frac{\partial G}{\partial N_1}.$$

We note that N_1 and N_2 appear in the energy derivative in the form of the expressions $N_1/(N_1+N_2)$ and $N_2/(N_1+N_2)$. Replacing these expressions by the mole fractions x_1 and x_2, we obtain

$$\mu_1 = \sum_{i=0}^{m} g_i(m+1-i)C_m^i x_1^{m-i} x_2^i - m \sum_{i=0}^{m} g_i C_m^i x_1^{m+1-i} x_2^i$$

$$+ \sum_{i=1}^{m} i h_i C_m^i x_1^{i-1} x_2^{m+1-i} - m$$

$$\times \sum_{i=0}^{m} h_i C_m^i x_1^i x_2^{m+1-i} + kT \ln x_1. \quad (2)$$

A similar expression may be obtained for the chemical potential of the second component by transposing the subscripts 1 and 2 and also g_i and h_i in Eq. (2).

Expression (2) contains $m+1$ values of g_i and the same number of h_i. Their values are unknown, so we shall make a simplifying assumption. We write $g_i = g_0 + i\Delta g$ and $h_i = h_0 + i\Delta h$, where Δg and Δh are the changes in the free energy per atom when a neighboring atom of one species is replaced by an atom of the other species. Substituting g_i and h_i into Eq. (2), we obtain a cumbersome expression containing eight

sums. These sums can be simplified appreciably having noted that they are expressed only in terms of $(x_1+x_2)^m$, or in terms of derivatives of $(x_1+x_2)^m$ with respect to x_1 or x_2. We write these eight sums assuming that $x_1+x_2=1$:

$$g_0 \sum_{i=0}^{m} (m+1-i)C_m^i x_1^{m-i} x_2^i$$

$$= g_0 \frac{\partial}{\partial x_1}(x_1(x_1+x_2)^m) = g_0 + mg_0 x_1, \qquad (2a)$$

$$\Delta g \sum_{i=1}^{m} i(m+1-i)C_m^i x_1^{m-i} x_2^i = \Delta g \frac{\partial}{\partial x_1}\left(x_1 x_2 \frac{\partial}{\partial x_2}\right.$$

$$\left. \times (x_1+x_2)^m\right) = m\Delta g x_2 + m(m-1)\Delta g x_1 x_2, \qquad (2b)$$

$$-mg_0 \sum_{i=0}^{m} C_m^i x_1^{m+1-i} x_2^i$$

$$= -mg_0 x_1(x_1+x_2)^m = -mg_0 x_1, \qquad (2c)$$

$$-m\Delta g \sum_{i=1}^{m} iC_m^i x_1^{m+1-i} x_2^i = -m\Delta g x_1 x_2 \frac{\partial}{\partial x_2}(x_1+x_2)^m$$

$$= -m^2\Delta g x_1 x_2, \qquad (2d)$$

$$h_0 \sum_{i=1}^{m} iC_m^i x_1^{i-1} x_2^{m+1-i} = h_0 x_2 \frac{\partial}{\partial x_1}(x_1+x_2)^m = mh_0 x_2, \quad (2e)$$

$$\Delta h \sum_{i=1}^{m} i^2 C_m^i x_1^{i-1} x_2^{m+1-i} = \Delta h x_2 \frac{\partial}{\partial x_1} x_1 \frac{\partial}{\partial x_1}(x_1+x_2)^m$$

$$= m\Delta h x_2 + m(m-1)\Delta h x_1 x_2, \quad (2f)$$

$$-mh_0 \sum_{i=0}^{m} C_m^i x_1^i x_2^{m+1-i}$$

$$= -mh_0 x_2(x_1+x_2)^m = -mh_0 x_2, \qquad (2g)$$

$$-m\Delta h \sum_{i=1}^{m} iC_m^i x_m^i x_1^i x_2^{m+1-i}$$

$$= -m\Delta h x_1 x_2 \frac{\partial}{\partial x_1}(x_1+x_2)^m = -m^2\Delta h x_1 x_2. \qquad (2h)$$

Substituting these values into expression (2) and abbreviating some terms. we finally obtain

$$\mu_1 = g_0 + m(\Delta g + \Delta h)(1-x_1)^2$$

$$+ kT \ln x_1 = g_0 + kT \ln \gamma_1 x_1, \qquad (3)$$

where

$$\gamma_1 = \exp\left(\frac{m(\Delta g + \Delta h)(1-x_1)^2}{kT}\right). \qquad (4)$$

Similar expressions can also be obtained for the second component.

Equations of the type (3) and (4) are well known in the theory of regular solutions, the only difference being that the expression for the activity coefficient (4) contains the experimentally determined interaction parameter $\alpha(T)$ instead of $m(\Delta g + \Delta h)$. In many cases (especially for III–V semiconductors) it is found[1] that $\alpha(T) = a + bT$, where a and b are constants. However, the factor $m(\Delta g + \Delta h)$ can also be expressed similarly, recalling that $\Delta g = \Delta H_1 + \Delta S_1 T$ and $\Delta h = \Delta H_2 + \Delta S_2 T$. Hence

$$a = m(\Delta H_1 + \Delta H_2), \quad b = -m(\Delta S_1 + \Delta S_2).$$

We shall now determine the physical meaning of the parameters a and b. The quantity $m\Delta H_1$ is the change in enthalpy per atom when m neighbors of species 1 are replaced by m atoms of species 2 or, which amounts to the same thing, when an atom of the pure component 1 replaces an atom of pure component 2. The quantity $m\Delta H_2$ has the same meaning for an atom of the second component. Consequently, $m(\Delta H_1 + \Delta H_2)$ is the change in enthalpy accompanying the exchange of atoms between the two pure components and $m(\Delta S_1 + \Delta S_2)$ is the change in entropy for this process.

The assumptions made above that both components have the same coordination numbers and the atoms are of similar size limit the validity of these results. This reasoning only fully applies to a few solutions, and specifically to solutions of group IV semiconductors and solutions of metals with coordination numbers of 8–11 (Ref. 4). Metalloid association is observed in solutions of II–IV and III–V elements so that an association compound must be assumed for each atom, which leads to a large difference in the sizes of the atoms of the two components and a difference between their coordination numbers. Nevertheless, for low coordination numbers the size of the atoms is not so critical because of the short-range order. The influence of the atomic size may be taken into account by suitably defining the free energies g_i and h_i in Eq. (2). In this case, the mole fraction of the component will appear in the coefficient of activity as an mth degree polynomial rather than as a square. The temperature dependence remains the same.

[1] H. C. Casey and M. B. Panise, *Heterostructure Lasers* (Academic Press, New York, 1978; Mir, Moscow 1981, 364 pp.)

[2] R. A. Swalin, *Thermodynamics of Solids* (Wiley, New York, 1962; Metallurgiya, Moscow, 1968, 314 pp.)

[3] S. V. Bulyarskiĭ and V. I. Fistul', *Thermodynamics and Kinetics of Interacting Defects in Semiconductors* [in Russian], Nauka, Moscow (1997), 352 pp.

[4] M. I. Shakhparonov, *Introduction to the Modern Theory of Solutions* [in Russian], Vysshaya Shkola, Moscow (1976), 296 pp.

Flow in a turbulent supersonic boundary layer with a heat source

O. B. Larin and V. A. Levin

Institute of Mechanics, Moscow State University, Moscow

A numerical analysis is made of a turbulent supersonic boundary layer with a heat source for a wide range of heat supplied to the gas. It is shown that the frictional resistance may be reduced appreciably and the efficiency of using a heat conductor to achieve such a reduction is estimated. © *1999 American Institute of Physics.* [S1063-7850(99)00604-7]

An analysis is made of plane supersonic flow around a cooled plate in the presence of an external heat supply in a rectangular region. The system of averaged equations for the turbulent motion of an ideal gas in the absence of external mass forces in the boundary-layer approximation has the form

$$\frac{\partial \rho u}{\partial x} + \frac{\partial \rho v_*}{\partial y} = 0, \tag{1}$$

$$\rho u \frac{\partial u}{\partial x} + \rho v_* \frac{\partial u}{\partial y} = \frac{\partial}{\partial y}\left(\mu_* \frac{\partial u}{\partial y}\right), \tag{2}$$

$$\rho u \frac{\partial I_0}{\partial x} + \rho v_* \frac{\partial I_0}{\partial y} = \frac{\partial}{\partial y}\left(\lambda_* \frac{\partial T}{\partial y} + \mu_* u \frac{\partial u}{\partial y}\right) + \rho Q, \tag{3}$$

$$\rho = \frac{pm}{RT}, \quad \rho v_* = \rho v + \langle \rho' v' \rangle, \quad I_0 = I + \frac{u^2}{2},$$

$$\mu_* = \mu + \mu_t, \quad \lambda_* = \left(\frac{\mu}{\text{Pr}} + \frac{\mu_t}{\text{Pr}_t}\right)c_p.$$

Here u and v are the projections of the velocity vector on the orthogonal coordinate axes x (parallel to the surface) and y (along the normal to the surface), respectively, ρ is the density, p is the pressure, T is the temperature, I is the enthalpy, Q is the specific quantity of heat supplied externally per unit time to a given point in the medium (a known function of the coordinates), m is the molecular weight of the gas, R is the universal gas constant, $\langle \rho', v' \rangle$ is the correlation of the density pulsations and the normal component of the velocity, μ and μ_t are the dynamic coefficients of molecular and turbulent viscosity, c_p is the specific heat of the gas at constant pressure, and Pr and Pr_t are the Prandtl number and its turbulent analog. We assume that the last three parameters are constant.

The coefficient of turbulent viscosity is determined using the widely used two-layer model.[1]

The boundary conditions at the surface of the object around which the flow takes place ($y=0$) have the form $u=0$, $v=0$, and $T=T_w$. The flow characteristics at the outer boundary of the layer denoted subsequently by the subscript e are assumed to be known.
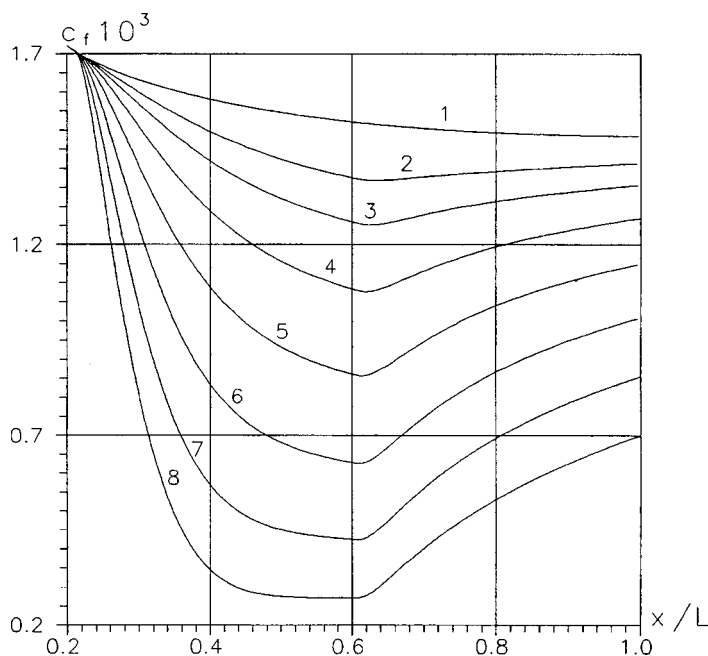
FIG. 1. Variation of the local coefficient of surface friction over the plate length. Specific heat supply q: 1—0, 2—1, 3—2, 4—4, 5—8, 6—16, 7—32, and 8—64.
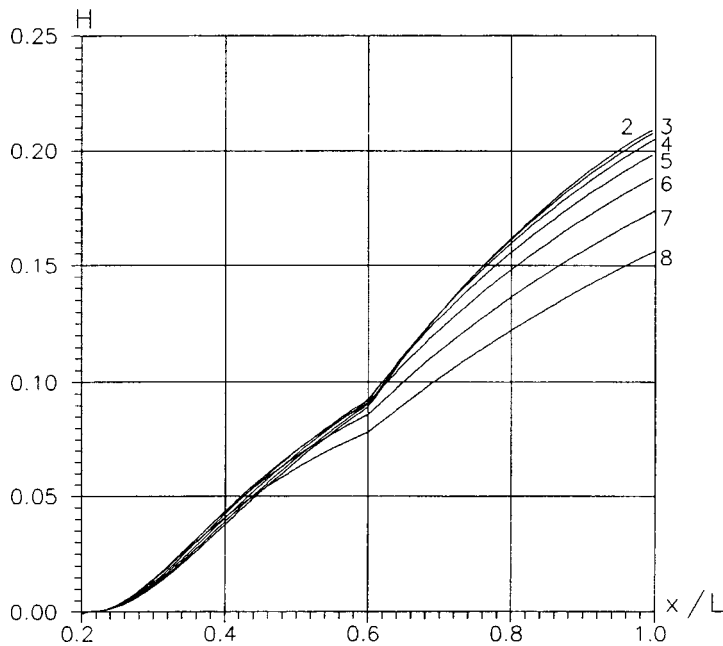
FIG. 2. Variation of the efficiency parameter over the plate length. Specific heat supply q: 2—1, 3—2, 4—4, 5—8, 6—16, 7—32, and 8—64.

The problem is solved numerically using a finite-difference method. The system (1)–(3) is first converted to dimensionless form using the normal coordinate $\eta = \delta^{-1}(x)\int_0^y \rho dy$, where $\delta(x)$ is some normalizing function. We use an implicit, arbitrarily stable, difference scheme, which gives a second-order approximation for the mesh steps Δx and $\Delta \eta$ and possesses good stabilizing properties.

Below we present some results of calculations made for an incoming flow with the Mach number $M_e = 3$. We assume that the temperature of the cooled wall is the same as the gas temperature at the outer boundary $T_w = T_e$. The Prandtl numbers and the ratio of specific heats are: $\mathrm{Pr} = 0.72$, $\mathrm{Pr}_t = 0.9$, and $\gamma = 1.4$. The coefficient of molecular viscosity μ is assumed to have a power dependence on temperature with the exponent $\omega = 0.76$.

We assume that an external heat supply with the constant parameter $q = Q(c_p T_e u_e)^{-1} L$ is provided in the rectangular region

$$0.2 < x/L \leqslant 0.6, \quad 5 \leqslant y/Y \leqslant 25. \tag{4}$$

Here we have $Y = \mu_e \rho_e^{-1} u_e^{-1} 10^4$ and $L = Y \cdot 10^4$. Note that the region (4) is completely within the boundary layer.

Figure 1 shows distributions of the local coefficient of surface friction $c_f = 2\tau_w \rho_e^{-1} u_e^{-2}$, where $\tau_w = (\mu \partial u/\partial y)_{y=0}$ is the friction stress. Curves 1–8 are plotted for the following values of the specific heat supply parameter $q = 0, 1, 2, 4, 8, 16, 32$, and 64 (positive values of the parameter in a geometric progression). It can be seen that the external heat supply causes a substantial reduction in the local friction. For instance, for $q = 64$ the local coefficient of surface friction at the end of the heat release zone is 5.6 times lower than that for $q = 0$.

Values of the parameter c_f corresponding to the case of no heat supply are restored relatively slowly downstream from the heat source. Heat sources with the parameters $q = 16$ and $q = 64$ reduce the frictional resistance $F(x_2)$ by 40% and 60%, respectively ($F(x) = \int_{x_1}^x \tau_w dx$, $x_1 = 0.2L$, $x_2 = 0.6L$), which is much greater than the reduction calculated by Kazakov *et al.*[2] for a supersonic boundary layer at a heat-insulated surface.

As the specific heat supply q increases, the flow of heat from the gas to the walls is appreciably intensified. For example, for $q = 16$ and $q = 64$ the maximum heat flows are 1.5 and 1.9 times those in the absence of any thermal action.

The efficiency of using a heat source to reduce the frictional resistance is estimated using the parameter

$$H = \frac{\Delta F u_e}{Q_*},$$

where $\Delta F = (F)_q - (F)_0$ and $Q_*(x)$ is the external heat supplied to the gas per unit time upstream from the cross section x.

The distributions $H(x)$ are plotted in Fig. 2 (the numbering of the curves is the same as in Fig. 1). For low values of q the heat supply efficiency depends weakly on the total quantity of heat supplied to the flow. When the specific heat supply q is increased appreciably, the heat supply efficiency drops slightly.

[1] T. Cebeci and A. M. O. Smith, *Analysis of Turbulent Boundary Layers* (Academic Press, New York, 1974), 404 pp.

[2] A. V. Kazakov, M. N. Kogan, and A. P. Kuryachiĭ, Izv. Ross. Akad. Nauk Ser. Mekh. Zhidk. Gaza No. 1, 48 (1997).

Translated by R. M. Durham

Hybrid "antenna–amplifier" relativistic traveling-wave tube using an azimuthally asymmetric mode of a rod slow-wave system

A. S. Shlapakovskiĭ

Research Institute of Nuclear Physics, Tomsk Polytechnic University
(Submitted August 19, 1998)
Pis'ma Zh. Tekh. Fiz. **25**, 43–50 (April 12, 1999)

A linear theory is developed for a Cherenkov microwave amplifier with a slow-wave system in the form of a circular waveguide with a dielectric rod. In this system the rod antenna can couple out the radiation into free space without additional channels and mode converters. An analysis is made of the general case with no azimuthal symmetry and conditions are determined where the dominant TEM$_{11}$ asymmetric mode predominates. © *1999 American Institute of Physics.* [S1063-7850(99)00704-1]

In the very first study of the generation of high-power microwave radiation by a relativistic high-power electron beam, Nation[1] used an electrodynamic system in the form of a waveguide with a ribbed rod, which provided the required slowing of the electromagnetic wave for Cherenkov interaction. In a coaxial geometry the maximum beam transport currents increase, which made this geometry a natural choice for the currents of several tens of kiloamperes used in these experiments. In addition to the possibility of using superpower beams, a coaxial configuration has the advantage of a reduced microwave field strength at the surface of the slow-wave structure.[2–4] Gunina *et al.*[2] also stressed the advantage that the oscillation spectrum of a corrugated rod is considerably more sparse than that of a waveguide section of similar dimensions. This allowed successful mode selection to be achieved in a Cherenkov generator in the millimeter range.

A coaxial system with a retarding rod also has another specific, very attractive feature first noted by Shlapakovskiĭ.[5] This relates to the novel possibilities for coupling microwaves in and out of the amplifier. A dielectric rod or a metal ribbed or corrugated rod is in fact a transmission line which forms the basis of the widely used surface wave antennas, which have been developed in detail.[6] If a cylindrical electron beam is launched along the surface of this antenna, the microwave signal supplying it will be amplified by the Cherenkov interaction mechanism. An external coaxial conductor, which may serve as a collector, is required to ensure that the beam propagates. Hence it is possible to have a hybrid comprising of a traveling-wave tube and a surface-wave antenna.

The usual working mode of a rod antenna is the dominant asymmetric TEM$_{11}$ mode, whereas the symmetric TM$_{01}$ mode is typical of a traveling-wave tube. In order to determine the potential scope of a hybrid "antenna–amplifier" system, we need to determine the gain and gain profiles for the TEM$_{11}$ mode as a function of the parameters of the beam and the slow-wave system in order to compare these first with the values typical of the conventional configuration of traveling-wave tubes and second, with the values obtained in the same coaxial system for the TM$_{01}$ mode and other higher-order modes. For this purpose it is sufficient to derive the "hot" dispersion equation for the system without assuming azimuthal symmetry for the perturbations. By solving this equation numerically we can obtain instability growth rates for any mode with an arbitrary azimuthal index.

In the present paper, such an investigation is made for a circular waveguide with a dielectric rod and a cylindrical electron beam between the rod and an external conducting wall. In fact this system is a variant of the dielectric Cherenkov maser (whose conventional slow-wave system is a waveguide with a dielectric insert).

We shall assume that the beam is infinitely thin, monoenergetic, and completely magnetized. For fields proportional to $\exp\{i(l\theta+kz-\omega t)\}$, where ω is the frequency, k is the longitudinal wave number, and l is the azimuthal index, the dependence of the longitudinal components E_z and H_z on the radial coordinate r allowing for the conditions at the metal surface are expressed by Bessel functions of the real (J_l) and imaginary (I_l and K_l) argument

$$E_z = A_E J_l(pr), \quad H_z = A_H J_l(pr), \quad r < a,$$

$$E_z = B_E I_l(qr) + C_E K_l(qr), \quad a < r < r_b,$$

$$E_z = D_E [K_l(qb) I_l(qr) - I_l(qb) K_l(qr)], \quad r_b < r < b,$$

$$H_z = B_H [K_l'(qb) I_l(qr) - I_l'(qb) K_l(qr)], \quad a < r < b. \tag{1}$$

Here a is the radius of the rod, r_b is the beam radius, and b is the waveguide radius, $p^2 = \varepsilon \omega^2/c^2 - k^2$, $q^2 = k^2 - \omega^2/c^2$, ε is the permittivity of the rod material, and $A_{E,H}$, $B_{E,H}$, C_E and D_E are arbitrary constants. The conditions for continuity of the azimuthal components of the field E_θ and H_θ at the surface of the dielectric have the following form:

$$\frac{1}{p^2}\left(k\frac{l}{r}E_z + i\frac{\omega}{c}\frac{dH_z}{dr}\right)_{r=a-0}$$

$$= -\frac{1}{q^2}\left(k\frac{l}{r}E_z + i\frac{\omega}{c}\frac{dH_z}{dr}\right)_{r=a+0},$$
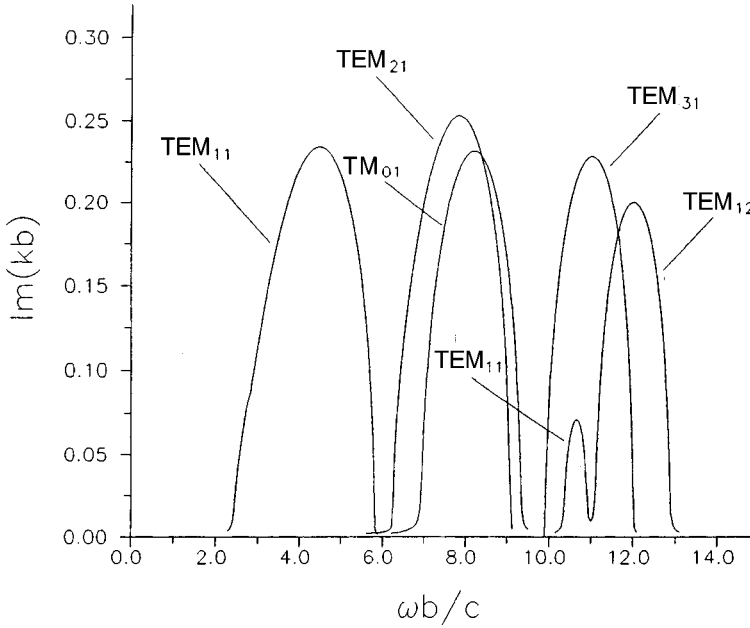
FIG. 1. Spatial growth rates versus frequency for various modes in a waveguide with a dielectric rod and cylindrical beam: $\varepsilon = 2.25$, $a/b = 0.5$, $r_b/b = 0.6$, $\gamma = 1.8$, and $I_b = 1.7$ kA.

$$\frac{1}{p^2}\left(i\varepsilon\frac{\omega}{c}\frac{dE_z}{dr} - k\frac{l}{r}H_z\right)_{r=a-0}$$

$$= -\frac{1}{q^2}\left(i\frac{\omega}{c}\frac{dE_z}{dr} - k\frac{l}{r}H_z\right)_{r=a+0}. \qquad (2)$$

Using linearized equations of motion and continuity, we can obtain the constraint on the discontinuity of the derivative of E_z at the beam surface

$$\left\{\frac{dE_z}{dr}\right\}_{r=r_b} = -\frac{2eI_b}{\gamma^3 mur_b}\frac{q^2 E_z(r_b)}{(\omega - ku)^2}, \qquad (3)$$

where I_b is the beam current, u is the electron velocity, and $\gamma = (1 - u^2/c^2)^{-1/2}$ is the relativistic factor. Substituting conditions (2) and (3) into the expressions (1) and allowing for the conditions of continuity of E_z and H_z finally yields the dispersion equation for this system

$$\left\{\left[\frac{pF'_E(qa,qb)}{F_E(qa,qb)} + \frac{\varepsilon qJ'_l(pa)}{J_l(pa)}\right]\left[\frac{pF'_H(qa,qb)}{F_H(qa,qb)}\right.\right.$$

$$\left.\left. + \frac{qJ'_l(pa)}{J_l(pa)}\right] - \left[\frac{(\varepsilon-1)l\omega k}{cpqa}\right]^2\right\}(\omega - ku)^2$$

$$= \frac{2eI_b}{\gamma^3 mu}q^2\frac{F_E(qr_b,qb)}{F_E(qa,qb)}F_E(qa,qr_b)f(\omega,k), \qquad (4)$$

where

$$F_E(x,y) = I_l(x)K_l(y) - I_l(y)K_l(x),$$

$$F'_E(x,y) = I'_l(x)K_l(y) - I_l(y)K'_l(x),$$

$$F_H(x,y) = I_l(x)K'_l(y) - I'_l(y)K_l(x),$$

$$F'_H(x,y) = I'_l(x)K'_l(y) - I'_l(y)K'_l(x),$$

$$f(\omega,k) = \left[\frac{(\varepsilon-1)l\omega k}{cpqa}\right]^2 - \left[\frac{pF'_E(qa,qr_b)}{F_E(qa,qr_b)} + \frac{\varepsilon qJ'_l(pa)}{J_l(pa)}\right]$$

$$\times \left[\frac{pF'_H(qa,qb)}{F_H(qa,qb)} + \frac{qJ'_l(pa)}{J_l(pa)}\right].$$

In the absence of a beam ($I_b = 0$) Eq. (4) is the same as the well-known dispersion equation for the azimuthally asymmetric modes in a waveguide with a dielectric rod.[7]

Figure 1 shows the instability spectrum obtained by solving Eq. (4) for various azimuthal indices ($l = 0,1,2,3$). The beam parameters used for the calculations are typical of relativistic traveling-wave tubes. (Note that because of the influence of the Coulomb field the value $\gamma = 1.8$ taken for the given current and beam radius corresponds to an applied voltage of ≈ 470 kV). The value of ε is typical of dielectric rod antennas. The frequency at which the maximum spatial growth rate is achieved for the TEM_{11} mode depends on the waveguide radius. For the given ratio of rod and waveguide radii this maximum falls within the 3 cm wavelength range for $b \sim 2.0 - 2.5$ cm, which corresponds to a gap of 2.0–2.5 mm between the beam and the dielectric and a gain per unit length of 0.8–1.0 dB/cm. Therefore, both the geometry of the system and the gain are of the same order of magnitude as those of known experimental relativistic traveling-wave tubes and dielectric masers.

However, it can be seen that for these parameters the absolute maximum of the spatial growth rate is obtained for the TEM_{21} mode rather than for TEM_{11}, and that even for the TEM_{31} mode the growth rates are of the same order of magnitude as for TEM_{11} despite the much higher frequency. This can be attributed to the specific radial dependence of the transverse field components: for the TEM_{11} mode the transferred power is distributed over the entire cross section of the rod, whereas for the other modes it is concentrated to a larger or lesser degree near the surface. Thus, the same power cor-
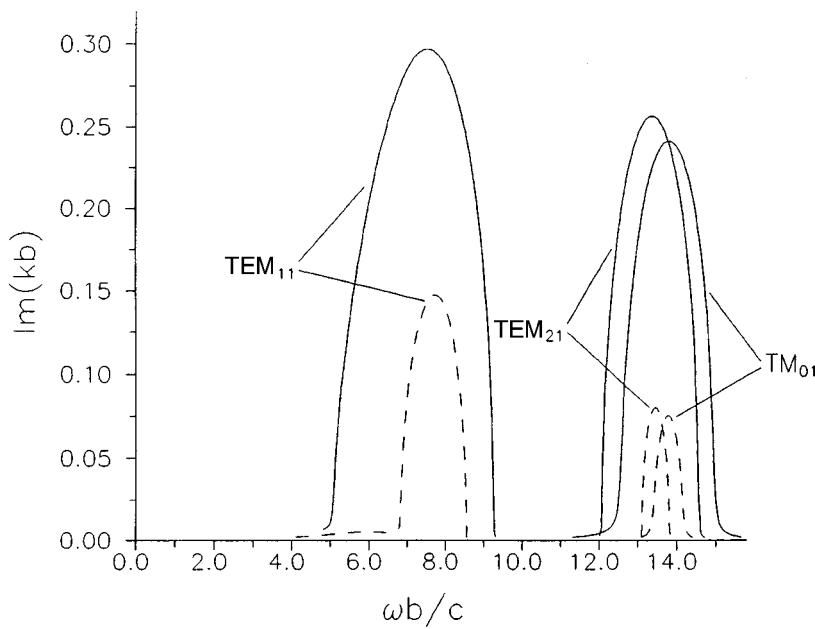
FIG. 2. As Fig. 1 for a thinner rod with $a/b=0.3$. Solid curves—$r_b/b=0.4$, dashed curves—$r_b/b=0.5$. The other parameters are the same as in Fig. 1.

responds to a smaller E_z component for the TEM_{11} mode.

The situation changes if the radius of the rod is reduced and the distance between the beam and its surface is increased. In an isolated dielectric rod, the TEM_{11} mode has no critical frequency, whereas a critical frequency does exist for the other modes and is determined by the thickness of the rod. Moreover, all the propagating modes have a surface field structure and phase velocities less than c. If the rod is surrounded by a conducting wall, critical frequencies exist for all the modes and these are determined by the wall diameter; in this case frequency ranges in which the phase velocity is greater than c are observed for all the modes. If the radius of the rod is smaller than the waveguide radius, the presence of a conducting wall will have no significant influence on the spectrum of waveguide modes in the region of slowed phase velocities. Consequently, the thicker the rod,

the further the TEM_{11} mode from the other modes in terms of the phase-matching frequency with the electron beam. This implies that the scale of localization of the field in the vacuum region near the surface of the rod may be considerably greater for the TEM_{11} mode than for the other modes, i.e., it will predominate in the instability spectrum of the system if the beam moves a large distance away from the dielectric.

Figure 2 shows the instability spectrum for the same current and electron energy but a smaller ratio $a/b=0.3$ for two values of the beam radius (for $r_b/b=0.4$ the value $\gamma=1.8$ corresponds to an accelerating voltage of 521 kV and for $r_b/b=0.5$ it corresponds to 494 kV). It can be seen that in this case the growth rate for the TEM_{11} mode predominates, especially for $r_b/b=0.5$. The gain profile for the TEM_{11} mode falls within the 3 cm range, for example for
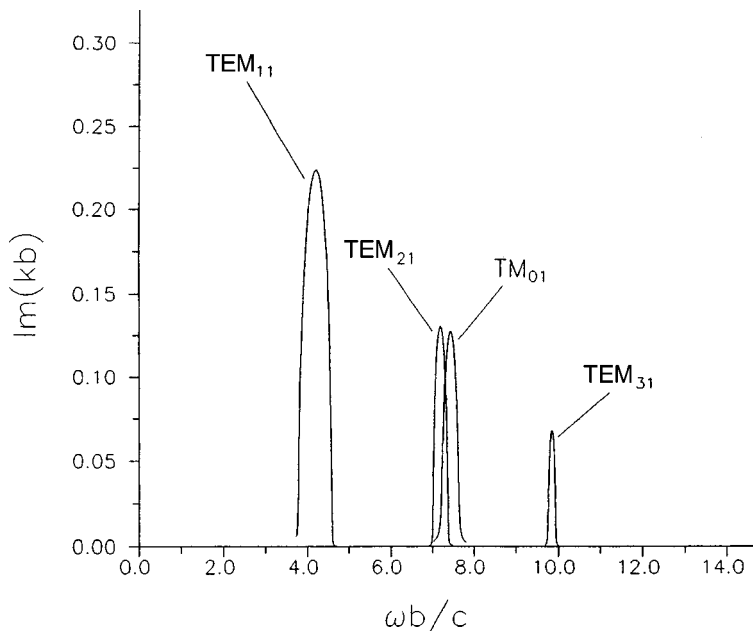
FIG. 3. As Fig. 1 for $\varepsilon=5$, $a/b=0.3$, $r_b/b=0.5$, $\gamma=1.4$, and $I_b=1$ kA.

$b = 3.5$ cm which corresponds to a gain per unit length of 0.74 dB/cm for a 3.5 mm beam–dielectric gap (solid curve) and 0.37 dB/cm for a 7 mm gap (dashed curve).

The last figure for the gain is fairly low, so this geometry would be more acceptable for smaller waveguide radii and therefore shorter wavelengths (say, the gain per unit length is doubled when b is halved and the frequency is 20 GHz). However, it should be noted that the TEM_{11} mode may dominate in the 3 cm range at a lower electron energy and higher permittivity of the rod material. Figure 3 gives the results of calculations for $\varepsilon = 5$; the beam parameters correspond to a voltage of 265 kV. Here the frequency at which the growth rate of the TEM_{11} mode is highest is 10 GHz for $b = 2$ cm. In this case, the beam–dielectric gap is 4 mm and the gain 0.97 dB/cm. These are normal values for a traveling-wave tube amplifier although the gain profile in this case is considerably narrower than that for the parameters in Figs. 1 or 2 (for the solid curve).

To conclude, the dominant azimuthally asymmetric mode may predominate in the spectrum of electron beam instability in the rod slow-wave system. Moreover, typical gains and gain profiles for relativistic traveling-wave tubes are achieved for normal beam parameters and geometric dimensions for these systems. In addition, the use of a rod antenna as a natural means of coupling radiation out of this system can substantially increase the scope for controlling the microwave output beam at high powers.

[1] J. A. Nation, Appl. Phys. Lett. **17**, 491 (1970).
[2] N. I. Gunina, S. D. Korovin, S. D. Polevin *et al.*, Pis'ma Zh. Tekh. Fiz **14**, 1425 (1988) [Sov. Tech. Phys. Lett. **14**, 621 (1988)].
[3] E. P. Garate, A. Fisher, and W. T. Main, IEEE Trans. Plasma Sci. **18**, 831 (1990).
[4] T. J. Davis, L. Schächter, and J. A. Nation, IEEE Trans. Plasma Sci. **22**, 504 (1994).
[5] A. S. Shlapakovskii, Proc. SPIE **2557**, 404 (1995).
[6] C. H. Walter, *Traveling Wave Antennas* (Dover, New York, 1965; Énergiya, Moscow, 1970, 448 pp.
[7] Yu. A. Ilarionov, S. B. Raevskiĭ, and V. Ya. Smorgonskiĭ, *Calculations of Corrugated and Partially Filled Waveguides* [in Russian], Sovetskoe Radio, Moscow (1980), 200 pp.

Translated by R. M. Durham

Turbulent diffusion of passive impurities

S. N. Gordienko and S. S. Moiseev

L. D. Landau Institute of Theoretical Physics, Russian Academy of Sciences, Chernogolovka, Moscow Province; Institute of Space Research, Russian Academy of Sciences, Moscow
(Submitted November 10, 1998)
Pis'ma Zh. Tekh. Fiz. **25**, 51–56 (April 12, 1999)

It is shown that in turbulent flows with a divergent Loĭtsyanskiĭ integral, the coefficient of turbulent diffusion may be determined by pulsations whose scales are comparable with those of the liquid itself rather than by the largest-scale turbulent vortices. This is a new physical mechanism which must be taken into account to explain the experimentally observed phenomenon of impurity ''hyperdiffusion'' in turbulent media. The contribution of large-scale pulsations increases substantially with the onset of turbulence regimes which are accompanied by the spontaneous generation of structures comparable with the dimensions of the liquid. © *1999 American Institute of Physics.* [S1063-7850(99)00804-6]

At present considerable attention is being focused on studying methods of controlling turbulent momentum, heat, and mass transfer processes in order to minimize the drag accompanying the motion of objects when liquids are transported through pipes, to achieve more uniform heating of liquid volumes, or more uniform mixing of various chemical components.[1] The type of turbulence is fundamentally important when studying the diffusion of passive impurities, as in the atmosphere, for example. In order to estimate the coefficient of turbulent diffusion D_l on scales of the order l we can write $D_l \sim v_l l$, where v_l is the characteristic velocity of turbulent pulsations on scales of the order l. For a Kolmogorov spectrum we have $v_l \sim l^{1/3}$, for a turbulence spectrum with fixed helicity we have $v_l \sim l^{1/2}$, and for turbulence with a fixed rate of dissipation of the helicity $v_l \sim l^{2/3}$ (Ref. 2), which yield $D_l \sim l^{4/3}$, $D_l \sim l^{3/2}$, and $D_l \sim l^{5/3}$, respectively. If the largest scale of the turbulent vortices is of the order of l_c, the coefficients of turbulent diffusion are estimated as $D \sim l_c^{4/3}$, $D \sim l_c^{3/2}$, and $D \sim l_c^{5/3}$, respectively.

This estimate of D implicitly assumes that the velocity–velocity correlation function decays fairly rapidly when $l \gg l_c$ and pulsations having scales larger than l_c make no contribution to the transfer coefficient. A similar situation arises whenever the Loĭtsyanskiĭ integral converges.[3] However, the convergence or divergence of the Loĭtsyanskiĭ integral depends on the method of excitation of the turbulence[4] and in cases where this integral diverges, estimates for the coefficients of turbulent diffusion and thermal conductivity must be fundamentally reexamined because of the contribution of long-wavelength pulsations with $l > l_c$. This aspect is considered in the present paper.

1. Since we are only interested in liquid flows with large Reynolds numbers (Re≫1), we shall analyze the Navier–Stokes equation with the external force $\mathbf{f}(\mathbf{r},t)$:

$$\frac{\partial \mathbf{v}}{\partial t} + (\mathbf{v}\nabla)\mathbf{v} = -\nabla p + v\Delta\mathbf{v} + \mathbf{f}(\mathbf{r},t), \quad \text{div } \mathbf{v} = 0, \quad (1)$$

$$\langle\mathbf{f}(\mathbf{r},t)\rangle = 0, \quad \langle\mathbf{f}(\mathbf{r}_1,t_1)\mathbf{f}(\mathbf{r}_2,t_2)\rangle = f_0^2 K\left(\frac{t_1-t_2}{\tau_0}, \frac{\mathbf{r}_1-\mathbf{r}_2}{r_0}\right), \quad (2)$$

where K describes the correlation properties of the force $\mathbf{f}$ which sets the liquid in motion, and from the definition of f_0^2

$$\int K\left(\frac{t}{\tau_0}, \frac{\mathbf{r}}{r_0}\right) d\mathbf{r}\, dt = r_0^3 \tau_0.$$

Without loss of generality we can assume that the force $\mathbf{f}$ is purely sinusoidal, having included a potential component in the pressure gradient.

2. In Ref. 4 the present authors established that, depending on the force which sets the liquid in motion, three fundamentally different turbulent steady states may occur in the liquid, and we determined the dimensionless parameters responsible for the transition from one state to another: $\gamma = f_0 \tau_0^2 / r_0$ and $\Gamma = \gamma^{4/3}$ Re. It was shown that for $\gamma \ll 1$ and $\Gamma \ll 1$, the Kolmogorov spectrum $E(k) \sim 1/k^{5/3}$ forms in the inertial interval. In the transition to turbulent flows under the action of forces f_0 of larger amplitude, i.e., in going to $\gamma \ll 1$ and $\Gamma \gg 1$, a section of the spectrum with $E(k) \sim 1/k^2$ appears near the viscous interval, ''cutting off'' the Kolmogorov spectrum from the viscous interval. A further increase in the amplitude of the force f_0, i.e., a transition to $\gamma \gg 1$ and $\Gamma \gg 1$, has the result that the entire inertial interval is the ''occupied'' spectrum $E(k) \sim 1/k^2$, and outside the inertial interval large-scale structures begin to be generated with characteristic scales up to $\gamma^{2/5} r_0$. In the limit $\Gamma \ll 1$ the power dissipated per unit mass of liquid does not depend on the viscosity, in accordance with the Kolmogorov theory, but in the transition to turbulent regimes with $\Gamma \gg 1$ the viscous losses begin to depend on the viscosity of the liquid. When turbulence is excited by this method, the Loĭtsyanskiĭ integral diverges for any values of the parameters γ and Γ. Thus, three different types of flows are created for which the coefficient of turbulent diffusion (thermal diffusivity) behaves differently. We shall analyze these three cases separately.

3. Let us assume that $\gamma \ll 1$ and $\Gamma \gg 1$. Then, from Ref. 4 we have

$$\langle (\mathbf{v}(\mathbf{r},t) - \mathbf{v}(0,t))^2 \rangle = C_1 (f_0^2 \tau_0 r)^{2/3} \quad \text{for} \quad \lambda_0 \ll r \ll r_0, \tag{3}$$

$$\langle \mathbf{v}(\mathbf{r},t)\mathbf{v}(0,t) \rangle = C_2 \left(\frac{f_0^2 r_0^3 \tau_0}{r^2} \right)^{2/3} \quad \text{for} \quad r_0 \ll r, \tag{4}$$

where C_1 and C_2 are universal constants and λ_0 is the viscous length. Thus, the following estimates hold for the coefficient of turbulent diffusion

$$D_l \sim f_0^{2/3} \tau_0^{1/3} l^{4/3} \quad \text{for} \quad \lambda_0 \ll l \ll r_0$$

$$\text{and} \quad D_l \sim f_0^{2/3} \tau_0^{1/3} r_0 l^{1/3} \quad \text{for} \quad r_0 \ll l. \tag{5}$$

4. We shall now consider the case $\gamma \ll 1$, $\Gamma \gg 1$. In this case the velocity correlation differs slightly from that[4] given by Eqs. (3) and (4):

$$\langle (\mathbf{v}(\mathbf{r},t) - \mathbf{v}(0,t))^2 \rangle = C_0 f_0 r \quad \text{for} \quad \lambda_0 \ll r \ll f_0 \tau_0^2, \tag{6}$$

$$\langle (\mathbf{v}(\mathbf{r},t) - \mathbf{v}(0,t))^2 \rangle = C_1 (f_0^2 \tau_0 r)^{2/3} \quad \text{for} \quad f_0 \tau_0^2 \ll r \ll r_0, \tag{7}$$

$$\langle \mathbf{v}(\mathbf{r},t)\mathbf{v}(0,t) \rangle = C_2 \left(\frac{f_0^2 r_0^3 \tau_0}{r^2} \right)^{2/3} \quad \text{for} \quad r_0 \ll r, \tag{8}$$

where C_0 is a universal constant. The behavior of the coefficient of turbulent diffusion on different length scales is given by

$$D_l \sim f_0^{1/2} l^{3/2} \quad \text{for} \quad \lambda_0 \ll l \ll f_0 \tau_0^2, \tag{9}$$

$$D_l \sim f_0^{2/3} \tau_0^{1/3} l^{4/3} \quad \text{for} \quad f_0 \tau_0^2 \ll l \ll r_0$$

$$\text{and} \quad D_l \sim f_0^{2/3} \tau_0^{1/3} r_0 l^{1/3} \quad \text{for} \quad r_0 \ll l. \tag{10}$$

5. When $\gamma \gg 1$ and $\Gamma \gg 1$, the velocity correlation function is given by[4]

$$\langle (\mathbf{v}(\mathbf{r},t) - \mathbf{v}(0,t))^2 \rangle = C_0 f_0 r \quad \text{for} \quad \lambda_0 \ll r \ll r_0, \tag{11}$$

$$\langle \mathbf{v}(\mathbf{r},t)\mathbf{v}(0,t) \rangle = C_3 \left(\frac{f_0^2 r_0^3}{r} \right)^{1/2} \quad \text{for} \quad r_0 \ll r \ll \gamma^{2/5} r_0, \tag{12}$$

$$\langle \mathbf{v}(\mathbf{r},t)\mathbf{v}(0,t) \rangle = C_2 \left(\frac{f_0^2 r_0^3 \tau_0}{r^2} \right)^{2/3} \quad \text{for} \quad \gamma^{2/5} r_0 \ll r, \tag{13}$$

where C_3 is a universal constant. In this case, the coefficient of turbulent diffusion is given by

$$D_l \sim f_0^{1/2} l^{3/2} \quad \text{for} \quad \lambda_0 \ll l \ll r_0, \tag{14}$$

$$D_l \sim f_0^{1/2} r_0^{3/4} l^{3/4} \quad \text{for} \quad r_0 \ll l \ll \gamma^{2/5} r_0,$$

$$D_l \sim f_0^{2/3} \tau_0^{1/3} r_0 l^{1/3} \quad \text{for} \quad \gamma^{2/5} r_0 \ll l. \tag{15}$$

6. It follows from expressions (3), (4), (6)–(8), and (11)–(13) that for this method of exciting turbulence the maximum scale of the turbulent vortices is of order r_0. However, as a result of the slow decay of the velocity correlation function for $l \gg r_0$ long-wavelength pulsations make a decisive contribution to the turbulent diffusion coefficient. If $\gamma \ll 1$, i.e., the turbulence is not accompanied by the spontaneous creation of structures, the coefficient of turbulent dif-

fusion is determined by the largest-scale pulsations, of the same size as the dimension R of the vessel containing the liquid, i.e., this coefficient is given by

$$D \sim f_0^{2/3} \tau_0^{1/3} r_0 R^{1/3} = D_{\gamma \ll 1} (R/r_0)^{1/3} \quad \text{for} \quad R \gg r_0, \tag{16}$$

where $D_{\gamma \ll 1} = f_0^{2/3} \tau_0^{1/3} r_0^{4/3}$ is the diffusion coefficient determined by the largest-scale vortices.

If $\gamma \gg 1$ holds, i.e., if structures are spontaneously generated, in the limit $R \gg \gamma^{2/5} r_0$ the size of the vessel is larger than the scale of the incipient structures and the coefficient of turbulent diffusion is determined as before by (16):

$$D \sim f_0^{2/3} \tau_0^{1/3} r_0 R^{1/3} = \gamma^{1/6} D_{\gamma \gg 1} (R/r_0)^{1/3}$$

$$\text{for} \quad R \gg \gamma^{2/5} r_0, \tag{17}$$

where $D_{\gamma \gg 1} = f_0^{1/2} r_0^{3/2}$ is the coefficient of turbulent diffusion as a result of the largest-scale vortices when $\gamma \gg 1$.

In cases where $\gamma \gg 1$ holds but the largest scale of the resulting structures can exceed the size of the vessel $R \ll \gamma^{2/5} r_0$, the main contribution to the turbulent diffusion is made by structures having scales of the order R and

$$D \sim f_0^{1/2} r_0^{3/4} R^{3/4} = D_{\gamma \gg 1} (R/r_0)^{3/4} \quad \text{for} \quad r_0 \ll R \ll \gamma^{2/5} r_0. \tag{18}$$

Consequently, in the range of smaller scales of the largest turbulent vortex the coefficient of turbulent diffusion increases rapidly (faster than l) whereas in the range of larger scales, this coefficient continues to increase but slowly (slower than l) because the total turbulent diffusion coefficient is determined by the dimensions of the liquid itself.

An important consequence of expressions (16)–(18) is that for the same diffusion coefficients for the largest-scale vortices (when $D_{\gamma \ll 1}$ and $D_{\gamma \gg 1}$ are the same), the true diffusion coefficients may differ by a large factor. Note that the contribution of long-wavelength pulsations for turbulent regimes accompanied by the spontaneous generation of structures, as given by expressions (17) and (18), is always greater than the contribution of the long-wavelength component for turbulent flows which do not lead to self-organization. In fact, expression (17) contains an additional factor $\gamma^{1/6}$ compared with (16) and expression (18) contains the factor $(R/r_0)^{3/4}$ compared with $(R/r_0)^{1/3}$ in expression (16).

It follows from the above reasoning as applied to the physics of impurity transport in the atmosphere that a knowledge of the scale and velocity of the turbulent pulsations in vortices can be used to obtain a lower estimate of the turbulent diffusion coefficient of impurities. However, the true value of the turbulent diffusion coefficient is many times larger than this lower bound (i.e., hyperdiffusion takes place) and in order to determine this, we also need to study the type of turbulent flow, which can explain the dependence on the propagation velocity of contaminants on specific conditions.

[1] E. R. Eckert *et al.*, Int. J. Heat Mass Transf. **40**, 3729 (1997).
[2] S. Moiseev and O. Onishenko, Physica B **228**, 83 (1996).
[3] L. D. Landau and E. M. Lifshits, *Fluid Mechanics*, 3rd ed. (Pergamon Press, Oxford, 1972) [Russ. original, later ed., Nauka, Moscow, 1986].
[4] S. S. Gordienko and S. N. Moiseev, JETP Lett. **68**, 204 (1998)].

Translated by R. M. Durham

Anomalous phenomena

G. E. Skvortsov

St. Petersburg State University

The laws of large departures from equilibrium and the laws governing structural transitions indicated previously by the author are used as the basis for discussing anomalous phenomena. Their main properties are described, a classification is put forward, a simple model is proposed to describe an anomalous phenomenon, and several families of possible phenomena are indicated. © *1999 American Institute of Physics.* [S1063-7850(99)00904-0]

Anomalous phenomena occurring in nature, achieved experimentally, and used in technologies are attracting considerable interest because of their unusual nature, their counter-intuitive character, and also because of the desire to interpret the nature of the phenomenon and use it to effectively.

Ball lightning, although a fairly well-known anomalous phenomenon, remains mysterious in many respects despite long-term efforts to identify its nature and reproduce a similar phenomenon in the laboratory.[1–3] This example shows how difficult it is to investigate an anomalous phenomenon and unravel its mechanism.

A fairly large number of anomalous phenomena have now been observed under laboratory conditions, although a purposeful search for and discussion of the general properties of anomalous phenomena has to date not seemed possible.

The present author recently identified a system of laws of strong nonequilibrium, i.e., the qualitative boundary, abnormality, and alternation of abnormality,[4–6] and also established laws governing structural transitions,[7,8] which allow us to discuss anomalous phenomena for various systems in general terms. It becomes possible to specifically search for, observe, and study anomalous phenomena on a regular basis.

In the present paper classes of anomalous phenomena are described and a more detailed analysis is made of the phenomenon of anomalous relaxation. Families of possible anomalous phenomena suitable for observation and application are indicated.

1. We shall outline a wide range of anomalous phenomena which are fairly well-known.

First, there is ball lightning and its numerous imitations.[1,2]

The phenomena and effects of anomalous relaxation constitute a large family of anomalous phenomena. Anomalous relaxation is a process in which the internal degrees of freedom of particles are excited above equilibrium and after transformation, they are deactivated as a whole range of anomalous effects, including the laser effect.

Anomalous relaxation has been studied fairly comprehensively for shock waves in gases[9] and shock waves activated by a glow discharge.[10,11]

Various anomalous phenomena which can be fruitfully discussed using the laws of nonequilibrium include erosion discharges,[12–14] the plasma-ion method of water electrolysis,[15,16] cold nuclear fusion, and high-temperature superconductors.

These laws can also be usefully applied to fairly well-studied anomalous phenomena such as anomalous photoconductivity,[17] and also to those anomalous phenomena accorded the status of discoveries in Ref. 18. These include plasma neutron radiation (discovery No. 3, I. V. Kurchatov *et al.*), the formation of a high-temperature plasma in an rf discharge (discovery No. 87, P. L. Kapitsa), the self-focusing effect (discovery No. 67, G. A. Askar'yan), the multifocus property of a wave beam (discovery No. 147, A. M. Prokhorov *et al.*), the formation of hydrogen-saturated zones (discovery No. 313, V. N. Shapovalov and V. Yu. Karpov), the laws governing the interaction of x-rays with atoms (discovery No. 297, A. P. Lukirskiĭ and T. M. Zimina), the phenomena of large reversible strains (discovery No. 239, G. V. Kurdyumov and L. G. Khandros), the phenomenon of catalyst modification (discovery No. 306, S. Z. Roginskiĭ *et al.*), bioelectrocatalysis (discovery No. 311, I. V. Berezin *et al.*), the law of self-regulation in cellular excitation (discovery No. 17, D. N. Nasonov), and the phenomenon of intercellular remote electromagnetic interactions (discovery No. 122, V. P. Kaznacheev *et al.*).

It is useful to apply the laws of nonequilibrium to differently organized cycles of the second kind of energy conversion (A. B. Serogodskiĭ and G. V. Skornyakov).

2. Even though each one is different, the wide variety of anomalous phenomena can be categorized using the laws expounded in Refs. 4–8 We note the general properties of anomalous phenomena and the significant indicators of the different classes of these phenomena.

2.1. Anomalous phenomena occur states and regimes far from equilibrium; they cannot occur as a result of weak disturbances of quasiequilibrium systems.

The wide variety of anomalous phenomena can be subdivided into classes according to the values, character, and number of nonequilibrium factors, or measures of action.

The first class includes single-factor effects of a resonant nature which reveal an anomalous initial structure. The active measures of action G_a are small and the resonance criterion has values close to one, res ≈ 1.

Effects of this type include anomalous photoconductiv-

ity, various discoveries (Nos. 165, 175, 191, and 225; Ref. 18), anomalies of kinetic coefficients,[5] and the effect of a universal structural transition quantum[19] (12.5 K).

2.2. As a result of the qualitative boundary law, anomalous phenomena occur as threshold processes.

A second class of anomalous phenomena can be identified by thresholds, typically exhibiting abrupt thresholds for the beginning and end, $G_a \approx 1$ and also an inverse stage, in addition to be being single-factor effects. In this case, an anomalous structure forms during the process, unlike the first class of anomalous phenomena. Typical phenomena of this second class include negative differential susceptibility effects (such as diffusion, conductivity, and viscosity), self-focusing of electromagnetic beams, plasma filamentation, and the first stage of anomalous relaxation in a shock wave. This class must also include chemical vibrations and many phenomena analyzed by synergetics.

2.3. The formation of anomalous phenomena in the second and subsequent classes is caused by structural transitions with a defined inversed–anomalous stage.

The third class of anomalous phenomena is characterized by two or three successive structural transitions. In this case, the process of increasing action includes internal factors and the anomalous phenomena at the stage of the second and third structural transition reveal an increased range of anomalous effects.

A typical anomalous phenomenon of the third class is anomalous relaxation of the second and third stage. This class includes erosion discharges and also plasma-ion electrolysis of water.

2.4. In general, unexpected results which are difficult to predict are obtained when two (and especially three) structural transitions take place simultaneously under the action of two (three) independent factors.

This type of anomalous phenomenon belongs to the fourth class. It is easy to specify a set of possible anomalous phenomena in this class by combining different factors. However, their results can only be predicted with a low probability.

There are some cases where, in the presence of several factors and structural transitions, the result of an anomalous phenomenon is fairly predictable. An example is bioelectrocatalysis in which the most effective biocatalyst, an enzyme, being inserted in the electrochemical reaction chain, increases the reaction rate millions of times. This anomalous phenomenon removes the barrier between living systems and electrotechnical ones. Natural anomalous phenomena (such as tornados, ball lightning, and unidentified flying objects) generally occur as a result of several important factors and several structural transitions taking place simultaneously and successively. Consequently it is impossible to predict their occurrence, nature, and resultant effects with sufficient certainty. These phenomena form a superclass.

2.5. In accordance with the law of alternating abnormality, all anomalous phenomena take place ''at intervals,'' i.e., in relatively small intervals of measures of action which alternate with intervals of normal behavior of the process.

The law of alternating abnormality is a specific refinement of the law of alternating nonequilibrium.[4,6] It prescribes the alternation of properties and the behavior of quantities as a function of the action factor, time, and space, as is found for anomalous relaxation in shock waves,[4,6] for striations, and temporal oscillations in chemical reactions.

2.6. A common property of anomalous phenomena is the presence of an anomalous structure (particular to each object of the anomalous phenomenon); a more anomalous structure, up to the exotic, corresponds to a higher class of anomalous phenomena.

We know[4,5] that a structure is formed by structure-kinetic elements and the coupling between them. Anomalous effects have anomalous structure-kinetic elements: electromagnetic turbines, electron traps, exciton–impurity complexes, dynamic domains, hydrogen-saturated zones, models of ball lightning invoking exotic clusters,[3] and so on.

Bearing in mind the transient structure of the structural transitions,[7] we note some general properties of anomalous structure-kinetic elements and their coupling.

Generally these elements are complexes with a strengthened coupling between them, activated, metastable, and capable of absorbing external energy and deactivating under saturation. As a result of their metastable nature, the structure of objects of anomalous phenomena is extremely variable, even under small influences. In general the variety of structures in strong nonequilibrium is extremely large; living matter and the multilevel physical world known to us, being of nonequilibrium origin, only realizes this variety to a small extent.

Among the various properties of anomalous phenomena specified, special mention should be made of the capacity to intensively absorb and concentrate energy. On account of its universal nature, this property is essentially an energy concentration law.

3. We shall demonstrate some general properties of anomalous phenomena for the fairly typical case of anomalous relaxation.

The abrupt threshold for anomalous relaxation with increasing action is determined by the resonant and amplitude energy relations

$$\varepsilon_i + e = \alpha \varepsilon_a, \quad \alpha \approx 1, \tag{1}$$

$$n_1\left(\frac{\gamma_1}{2}kT_1 + \frac{n_i}{n_1}\varepsilon_i + e\right) \geqslant n_2\left(\frac{\gamma_2}{2}kT_2 + \frac{n_a}{n_2}\varepsilon_a\right), \tag{2}$$

where ε_i, e, and ε_a are the initial excitation energy, the energy of the external action on the structure-kinetic elements, and the activation energy, $n_{1,2}$, n_i, and n_a are the particle number densities before and after the action, preliminarily excited, and activated structure-kinetic elements, $\gamma_{1,2}$ are the numbers of degrees of freedom, and $T_{1,2}$ are the initial and final temperatures.

A regular structural transition occurs when the threshold is reached. For a shock wave this is manifest as branching of the front (in gases,[9] in a glow discharge,[11] and in metals[20]).

A slight increase in the action beyond the threshold e_c transfers the system to an anomalous regime. This regime is characterized by strong inhomogeneity of the density and other quantities (striations, filamentation, microexplosions, cores), anomalies of radiation spectra (between infrared and

x-ray), an increase in viscosity, and other effects associated with high material activity. These include an appreciable increase in energy above that dissipated in the plasma ion electrolysis of water,[15,16] the failure of a core which burns through metals to burn tracing paper,[12] and so on.

When the action increases above the threshold e_c by a resonance width the anomalous regime is replaced by a regular one, which is surprising if we are not familiar with the law of alternating abnormality. As the action increases further until conditions (1) and (2) are satisfied for the second structural level, a threshold transition takes place to a second anomalous regime, and so on.[4,6]

Typical structure-kinetic elements for anomalous relaxation in gases are excited M* molecules, M_2^+, M_2^+* biomolecular ions, and more intricate complexes.[21]

4. We shall now briefly discuss a phenomenological model of an experimentally reproducible anomalous phenomenon of the first–third class, such as a long-lived Protasevich plasma formation.[21]

Taking into account the laws of nonequilibrium, the laws governing structural transitions, and the main properties of anomalous phenomena, we reflect these by means of an expression for the determining quantities

$$\Phi(g,y) = \sum_{n,m=0}^{n+m \leqslant 3} b_{nm} g^n y^m \bigg/ \sum_{n,m=0}^{n+m \leqslant 3} c_{nm} g^n y^m. \qquad (3)$$

Here g and y are action factors, and b_{nm} and c_{nm} are coefficients determined from general constraints and experimental data. One of the action factors may be time, as in the case of chemical reactions, and another may be the field action (a possible radical change in the result of the reaction depending on the category of an anomalous phenomenon).

Expression (3) was examined for a single factor (for $y=0$) in Refs. 7 and 8. The relevant dependence can have four extrema corresponding to two sequences of structural transitions. When the maxima are close, the wells between them will reflect the existence of a metastable stage of the anomalous phenomenon.

Under the action of two factors, expression (3) may have sixteen extrema, which reflects the highly complex and multivalued pattern of an anomalous phenomenon and the variety of its results. This also implies an appreciable increase in the number of anomalous effects accompanying the anomalous phenomenon. These indications are also consistent with the characteristics of anomalous phenomena observed experimentally and in nature, which motivates the use of expression (3) to describe anomalous phenomena.

5. We note several families of possible anomalous phenomena.

First we note that, as follows from the general properties of anomalous phenomena, the number of possible anomalous phenomena is considerably greater than the number of normal effects but the region of regimes of occurrence of anomalous phenomena is much smaller, i.e., anomalous phenomena occur considerably less frequently than normal effects. The first class are anomalous phenomena caused by resonant action on structure-kinetic elements. These are observed at fairly high action intensities as an abrupt change (a

jump or a peak) in the kinetic coefficients. These effects were discussed in Ref. 5. For instance, when a gas is exposed to the action of radiation at a frequency equal to half the dissociation energy and an intensity sufficient to excite a quarter of the molecules, anomalies of the viscosity, electrical and thermal conductivity will be observed.

A family of anomalous relaxation phenomena and effects for shock waves in gases was predicted by the author on the basis of the qualitative boundary law. These were observed and studied in Ref. 9, and extended to the case of a glow discharge.[11,10] A whole range of predictions confirmed experimentally indicates the predictive capabilities of the author's criterion (1,2) (Ref. 22), which can undoubtedly be used to observe new anomalous relaxation effects.

A set of energy concentration anomalous phenomena can usefully be identified. The family of self-focusing phenomena has been studied most comprehensively (G. A. Askar'yan, A. M. Prokhorov et al.). Filamentation is another similar effect. Among the many possible effects we note self-focusing of a beam in a solid insulator, which may be observed as a very thin channel formed by a beam of fairly large diameter.

The laws of nonequilibrium can be used to predict highly exotic anomalous phenomena and provide a qualitative description. For example, a family of mass$\rightleftarrows$field structural transitions can be considered for various fields.

[1] I. P. Stakhanov, *The Physical Nature of Ball Lightning* [in Russian], Moscow (1996), 262 pp.

[2] *Ball Lightning in the Laboratory* [in Russian], Moscow (1994), 256 pp.

[3] O. A. Sinkevich, in *The Physical Nature of Ball Lightning*, edited by I. P. Stakhanov, [in Russian], Moscow (1996), pp. 238–260.

[4] G. E. Skvortsov, Pis'ma Zh. Tekh. Fiz **16**(17), 15 (1990) [Sov. Tech. Phys. Lett. **16**, 1647 (1990)].

[5] G. E. Skvortsov, Pis'ma Zh. Tekh. Fiz **23**(6), 85 (1997); **23**(7) 23 (1997) [Tech. Phys. Lett. **23**, 647 (1997); **23**, 246 (1997)].

[6] G. E. Skvortsov, Pis'ma Zh. Tekh. Fiz **23**(10), 17 (1997) [Tech. Phys. Lett. **23**, 383 (1997)].

[7] G. E. Skvortsov, Pis'ma Zh. Tekh. Fiz. **24**(3), 80 (1998) [Tech. Phys. Lett. **24**, 117 (1998)].

[8] G. E. Skvortsov, Pis'ma Zh. Tekh. Fiz **24**(19), 7 (1998) [Tech. Phys. Lett. **24**, 749 (1998)].

[9] G. I. Mishin, A. P. Bedin, N. I. Yushchenkova, G. E. Skvortsov, and A. P. Ryazin, Zh. Tekh. Fiz **51**, 2315 (1981) [Sov. Phys. Tech. Phys. **26**, 1363 (1981)].

[10] A. I. Klimov, A. Yu. Gridin, and G. I. Mishin, in *Ball Lightning in the Laboratory* [in Russian], Moscow (1994), pp. 175–183.

[11] A. I. Klimov, in *Proceedings of the Third Conference on Physics and Gasdynamics of Shock Waves*, Vladivostok, 1989, Part 1 [in Russian], pp. 230–233.

[12] R. F. Avramenko, V. I. Nikolaeva, and L. P. Poskacheeva, in *Ball Lightning in the Laboratory* [in Russian], Moscow (1994), pp. 15–56.

[13] V. L. Bychkov, A. Yu. Gridin, and A. I. Klimov, *ibid.*, pp. 66–72.

[14] S. E. Emelin, V. S. Semenov, A. I. Eĭkhval'd, and A. K. Khassani, *ibid.* pp. 87–95.

[15] Yu. A. Beklemeshev, *Application of Effective Water Treatment Technologies* [in Russian], Krasnodar (1988).

[16] B. F. Lyakhov, Zh. Fiz. Khim. **72**, 765 (1998).

[17] M. I. Korsunskiĭ, *Anomalous Photoconductivity* Wiley, New York (1973); Russ. original, Moscow (1972), 192 pp.

[18] Yu. P. Konyushaya, *Discoveries of Soviet Scientists* [in Russian], Moscow (1988) Part. 1, 477 pp.; Part. 2, 232 pp.

[19] *Systems of Singular Temperature Points in Solids* [in Russian], Moscow (1986), 270 pp.

[20] A. G. Ivanov, S. A. Novikov, and V. A. Sinitsyn, *Strength and Shock Waves* [in Russian], Sarov (1996), p. 64.

[21] E. T. Protasevich, *Cold Nonequilibrium Plasma* [in Russian], Tomsk (1997), 241 pp.

[22] G. E. Skvortsov, Pis'ma Zh. Tekh. Fiz **9**, 744 (1983) [Sov. Tech. Phys. Lett. **9**, 320 (1983)].

Translated by R. M. Durham

Influence of screening on calculations on the total energy of calcium oxide

V. A. Drozdov, V. V. Pozhivatenko, and M. A. Drozdov

Odessa Institute of Ground Forces
(Submitted August 31, 1998)
Pis'ma Zh. Tekh. Fiz. **25**, 64–68 (April 12, 1999)

A unified formulation of a method which conserves the pseudopotential norm and the electron density functional is used to calculate the total energy and the equilibrium atomic volume of calcium oxide. Various methods of screening the pseudopotential are considered as a fitting procedure. © *1999 American Institute of Physics.* [S1063-7850(99)01004-6]

In order to determine the total energy, the equation for the crystal ground state

$$\left[-\frac{1}{2}\nabla^2 + W^{\text{BHS}}(\mathbf{r}) + W^H(\mathbf{r}) + W^{\text{XC}}(\mathbf{r}) \right] \Psi_{\mathbf{k}}(\mathbf{r})$$

$$= E_{\mathbf{k}}\Psi_{\mathbf{k}}(\mathbf{r}), \tag{1}$$

where $\Psi_{\mathbf{k}}$ is the wave function, and $W^{\text{BHS}}(\mathbf{r})$, $W^H(\mathbf{r})$, and $W^{\text{XC}}(\mathbf{r})$ are the Bachelet–Hamann–Schlüter pseudopotential,[1] the Hartree potential, and the exchange correlation potential, respectively, must be solved jointly with the equations

$$\nabla^2 V^H(r) = -4\pi\rho(r), \tag{2}$$

$$W^{\text{XC}}(r) = \delta E^{\text{XC}}[\rho(r)]/\delta\rho(r), \tag{3}$$

$$\rho(r) = \sum_{i=1}^{M} |\Psi_i(r)|^2. \tag{4}$$

Here $\rho(r)$ is the electron density, M is the number of electrons, and E^{XC} is the exchange correlation energy.

In a combined formalism of the electron density functional theory and the norm-conserving pseudopotential the total energy is given by[2]

$$E = \frac{1}{N}\sum_{\mathbf{k}} E_{\mathbf{k}} - E_H + E_{xc}E_{\text{es}} + \alpha_1 z, \tag{5}$$

where the first term is the sum over all occupied electronic states, N is the number of atoms of different species per unit cell, E_{xc} are the exchange correlation contributions which are calculated using formulas which approximate the Nozieres–Pines expression by Chebyshev polynomials:[3]

$$E_{xc} = \Omega\sum_{\mathbf{g}} \left[\varepsilon_{xc}(\mathbf{g}) - W_{xc}(\mathbf{g}) \right]\rho(\mathbf{g}), \tag{6}$$

where Ω is the volume of a unit cell, ε_{xc} is the exchange correlation energy density, and $\rho(\mathbf{g})$ is the Fourier transform of the electron density. The electrostatic energy E_{es} for compounds with two species of atoms was calculated using formulas given in Ref. 4. The Hartree term is given by

$$E_H = \frac{\Omega}{2}\sum_{\mathbf{g}} \frac{4\pi}{g^2} |\rho(\mathbf{g})|^2. \tag{7}$$

For the non-Coulomb component of the electron–ion interaction we have

$$\alpha_1 = \lim_{\mathbf{g}\to 0}\left\{ W_{\text{loc}}(\mathbf{g}) + \frac{8\pi z}{\Omega g^2} \right\}, \tag{8}$$

where $W_{\text{loc}}(\mathbf{g})$ is the Fourier transform of the local component of the first-principle Bachelet–Hamann–Schlüter pseudopotential.[1]

The sum in formula (1) is calculated at high-symmetry points in the Brillouin zone by solving the secular equation[5]

$$\left[\frac{1}{2}(\mathbf{k}+\mathbf{g}) - E_n(\mathbf{k}) \right] C_{n,\mathbf{k}}(\mathbf{g})$$

$$+ \sum_{\mathbf{g}'} W(\mathbf{k}+\mathbf{g}, \mathbf{k}-\mathbf{g}') C_{n,\mathbf{k}}(\mathbf{g}') = 0, \tag{9}$$

where $C_{n,\mathbf{k}}(\mathbf{g})$ are the coefficients in the expansion of the pseudowave function in terms of plane waves

$$\varphi_{n,\mathbf{k}}(\mathbf{r}) = \sum_{\mathbf{g}} C_{n,\mathbf{k}}(\mathbf{g})|\mathbf{k}+\mathbf{g}\rangle, \tag{10}$$

where n is the zone number and $\mathbf{k}$ is the wave vector in the first Brillouin zone. The Fourier transform of the potential

$$W(\mathbf{k}+\mathbf{g},\mathbf{k}+\mathbf{g}') = W_{\text{BHS}}(\mathbf{k}+\mathbf{g},\mathbf{k}+\mathbf{g}') + W_H(\mathbf{g}-\mathbf{g}')$$

$$+ W_{xc}(\mathbf{g}-\mathbf{g}') \tag{11}$$

contains not only the Hartree and exchange correlation Fourier transforms but also the Fourier transform of the Bachelet–Hamann–Schlüter pseudopotential. At the first step of the self-consistent iteration procedure the linearly screened local component of the pseudopotential is usually used:

$$W(\mathbf{g}) = W_{\text{loc}}(\mathbf{g})/\varepsilon(\mathbf{g}), \tag{12}$$

where $\varepsilon(\mathbf{g})$ is the permittivity function in the Lindhardt form. The matrix element of the local component of the Bachelet–Hamann–Schlüter pseudopotential is a superposition of the similar matrix elements for calcium and oxygen and is expressed in the form

$$W_{\text{loc}}(\mathbf{g}) = S(\mathbf{g})[W_{\text{loc,Ca}}(\mathbf{g}) + W_{\text{loc,O}}(\mathbf{g})\exp(i\mathbf{g}\mathbf{h})], \tag{13}$$

TABLE I. Equilibrium atomic volumes and total energies for calcium oxide for $B1$ and $B2$ structures (atomic volume in (a.u.)^3, energy in Ry).

	$B1$		$B2$	
	Ω	E	Ω	E
I	70.72	−17.497	89.54	−17.419
II	103.07	−17.101	95.66	−17.079
III	85.74	−17.065	89.87	−16.723
IV	92.24	−17.178	93.81	−16.558
V	91.30	−17.092	95.96	−16.646
VI	93.17	−17.055	94.03	−16.882

where $S(\mathbf{g})$ is the structure factor of the fcc and ccp lattices for $B1$ and $B2$ structures, respectively, $h = a_c(1/2, 1/2, 1/2)$, and a_c is the lattice constant.

The secular equation (9) is solved for the self-consistent calculations at each step. The construction of the crystal potential $W(\mathbf{g})$ at the next step of the iteration procedure takes into account the electron density distribution obtained at the previous step.[3] Integration over the first Brillouin zone was replaced by summation over a single Baldereschi point.[6]

The equilibrium atomic volumes and total energies were obtained from the equation of state of the crystal at $p = 0$ and $T = 0$:

$$\left(\frac{\partial E}{\partial \Omega} \right)_S = 0, \tag{14}$$

where S is the entropy. For the calculations we used expansions in terms of 59 vectors of the reciprocal lattice for the $B1$ structure and 57 for the $B2$ structure.

The results of the calculations are presented in Table I. Calculation I is done from first principles. The accuracy of the first-principle calculations can be enhanced by using a higher-order secular equation or more accurate methods of summation over the Brillouin zone (over Chadi–Cohen points[7]).

In calculation II the results of the first principle calculations are fitted using

$$\Delta E = b/\Omega, \tag{15}$$

where Ω is determined from the condition

$$E_{\Omega_{\text{exp}}} = E_{\text{exp}}. \tag{16}$$

Calculations III and IV were done using the Lindhardt dielectric function $\varepsilon(\mathbf{g})$. In the self-consistent calculations a ''new'' screening potential is calculated at each step, which corresponds to additive screening.[3,4] In calculation III the nonlocal component $l = 2$ of the Bachelet–Hamann–Schlüter pseudopotential is screened with respect to the imparted momentum by the function $\varepsilon(\mathbf{g})$. Similarly, the local component of the pseudopotential (12) is screened in calculation IV.

Calculations V and VI were also made under conditions where the local component of the pseudopotential is screened in the first step of the iteration procedure. In this case, the constants ε_1 and ε_2 were used as screening factors and the potential (13) had the form

$$W_{\text{loc}}(\mathbf{g}) = S(\mathbf{g})[W_{\text{loc,Ca}}(\mathbf{g})/\varepsilon_1 + W_{\text{loc,O}}(\mathbf{g})\exp(i\mathbf{g}\mathbf{h})/\varepsilon_2], \tag{17}$$

where ε_2 was taken as 0.95. For calculation V we have $\varepsilon_1 = 0.9$, and for calculation VI $\varepsilon_1 = 0.8$. The experimental values are $\Omega = 94.09$ (a.u.)^3 and $E = -17.07$ Ry.

[1] G. B. Bachelet, D. R. Hamann, and M. Schlüter, Phys. Rev. B **26**, 4199 (1982).

[2] A. A. Katsnel'son, V. S. Stepanyuk, O. F. Farberovich *et al.*, *Electronic Theory of Condensed Media* [in Russian], Moscow State University Press, Moscow (1990), 240 pp.

[3] G. L. Krasko, Z. Naturforsch. A **36**, 1129 (1981).

[4] L. I. Yastrebov and A. A. Katsnel'son, *Foundations of the One-Electron Theory of Solids* (AIP, New York, 1987; Nauka, Moscow, 1981, 320 pp.)

[5] P. J. H. Denteneer and W. van Haeringen, J. Phys. C **18**, 4127 (1985).

[6] A. Baldereschi, Phys. Rev. B **8**, 5212 (1973).

[7] D. J. Chadi and M. L. Cohen, Phys. Rev. B **8**, 5747 (1973).

Translated by R. M. Durham

Depth of penetration of microindenters in a metal target subjected to a fast powder flux

S. K. Andilevko, S. S. Karpenko, and V. A. Shilkin

Research Institute of Pulsed Processes, Belarus State Scientific-Industrial Concern of Powder Metallurgy, Minsk
(Submitted November 26, 1998)
Pis'ma Zh. Tekh. Fiz. **25**, 69–73 (April 12, 1999)

Results are presented of experiments to determine the maximum depths of superdeep penetration and to check the conclusions of an existing model of this effect. © *1999 American Institute of Physics.* [S1063-7850(99)01104-0]

The maximum depths of superdeep penetration of powders into targets[1–3] have attracted major interest among researchers since this effect was first observed experimentally. Using layer-by-layer chemical analysis, micro-x-ray spectral and x-ray structural analysis, neutron diffraction analysis, and various other indirect methods of studying solid materials, the authors of Refs. 1–3 showed that the superdeep penetration of microparticles (initial sizes of around 10 μm) from a powder flux may reach depths of several tens of millimeters. However, these studies of the maximum depths of penetration did not exhibit high accuracy and the experiments were not definitive. In order to improve the reliability of the results, we developed a special apparatus which can identify penetration to various predefined depths.

For this purpose we placed a detector in the path of a particle flux generated by an explosive accelerator (Fig. 1). This detector was a protective steel container in which samples were inserted (Fig. 2), which completely protects the inserted material from the influence of lateral movement. The depth of penetration is determined from the particles piercing the upper sample in the container. The penetrating material is collected inside the working chamber of the container by sets of foils each 0.00003 m thick (up to 30) interspersed with tracing paper which reliably decelerates the powder particles. A subsequent chemical analysis can not only reveal the penetration to depths determined by the upper sample but can also provide a quantitative assessment of the process without using expensive equipment.

By then increasing the height of the upper test sample (Fig. 2), the authors reliably observed an increased content of the penetrating powder (cobalt) in the foils to depths of around 70–75 mm (the initial size of the cobalt particles was less than 10 μm), which provides reliable confirmation that the particles have penetrated to this depth as a result of superdeep penetration.

By using the system shown in Fig. 2 to record the results of superdeep penetration, it was possible to make a direct experimental check of the conclusions reached by Adadurov et al.,[4] who suggested that superdeep penetration is determined by the consequences of axisymmetric annular impact when the aluminum facing of the powder container in the accelerator (Fig. 1), accelerated and twisted into a ring by the explosive energy, encounters the surface of the target. The authors[4] therefore assume that superdeep penetration should

be seen simply as a particular case of the stinging effect described by them (this term is taken from Ref. 4), which describes a mechanism for the formation of an extremely high-pressure zone on the axis of annular impact beneath the surface of the solid, which frequently leads to the formation of caverns into which, in the view of these authors, the particles penetrate.

Without going into a detailed polemic on the conclusions reached by Adadurov et al.,[4] we note that in the superdeep penetration experiment, this twisting of the charge facing occurs extremely rarely, whereas superdeep penetration is regularly recorded. Moreover, with this approach, weakening of the barrier should be expected regardless of the type of penetrating material. However, practical experiments and ten years of using this effect in practice have shown that the matrix can either be strengthened or weakened depending on the type of penetrating material. Moreover, Aleksentseva et al.[5] have reliably recorded superdeep penetration by using a system in which there is absolutely no possibility of the barrier interacting with anything but the powder flux. In this case, however, a direct response to the proposal put forward by Adadurov et al.[4] may be provided as a result of a direct experiment, which in any case is far more convincing than any polemic. This can be accomplished by removing the
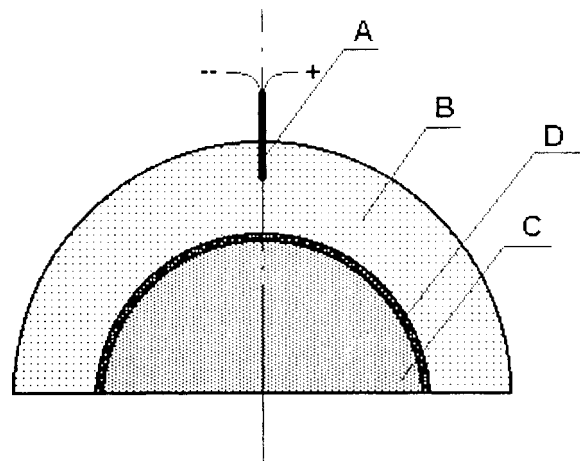
FIG. 1. Schematic of explosive accelerator for powder particles for superdeep penetration: *A*—detonator, *B*—explosive, *C*—powder container, and *D*—facing of powder container.
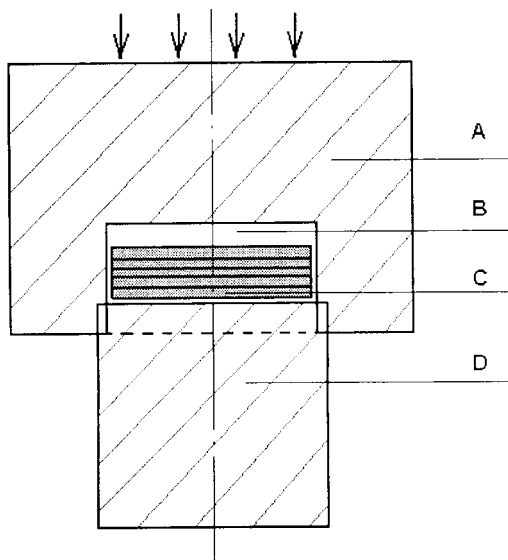
FIG. 2. Schematic of composite protective container: *A*—test sample, *B*—working chamber (cylindrical cavity), *C*—set of foils interspersed with tracing paper, *D*—lower blanking sample.

''culprit'' (in the opinion of the authors of Ref. 4), i.e., the aluminum facing of the powder container, from the accelerator system (Fig. 1).

This experiment was carried out using the composite protective container (Fig. 2) as the collecting device. The explosive accelerator shown in Fig. 1 had no facing in the powder container. Direct contact between the explosive and the powder causes some loss of acceleration energy because detonation products are ''blown'' straight through the porous layer of powder, so the height of the upper sample in the composite protective container was set at 50 mm in order to

obtain a more reliable determination of penetration. An analysis of the foils removed from the container chamber after treatment revealed a definite increase in the content of penetrating material (cobalt), which provides undisputable evidence that the powder has penetrated to a depth of at least 50 mm (for the cobalt powder used with particle sizes less than 10 μm the relative depth of penetration in this case exceeds 5000, which is undoubtedly of the order of magnitude of that recorded for superdeep penetration).

To conclude, these experiments have established that:

a) The maximum depth of superdeep penetration of cobalt powder with particle sizes less than 10 μm is at least 70 mm (i.e., the relative depth of penetration exceeds 7000);

b) Superdeep penetration is not the result of a stinging effect caused by the annular impact of the facing of the powder container accelerated by explosive products since, at variance with the view held by Adadurov *et al.*,[4] this effect is observed when a barrier is exposed to a particle flux accelerated by an accelerator containing no such structural element.

[1] L. V. Al'tshuler, S. K. Andilevko, G. S. Romanov, and S. M. Usherenko, Pis'ma Zh. Tekh. Fiz **15**(5), 55 (1989) [Sov. Tech. Phys. Lett. **15**, 186 (1989)].

[2] S. K. Andilevko, G. S. Romanov, V. A. Shilkin, and S. M. Usherenko, Int. J. Heat Mass Transf. **36**, 1113 (1993).

[3] M. Jeandin, M. Vardavoulias, S. K. Andilevko, O. V. Roman, V. A. Shilkin, and S. M. Usherenko, Rev. Metall. No. **12**, 808 (1992).

[4] N. A. Adadurov, A. F. Belikova, and S. N. Buravova, Fiz. Goreniya Vzryva **28**, 95 (1992).

[5] S. E. Aleksentseva, D. V. Isaev, and D. A. Krivchenko, in *Proceedings of the International Conference on Shock Waves in Condensed Matter*, St. Petersburg, 1996, p. 122.

Translated by R. M. Durham

Extension of a model analysis of the degree of polarization of light

Sh. D. Kakichashvili and A. L. Purtseladze

Institute of Cybernetics, Georgian Academy of Sciences, Tbilisi
(Submitted October 6, 1998)
Pis'ma Zh. Tekh. Fiz. **25**, 74–78 (April 12, 1999)

A theoretical approach is developed in which partially polarized radiation can be represented as a sum of coherent and incoherent components and also of the action of some imaginary device with time-dependent birefringence. This approach allows the Jones vector matrix method to be used for the calculations, which is important for theoretical calculations of the polarization state. © *1999 American Institute of Physics.* [S1063-7850(99)01204-5]

As we know, partially polarized radiation can be represented as a combination of two mutually completely incoherent components having the largest possible difference in intensity and opposite directions of rotation.[1] Using this concept, Kakichashvili[2] modified the Jones vector matrix method[3] by introducing the formal operation of incoherent summation of amplitudes and determined the rules of operation with the appropriate index. This approach generalized the Jones vector matrix method for the arbitrary partial polarization of electromagnetic waves, while completely conserving its formal scheme of usage. This modification was used previously in polarization holography in the particular case of an unpolarized reference wave and was confirmed theoretically and experimentally.[4,5]

In Ref. 6, Kakichashvili considered the formation of partially polarized radiation to be the result of the action of a time-dependent polarizing device on initially completely polarized light. In the present paper this approach is developed further and a theoretical analysis is made of the operation of a suitable device for the case of complex birefringence.

We shall represent the model device as a medium of thickness d having the complex birefringence $\Delta\hat{n}=\hat{n}_y-\hat{n}_x$ $\equiv\Delta n-i\Delta n\tau$, where $\hat{n}_y=n_y-in\tau_y$, $\hat{n}_x=n_x-in\tau_x$; n_y and n_x are the real refractive indices, and τ_y and τ_x are the extinction coefficients. For simplicity we shall also assume that the axes of birefringence and anisotropic absorption coincide and are oriented at the angle ρ relative to the laboratory coordinate system (see Fig. 1).

The corresponding Jones matrix of the model device is written as

$$M=\exp\frac{i\varkappa d}{2}(\hat{n}_x+\hat{n}_y)\begin{pmatrix}\hat{m}_{11} & \hat{m}_{12}\\ \hat{m}_{21} & \hat{m}_{22}\end{pmatrix},$$

$$\hat{m}_{11}=\cos\left(\frac{\varkappa d}{2}\Delta n\right)\left[\cosh\left(\frac{\varkappa d}{2}\Delta n\tau\right)\right.$$
$$\left.-\sinh\left(\frac{\varkappa d}{2}\Delta n\tau\right)\cos 2\rho\right]+i\sin\left(\frac{\varkappa d}{2}\Delta n\right)$$
$$\times\left[\sinh\left(\frac{\varkappa d}{2}\Delta n\tau\right)-\cosh\left(\frac{\varkappa d}{2}\Delta n\tau\right)\cos 2\rho\right],$$

$$\hat{m}_{12}=\hat{m}_{21}=-\left[\cos\left(\frac{\varkappa d}{2}\Delta n\right)\sinh\left(\frac{\varkappa d}{2}\Delta n\tau\right)\right.$$
$$\left.+i\sin\left(\frac{\varkappa d}{2}\Delta n\right)\cosh\left(\frac{\varkappa d}{2}\Delta n\tau\right)\right]\sin 2\rho,$$

$$\hat{m}_{22}=\cos\left(\frac{\varkappa d}{2}\Delta n\right)\left[\cosh\left(\frac{\varkappa d}{2}\Delta n\tau\right)\right.$$
$$\left.+\sinh\left(\frac{\varkappa d}{2}\Delta n\tau\right)\cos 2\rho\right]+i\sin\left(\frac{\varkappa d}{2}\Delta n\right)$$
$$\times\left[\sinh\left(\frac{\varkappa d}{2}\Delta n\tau\right)+\cosh\left(\frac{\varkappa d}{2}\Delta n\tau\right)\cos 2\rho\right]. \quad (1)$$

Let us assume that an elliptically polarized plane wave **E** propagating along the Z axis, with the major axis of the ellipse oriented along X, reaches the device described by expression (1). If $\Delta\hat{n}$ and ρ are fairly fast functions of time comparable with the optical frequency, the device is time-dependent and the field directly after the device may be represented as two components $\mathbf{E}_A$ and $\mathbf{E}_B$, connected by the incoherent summation sign $\oplus$ (see Ref. 6), and the field of the transmitted wave is given by

$$\mathbf{E}=M\mathbf{E}=\mathbf{E}_A\oplus\mathbf{E}_B, \quad (2)$$

$$\mathbf{E}=E_x\exp i(\omega t-\varkappa z)\begin{pmatrix}1\\ \pm i\xi\end{pmatrix}, \quad 0\leq\xi\equiv\frac{E_y}{E_x}\leq 1,$$

where

$$\mathbf{E}_A=E_x\exp i(\omega t-\varkappa z)\exp-\frac{i\varkappa d}{2}(\hat{n}_x(t)+\hat{n}_y(t))$$
$$\times\begin{pmatrix}\hat{m}_{11}(t)\\ \pm i\xi\hat{m}_{22}(t)\end{pmatrix},$$

$$\mathbf{E}_B=E_x\exp i(\omega t-\varkappa z)\exp-i\frac{\varkappa d}{2}(\hat{n}_x(t)+\hat{n}_y(t))\begin{pmatrix}\pm i\xi\\ 1\end{pmatrix}.$$

In its most general form, we show that this representation of the mutually incoherent components $\mathbf{E}_A$ and $\mathbf{E}_B$ is possible because there is no linear functional coupling between the matrix elements $\hat{m}_{11}(t)$, $\hat{m}_{22}(t)$, and $\hat{m}_{12,21}(t)$,
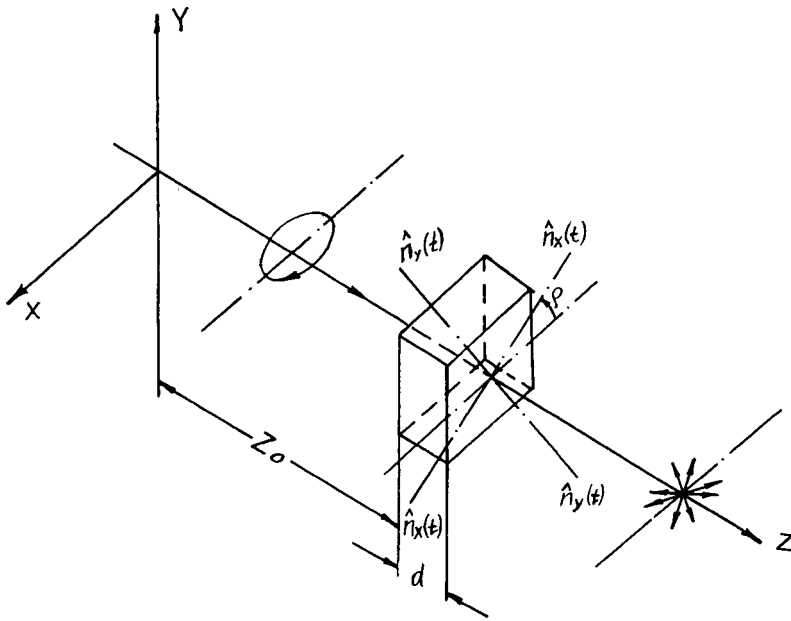
FIG. 1. Time-dependent model device.

unlike the identically equal elements $\hat{m}_{12}(t) = \hat{m}_{21}(t)$. Using for this purpose the generalized Wronskian for complex equations,[7] we have

$$W[\hat{m}_{11}(t), \hat{m}_{22}(t)] = \frac{\varkappa d}{2} \sin\left(\frac{\varkappa d}{2} \Delta \hat{n}(t)\right) \cos^2 2\rho(t) \frac{\partial \Delta \hat{n}(t)}{\partial t}$$

$$+ 2i\left[\frac{\varkappa d}{2} \cos^2\left(\frac{\varkappa d}{2} \Delta \hat{n}(t)\right)\right.$$

$$\times \cos 2\rho(t) \frac{\partial \Delta \hat{n}(t)}{\partial t} - \sin(\varkappa d \Delta \hat{n}(t))$$

$$\left. \times \sin 2\rho(t) \frac{\partial \rho(t)}{\partial t}\right] \neq 0,$$

$$W[\hat{m}_{11}(t), \hat{m}_{12}(t)] = -2\sin^2\left(\frac{\varkappa d}{2} \Delta \hat{n}(t)\right)[\sin^2 2\rho(t)$$

$$+ \cos 2\rho(t) \sin 2\rho(t)] \frac{\partial \rho(t)}{\partial t}$$

$$- i\frac{\varkappa d}{2} \sin 2\rho(t) \frac{\partial \Delta \hat{n}(t)}{\partial t} \neq 0. \qquad (3)$$

The set of equations (3) uniquely indicates that after passing through the device, the field can be expressed in the form (2), where $\mathbf{E}_A$ is the completely unpolarized component and $\mathbf{E}_B$ is the completely polarized component. In this situation, the degree of polarization may be given by[8]

$$V = \frac{I_B}{I_A + I_B}. \qquad (4)$$

Here we have

$$I_B = \mathbf{E}_B^+ \mathbf{E}_B, \quad I_A = \mathbf{E}_A^+ \mathbf{E}_A,$$

$$\mathbf{E}_B^+ \mathbf{E}_B = (1 + \xi^2) E_x^2 \hat{m}_{12}^*(t) \hat{m}_{12}(t),$$

$$\mathbf{E}_A^+ \mathbf{E}_A = E_x^2(\hat{m}_{11}^*(t) \hat{m}_{11}(t) + \xi^2 \hat{m}_{22}^*(t) \hat{m}_{22}(t)).$$

By calculating the intensities of the appropriate components, using Eq. (1) and substituting into expression (4), we obtain in its most general form an expression for the degree of polarization of the transmitted light for a time-dependent model device with complex birefringence:

$$V = \frac{(1 + \xi^2)\sin^2 2\rho(t)\left[\sinh^2\left(\frac{\varkappa d}{2} \Delta n \tau(t)\right) + \sin^2\left(\frac{\varkappa d}{2} \Delta n(t)\right)\right]}{(1 + \xi^2)\left[1 + 2\sinh^2\left(\frac{\varkappa d}{2} \Delta n \tau(t)\right)\right] - (1 - \xi^2)\sinh(\varkappa d \Delta n \tau(t))\cos 2\rho(t)}. \qquad (5)$$

Quite clearly, since the degree of polarization written in the form (5) is a function of time, at each i it has the meaning of some instantaneous quantity which is a function of the

time dependence $\Delta \hat{n}(t)$ and $\rho(t)$. Under these conditions we must generalize the definition of the degree of polarization to be a quantity independent of the time of observation.

We have

$$\langle V \rangle = \frac{1}{T} \int_0^T V \, dt. \tag{6}$$

This modification contains information on the degree of polarization of the transmitted field for an arbitrary time dependence of the model device.

[1] W. A. Shurcliff, *Polarized Light: Production and Use* (Harvard University Press, Cambridge, Mass. 1962; Moscow, 1965, 246 pp.)

[2] Sh. D. Kakichashvili, Zh. Tekh. Fiz **59**(2), 26 (1989) [Sov. Phys. Tech. Phys. **34**, 145 (1989)].

[3] R. C. Jones, J. Opt. Soc. Am. **31**, 491 (1941).

[4] Sh. D. Kakichashvili and A. L. Purtseladze, Pis'ma Zh. Tekh. Fiz **18**(22), 27 (1992) [Sov. Tech. Phys. Lett. **18**, 734 (1992)].

[5] Sh. D. Kakichashvili, Pis'ma Zh. Tekh. Fiz **19**(14), 5 (1993) [Tech. Phys. Lett. **19**, 434 (1993)].

[6] Sh. D. Kakichashvili, Zh. Tekh. Fiz **65**(7), 200 (1995) [Tech. Phys. **40**, 743 (1995)].

[7] G. A. Korn and T. M. Korn, *Mathematical Handbook for Scientists and Engineers* (McGraw-Hill, New York, 1961; Nauka Moscow, 1973, 831 pp.)

[8] M. Born and E. Wolf, *Principles of Optics*, 4th ed. (Pergamon Press, Oxford, 1969; Nauka, Moscow, 1970, 855 pp.)

Scale invariance and the Gell-Mann–Low function of the conductance of a layer with an exponentially broad resistance spectrum

A. A. Snarskiĭ, K. V. Slipchenko, and A. Dziedzic

Kiev Polytechnic Institute, Ukrainian National Technical University, Kiev, Ukraine ''Nauka-Servis,''
Moscow Wrocław Polytechnic Institute, Wrocław, Poland
(Submitted November 3, 1998)
Pis'ma Zh. Tekh. Fiz. **25**, 79–84 (April 12, 1999)

A study is made of a layer having an exponentially broad spectrum of local resistances, one of whose dimensions is smaller than the self-averaging dimension. An investigation is made of the hypothesis of scale invariance and the Gell-Mann–Low function for finite scaling in systems with an exponentially broad spread of resistances. A comparative analysis is made of the scale behavior of these systems and the case of strong localization. © *1999 American Institute of Physics.* [S1063-7850(99)01304-X]

In many cases where the electrophysical properties of materials are being studied, these can be modeled using a medium having an exponentially broad spectrum of local resistances. Examples may include doped semiconductors (the so-called Miller and Abrahams mesh), conducting adhesives, various thick-film resistors, and so on.[1,2] The problem of the effective conductivity of these systems is solved using a percolation-type approach[1] which can be used to obtain the effective conductivity on the basis of information on a two-phase medium near the percolation threshold. As a result of the strong nonequilibrium, these systems have large correlation lengths ξ, i.e., the dimension used for self-averaging of the physical properties. Thus, the case when some of the linear dimensions of a sample are smaller than the value of ξ for the three-dimensional problem is of considerable practical interest. For example, the conductance of a layer with $L < \xi$ depends strongly (exponentially) on its thickness L.

Here we find the transverse conductance of a layer having the dimensions $\mathcal{L} \times \mathcal{L} \times L$, where $\mathcal{L} \gg \xi$ and $L < \xi$, in which the local resistance spectrum has an exponentially broad spread.

Let us assume that the local conductivity is $\sigma = \sigma_0 \exp(\lambda x)$, where $\lambda \gg 1$ is a quantity characterizing the width of the σ spread and $0 < x < 1$ is a random variable with a uniform distribution function. The correlation length of the three-dimensional system is $\xi = a_0 \lambda^\nu$ (Refs. 1 and 3), where a_0 is the minimum dimension in the system, for a mesh this is the coupling length, and ν is the critical index for the correlation length of a two-phase percolation medium.

We shall arbitrarily divide the layer into $L \times L \times L$ cubes and we shall replace these with effectively homogeneous cubes having conductances equal to those of the various realizations. The expression for the transverse and longitudinal conductivity of the layer obtained using this approach for a two-phase system shows good agreement with the well-known results.[4–6] According to Shklovskii and Efros,[1] the conductance of an isolated realization is

$$G_r \approx g_0 e^{\lambda x_c}, \quad g_0 = a_0 \sigma_0, \quad x_c = 1 - p_c, \tag{1}$$

where p_c is a random quantity which defines the percolation threshold of this realization. Thus, G_r is also a random quantity. The distribution for p_c is close to a Gaussian centered at $\langle p_c \rangle = p_{c3} + A(L/a_0)^{-1/\nu}$ with variance $S = B(L/a_0)^{-1/\nu}$, where A and B are various constants and $B > A$ (Ref. 1). In the assumed approximation the transverse conductance of this layer $G_\perp$ is the sum of the conductances of the $L \times L \times L$ cubes. Hence, $G_\perp$ may be expressed in terms of the average over the realizations

$$G_\perp = N\{G_r\},$$

$$\{G_r\} = g_0 e^{x_{c3}\lambda - A\lambda(L/a_0)^{-1/\nu} + B^2\lambda^2(L/a_0)^{-2/\nu}}, \tag{2}$$

where N is the number of cubes into which the layer is divided and the braces indicate the average over the realizations. For the averaging we use a Gaussian distribution for x_c with the variance S and the mean $\langle x_c \rangle$. Equation (2) gives the specific conductance over area

$$\frac{G_\perp}{\mathcal{L}^2} = \frac{g_0}{L^2} e^{x_{c3}\lambda - A\lambda(L/a_0)^{-1/\nu} + B^2\lambda^2(L/a_0)^{-2/\nu}}. \tag{3}$$

This expression holds when the longitudinal dimension of the layer $\mathcal{L}$ is sufficient for self-averaging, i.e., for $\mathcal{L} \gg \xi_\perp$, where $\xi_\perp$ is the correlation length of the layer. In order to determine $\xi_\perp$ we find the fluctuation of the conductance $G_\perp$, which is the sum of the conductances of the effective cubes forming the layer $G_\perp = \Sigma G_r$.

Since $G_\perp$ is a sum of independent random quantities, in this approximation the relative fluctuation is $\delta_{G_\perp} = \delta_{G_r}/N$ and

$$\delta_{G_\perp} = \frac{\{G^2\} - \{G\}^2}{\{G\}^2 N} = \frac{L^2}{\mathcal{L}^2}[e^{B^2\lambda^2(L/a_0)^{-2/\nu}} - 1]. \tag{4}$$

In the limit $L \ll \xi_\perp$ the one inside the brackets can be neglected and the correlation length becomes

$$\xi_\perp \approx L\, e^{B^2\lambda^2(L/a_0)^{-2/\nu}}. \tag{5}$$

In fact the condition $\mathcal{L} \gg \xi_\perp$ yields $\delta_{G_\perp} \ll 1$. However, when $L \approx \xi$ holds, Eq. (4) gives $\xi_\perp \approx L \approx \xi$.
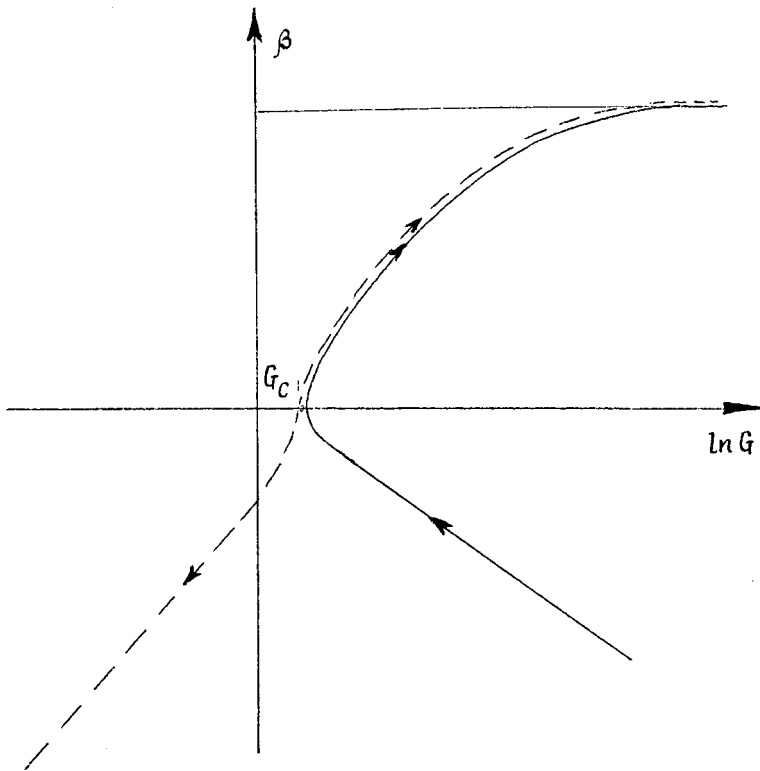
FIG. 1. Dashed curve—Gell-Mann–Low function $\beta(G)$ for strong localization; solid curve—the same function for a medium with an exponentially broad spectrum of resistance distribution. The direction of the arrows indicates the direction of increasing sample dimension L.

It follows from Eq. (2) that the conductance $\{G_r\}$ averaged over the realizations can be expressed simply in terms of the specific conductance of the layer over area $G_\perp$, and specifically $\{G_r\} = (L/\mathcal{L})^2 G_\perp$. Thus, measurements of the layer conductance can directly yield the conductance of cubes having dimensions L shorter than the correlation length, averaged over realizations.

We shall analyze the dependence of $\{G_r\}$ on L in greater detail. A well-known similar problem[1,7] involves determining the dependence of the conductance on the dimensions of a system with strong localization. According to the hypothesis of scale invariance,[1,7] the conductance is the only quantity that determines the behavior of a system as its dimensions vary. This statement may be written by introducing the Gell-Mann–Low function $\beta(G)$:

$$\beta(G) = \partial \ln G / \partial \ln L; \tag{6}$$

The dashed curve in Fig. 1 gives its dependence on $\ln G$ for the strong localization problem.

Le Doussal[3] formulated a similarity hypothesis for $\{G_r\}$ (finite scaling) which may be written as follows in the terminology adopted above:

$$\{G_r\} = G_c F(L^{1/\nu}\lambda^{-1}), \quad G_c = g_0 e^{\lambda x_c}, \tag{7}$$

where the scaling function has the following asymptotic forms: $F(z \ll 1) \to 1$ and $F(z \gg 1) \to z^\nu$ and we confined our analysis to the three-dimensional case. In accordance with this asymptotic form we have $\{G_r(L^{1/\nu}\lambda^{-1} < 1)\} \sim G_c$ and $\{G_r(L^{1/\nu}\lambda^{-1} \gg 1)\} \sim G_c L \lambda^{-\nu}$. It follows from Eq. (3) that $\{G_r\}$ obtained here satisfies these asymptotic forms. Moreover, the explicit expression allowed us to calculate the function $\beta(\{G\})$ given by the solid curve in Fig. 1. It can be seen

from the figure that the Gell-Mann–Low function for this problem differs fundamentally from that for strong localization. Whereas for strong localization the value of G_c separates two fundamentally different dependences of the conductance on L (above G_c the conductance G increases with increasing dimension whereas below G_c it decreases), in our case $\beta(\{G\})$ increases with increasing dimensions both above and below G_c.

Note that we can also apply the above reasoning to determine the longitudinal conductivity of this layer $\sigma_\parallel^e$. After replacing the realizations with homogeneous cubes, we convert to a two-dimensional system which satisfies the conditions for obtaining an exact solution.[8] Let us assume that the local conductivity of the two-dimensional system $\sigma(\mathbf{r})$ has a random distribution. We introduce the variable $\chi(\mathbf{r}) = \ln \sigma(\mathbf{r}) - \langle \ln \sigma(\mathbf{r}) \rangle$, where the angular brackets denote averaging. According to Dykhne,[8] if the density distribution function χ is even, the effective conductivity problem has an exact solution $\sigma_e = \exp(\langle \ln \sigma \rangle)$. Using this relation, we derive the well-known Shklovskii–Efros expression[1]

$$\sigma_\parallel^e = \sigma_0 e^{x_c \lambda - A\lambda(L/a_0)^{-1/\nu}}. \tag{8}$$

The self-averaging dimension $\xi_\parallel$ for $G_\parallel$ differs from $\xi_\perp$. We can consider this two-dimensional system to be a system with an exponentially broad local resistance spectrum. Then its correlation length is determined by the characteristic spectral width[3] λ^*: $\xi_\parallel = L(\lambda^*)^{\nu_2}$, where ν_2 is the two-dimensional percolation index of the correlation length and L is the minimum dimension in a system of homogeneous

$L \times L \times L$ cubes. In our case, we have $\lambda^* = \lambda B (L/a_0)^{-1/\nu}$, and then

$$\xi_{\parallel} = L(B\lambda)^{\nu_2} \left(\frac{L}{a_0} \right)^{-\nu_2/\nu} = a_0 (B\lambda)^{\nu_2} \left(\frac{L}{a_0} \right)^{1 - \nu_2/\nu}. \qquad (9)$$

Unlike $\xi_{\perp}$, $\xi_{\parallel}$ depends fairly weakly on the layer thickness $1 - \nu_2/\nu \approx 0.2$.

[1] B. I. Shklovskii and A. L. Efros, *Electronic Properties of Doped Semiconductors* (Springer-Verlag, Berlin, 1984).
[2] A. Dziedzic, Microelectron. Reliab. **31**, 537 (1991).
[3] P. Le Doussal, Phys. Rev. B **39**, 881 (1989).
[4] J. P. Clerc, G. Giraud, S. Alexander, and E. Guyon, Phys. Rev. B **22**, 2489 (1980).
[5] P. Gadenne and M. Gadenne, Physica A **157**, 344 (1989).
[6] V. Neimark, Zh. Éksp. Teor. Fiz. **98**, 611 (1990) [Sov. Phys. JETP **71**, 341 (1990)].
[7] A. A. Abrikosov, *Fundamentals of the Theory of Metals* (North-Holland, Amsterdam, 1988; Nauka, Moscow, 1987), p. 520.
[8] A. M. Dykhne, Zh. Éksp. Teor. Fiz. **59**, 110 (1970) [Sov. Phys. JETP **32**, 63 (1970)].

Translated by R. M. Durham

Losses in diamond in the millimeter range

B. M. Garin, V. V. Parshin, V. G. Ral'chenko, V. I. Konov, A. N. Kopnin, A. B. Mazur, M. P. Parkhomenko, and E. E. Chigryaĭ

Institute of Radio Engineering and Electronics, Russian Academy of Sciences, Fryazino, Moscow Province; Institute of Applied Physics, Russian Academy of Sciences, Nizhniĭ Novgorod Center for Natural Scientific Research, Institute of General Physics, Russian Academy of Sciences, Moscow
(Submitted May 19, 1998)
Pis'ma Zh. Tekh. Fiz. **25**, 85–89 (April 12, 1999)

A theoretical and experimental investigation is made of the magnitude and nature of the dielectric losses in weakly absorbing synthetic diamonds in the wavelength range 1.75–6.8 mm at temperatures $T = 20–500\,°C$. Some samples exhibited extremely low losses ($\tan\delta < 10^{-5}$) which makes plasma-chemically deposited diamond wafers suitable for fabricating windows for megawatt continuous gyrotrons. It is shown that in principle, a further substantial reduction in losses can be achieved. © *1999 American Institute of Physics.* [S1063-7850(99)01404-4]

Progress achieved in the technology used to synthesize polycrystalline diamond films by deposition from the gas phase and the development of large-diameter (5–10 cm) diamond wafers of thickness up to 1–2 mm has opened up possibilities for measuring low dielectric losses in diamonds in the millimeter wavelength range and also for fabricating diamond windows for powerful sources of millimeter radiation, i.e., gyrotrons. Galdetskiĭ and Garin[1] and Garin[2] predicted theoretically that in crystals with a diamond lattice structure, extremely low intrinsic lattice losses may occur in the millimeter and submillimeter ranges, corresponding to those of an ideal crystal and defining the theoretical limit to which losses can be reduced. Moreover, of these crystals, diamond has the lowest theoretical limits for reducing the lattice losses and the losses caused by free carriers.[2,3]

Results of measurements of the losses in synthetic diamonds are available in the millimeter range[4–6] and also at lower frequencies.[7] However, the temperature–frequency dependence has been very little studied, the nature of these losses has not been identified, and the influence of the diamond synthesis conditions on the losses and the possibility of reducing these substantially have not been considered. These aspects are examined in the present paper.

Garin[2] and Garin *et al.*[3] obtained rough theoretical estimates of the absolute values of the intrinsic lattice losses in diamond, silicon, and germanium: $\tan\delta \sim 10^{-9}$, 3×10^{-8}, and 2×10^{-7}, respectively, at $\lambda = 2$ mm and room temperature. From a comparison with experimental data on the lowest losses recorded in gold-compensated silicon[3,8] (Si:Au) we can deduce that under these conditions the value of $\tan\delta$ for the intrinsic lattice losses in diamond should at any rate be $\leq 3 \times 10^{-8}$.

We investigated series of polycrystalline diamond wafers grown at the Institute of General Physics by plasma-chemical deposition from $CH_4–H_2–O_2$ mixtures in a microwave discharge.[9] The growth rate was 2–5 μm/h and the concentration of nitrogen impurities was in the range $(2–30) \times 10^{17}\,cm^{-3}$. The samples separated from the substrates were 55–60 mm diameter disks up to 1.3 mm thick. The measurements were made in open resonators at the Institute of Radio Engineering and Electronics[3] and at the Institute of Applied Physics.[10] The temperature dependence of the losses and the refractive index was also measured over the range $T = 20–500\,°C$. The results for a series of unpolished disks measured at the Institute of Radio Engineering and Electronics are given in Tables I and II.

The losses lie in the range $\tan\delta = (1–10) \times 10^{-4}$ and they tend to decrease as the growth rate and nitrogen impurity content decrease. After annealing in air at $T = 550\,°C$ sample No. 111 showed a significant reduction in $\tan\delta$ from $\approx 1.5 \times 10^{-4}$ to $\approx 5 \times 10^{-5}$.

The lowest losses were observed for sample No. 113 (growth rate 2.4 μm/h, nitrogen concentration $2 \times 10^{17}\,cm^{-3}$) in measurements made at the Institute of Applied Physics (see Fig. 1). In order to improve the measurement accuracy because of the low losses, the disk was polished on both sides with a deviation from plane-parallel of less than 0.005 mm over its 55 mm diameter. The thickness was reduced from 1.05 to 0.74 mm, for which the 170 GHz measurement frequency was in resonance (this thickness is a multiple of half the wavelength in the material). After mechanical treatment the disk was annealed in air. The method of measurement[10] was modified slightly so that the error in these measurements of $\tan\delta$ was $\pm 10^{-6}$. The losses in this sample, $\tan\delta \sim 8 \times 10^{-6}$ (170 GHz; $20\,°C$), are among the lowest reported in the literature for diamond[6] and are close to the lowest losses ($\tan\delta \sim 3 \times 10^{-6}$) recorded for Si:Au (Ref. 8).

Calculations of the transmittivity show that the best of these diamonds can be used to fabricate windows for ≥ 3 MW cw gyrotrons.

The dependence of the losses on the frequency f in this range (Table II) follow a $1/f$ law to a first approximation. The observed frequency–temperature dependence may be attributed to conduction losses in nondiamond phases having a highly nonuniform distribution of local dynamic electrical

TABLE I. Losses $\tan \delta$ at $\lambda = 2.15$ mm at room temperature in diamond films.

Sample No.	Average thickness, μm	Growth rate, μm/h	$\tan \delta$, 10^{-4}
92	1280	5.0	8
83	190	4.6	10
79	490	4.5	1.5–3
70	230	3.9	<5
111	490	3.7	1–2
93	430	3.2	2
56	270	2.7	2
100	640	2.6	1.5–3.5
AST	180	2.5	<2

conductivity σ, which contain amorphous carbon and nanographite. Data obtained by Raman spectroscopy indicate that the relative volume fraction of these phases is less than 10^{-3}. Moreover, the losses increase with decreasing frequency slower than $1/f$ for $f \lesssim 10$ GHz (Ref. 7) because fewer regions satisfy the condition $\tau_M^{-1} \ll \omega$, where $\tau_M = \varepsilon \varepsilon_0 / \sigma$ and ε are the local values of the Maxwellian electrical relaxation time and the permittivity, respectively, ε_0 is the dielectric constant, and $\omega = 2\pi f$. The relatively weak temperature dependence of the losses (for $T < 400\,°$C) can be readily attributed to the weak dependence of the electrical conductivity in nondiamond inclusions. The increase in the losses observed for $T > 400\,°$C may be caused by a dipole relaxation process in the nondiamond phase.

The temperature and frequency dependence of the observed losses differs from the behavior of the intrinsic lattice losses (which should increase appreciably with increasing frequency and temperature[1–3]) and are considerably higher than their estimated values. Thus, the intrinsic lattice losses in diamond (as in silicon[3,8]) remain experimentally unidentified.

These data and the reasoning put forward above, together with estimates of the intrinsic losses indicate that there is scope for achieving a further substantial reduction of the losses in diamond and for obtaining the lowest losses in the millimeter and neighboring ranges compared with other materials.

TABLE II. Losses at wavelengths $\lambda = 2-7$ mm in sample No. 79.

λ, mm	2.15	3.9	6.0	6.8
$\tan \delta$, 10^{-4}	1.5–3	4	5	9.5
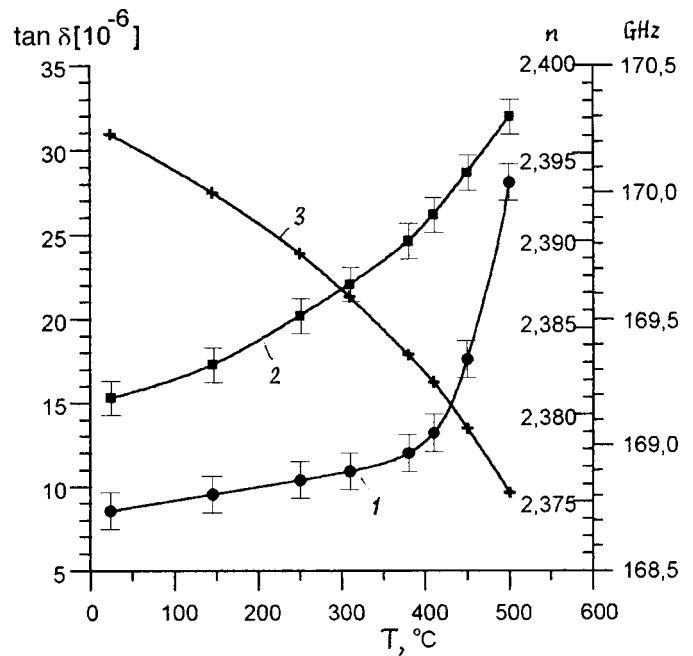
FIG. 1. Temperature dependence of $\tan \delta$ (*1*), the refractive index *n* (*2*), and the resonant frequency (*3*) in a diamond disk 0.74 mm thick.

[1] A. V. Galdetskiĭ and B. M. Garin, Preprint No. 17 (320) [in Russian], Institute of Radio Engineering and Electronics, Academy of Sciences of the USSR, Moscow (1981), 31 pp.

[2] B. M. Garin, in *Abstracts of Russian Scientific and Technical Conference "Dielectrics-93"*, St. Petersburg, 1993, Vol. 1 [in Russian], pp. 98–99.

[3] B. M. Garin, A. N. Kopnin, M. P. Parkhomenko *et al.*, Pis'ma Zh. Tekh. Fiz. **20**(21), 56 (1994) [Tech. Phys. Lett. **20**, 835 (1994)]; B. M. Garin, A. N. Kopnin, M. P. Parkhomenko *et al.*, in *Proceedings of the 21st International Conference on Infrared and Millimeter Waves*, Berlin, 1996, paper CT15.

[4] R. Heidinger, in *Digest of the 19th International Conference on Infrared and Millimeter Waves*, Japan, 1994, pp. 277–278.

[5] R. S. Sussmann, J. R. Brandon, G. A. Scarbrook *et al.*, Diamond Relat. Mater. **3**, 303 (1994).

[6] V. V. Parshin and V. A. Khmara, *Proceedings of the Ninth Joint Russian-German Meeting on ECRH and Gyrotrons*, 1997, pp. 143–144; R. Sporl, R. Schwab, and R. Heidinger, *ibid.*, pp. 167–174.

[7] A. Ibarra, M. Gonzalez, R. Vila *et al.*, Diamond Relat. Mater. **6**, 856 (1997).

[8] R. Heidinger, J. Molla, and V. V. Parshin, *Proceedings of the 21st International Conference on Infrared and Millimeter Waves*, Berlin, 1996.

[9] V. G. Ralchenko, A. A. Smolin, V. I. Konov *et al.*, Diamond Relat. Mater. **6**, 417 (1997).

[10] Yu. A. Dryagin and V. V. Parshin, in *Proceedings of the International Conference on Infrared and Millimeter Waves*, 1992, Vol. 13, pp. 1023–1032.

Translated by R. M. Durham

Continuous optical discharge in a thermionic converter for conversion of laser radiation energy into electrical energy

I. V. Alekseeva, A. P. Budnik, V. A. Zherebtsov, A. V. Zrodnikov, and S. T. Surzhikov

A. I. Leĭpunskiĭ Institute of Physics and Power Engineering, State Science Center, Obninsk, Russia
(Submitted October 3, 1998)
Pis'ma Zh. Tekh. Fiz. **25**, 90–95 (April 12, 1999)

A model is developed and calculations are made of the characteristics of a continuous optical discharge in the interelectrode gap of a thermionic converter for conversion of laser radiation energy into electrical energy. © *1999 American Institute of Physics.*
[S1063-7850(99)01504-9]

1. The idea of thermionic conversion of laser radiation energy into electrical energy was proposed by Rasor[1] in 1973 and was later confirmed experimentally at the end of the eighties.[2] Rasor's idea was based on an even earlier study.[3] Until now, however, no adequate theory has been put forward for this method of energy conversion and no effective methods have been developed for the mathematical modeling of a continuous optical discharge in the interelectrode gap. The aim of the present paper is to develop a model and mathematically simulate a steady-state continuous optical discharge in a thermionic converter.

The thermionic converter may be considered to be a gas-filled diode with a hot emitter and a cooler collector, with a continuous optical discharge burning in the interelectrode gap.[2] A characteristic feature of the discharge is that electric current flows through it and the electrodes are close to the high-temperature region of the discharge. A major factor in the discharge energy balance in the interelectrode gap is the transfer of energy to the electrodes by the highly nonequilibrium plasma radiation and by the charged and neutral plasma components.

2. An analysis of the experimental data[2] shows that in most of the interelectrode gap the plasma in a thermionic converter is almost in equilibrium (we shall call this region the discharge core). Deviations from equilibrium only occur in the thin layers near the electrodes, and the thickness of the electrode layer in which the temperature of the heavy plasma components T_i is lower than the electron temperature T_e is considerably greater than the thickness of the layer in which the charged particle concentration is below the equilibrium value. Generalizing the approach developed by Moĭzhes and Baksht[4] and Baksht *et al.*[5] for a thermionic converter of thermal into electrical energy to the case of a continuous optical discharge bounded by electrodes, we can appreciably simplify the description of the discharge by isolating three layers in the electrode regions, namely, the space charge, nonequilibrium, and quasiequilibrium plasma layers. By analyzing the processes in these three regions, we can determine the boundary conditions for the equilibrium plasma of the discharge core.

In accordance with the basic idea of the present study, we shall give a detailed description of the processes in the core region of the discharge and we shall allow for the processes in the electrode regions by means of boundary conditions. Using the well-developed methods from the theory of a continuous optical discharge[6,7] and the thermionic method of converting thermal energy into electrical,[8] we can obtain a closed system of equations and boundary conditions to describe the steady-state core of a continuous optical discharge in a thermionic converter. This system includes equations which describe the propagation and absorption of laser radiation in the quasioptic approximation, transport of the plasma self-radiation in the multilevel approximation, and equations describing the energy balance in the plasma, and the distribution of the electric potential and the current density in the discharge plasma (for further details see Ref. 9).

3. If the plasma at the boundary is weakly ionized, the boundary condition to determine the plasma temperature at the emitter boundary of the equilibrium region has the form

$$-(\lambda_t)_{T1}\left(\frac{dT}{dr}\right)\bigg|_{T1} = -2(T_{T1}-T_E)J_E$$

$$-(\lambda_H)_{T1}\frac{\sqrt{2}T_{T1}}{L_{T1}}\bigg[\ln\frac{T_{T1}}{N_E}$$

$$-\left(1-\frac{T_E}{T_{T1}}\right)\bigg]^{1/2}+\bigg(E_i+2T_{T1}$$

$$+e\Delta\varphi_{T1}-T_{T1}\ln\frac{n_{T1}}{n_{i1}}\bigg)(j_i)_1$$

$$-J_{T1}\bigg[\left(\frac{1}{2}+k_{eT1}^{(T)}\right)T_{T1}-e\Delta\varphi_{T1}\bigg]. \quad (1)$$

The subscript "$T1$" denotes values at the boundary. Condition (1) describes the plasma energy balance at the boundary. Its left-hand side gives the thermal energy flux from the discharge core. This energy is dissipated in heating the electrons emitted by the emitter to the plasma temperature T_{T1} (first term on right-hand side), goes to the emitter via the thermal conductivity of the heavy plasma components (ions and atoms), is dissipated in generating ions passing to the emitter in the nonequilibrium electrode layer, and passes to the boundary by the electron current (last term). Here T_E is the emitter temperature, λ_t is the thermal conductivity of the
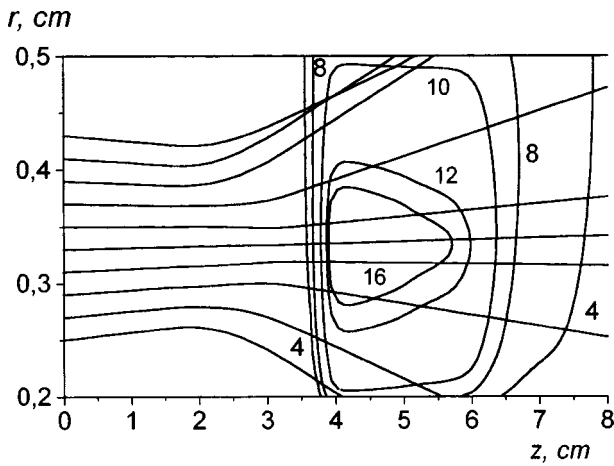
FIG. 1. Isotherms and beam path through the continuous optical discharge plasma for an idling diode with $r_1 = 0.2$ cm and $r_2 = 0.5$ cm, laser radiation power—90 kW, $J_E = 500$ A/cm^2, $P = 1$ atm, and $F = 15$ cm. The numbers near the isotherms are the temperature (in kK).
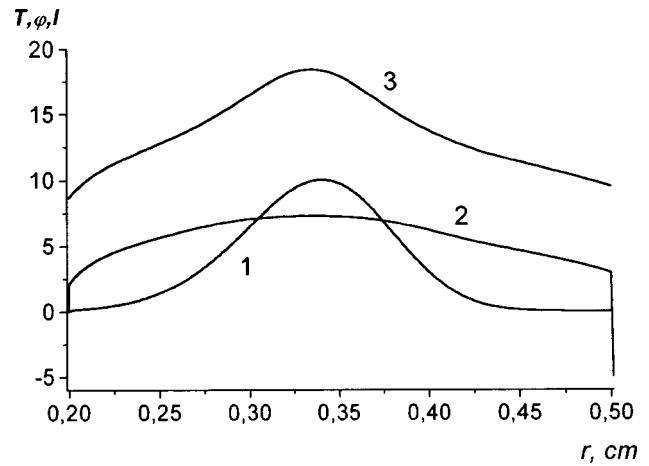
FIG. 2. Radial distribution of the laser radiation intensity (**I**) (curve 1) at $z = 0$ in arbitrary units, and also of the electric field potential (φ) (curve 2) in volts, and the plasma temperature (**T**) (curve 3) in kilodegrees Kelvin for the same converter parameters as in Fig. 1.

plasma, J_E is the flux density of the electrons emitted by the emitter, λ_H is the total thermal conductivity of the heavy plasma components, L_{T1} is the thermal relaxation length at the emitter, E_i is the atomic ionization potential, e is the electron charge, $\Delta\varphi_{T1}$ is the jump in potential between the equilibrium plasma and the emitter, n is the electron (ion) density, n_{i1} is the quasiequilibrium electron (ion) density at the emitter (when $T_e = T_{T1}$, but $T_i = T_E$), $(j_i)_1 = -(D_{a1} n_{i1})/(\sqrt{2} L_{i1})$ is the density of the ion flux to the emitter, D_{a1} is the coefficient of ambipolar diffusion at the emitter, L_{i1} is the ionization relaxation length near the emitter, J is the electron flux density, and $k_e^{(T)}$ is the electron thermal diffusion ratio. The boundary condition to determine the temperature at the collector boundary of the equilibrium region is similar. The other boundary conditions are formulated in the usual way and are omitted here for lack of space. Note that we pay particular attention to the electrode regions here because of their decisive role in the energy conversion process.[3]

4. The system of equations for the discharge core was solved by iteration.[10] Prior to solving the problem, we compiled a database of transport coefficients, and of thermophysical and optical properties of an argon plasma under the conditions obtaining in a thermionic converter. The calculations were made for an argon-filled converter at electrode temperatures $\sim 10^3$ K, argon pressure $P \sim 1$ atm, and J_E up to $\sim 10^3$ A/cm^2. A cylindrical 5.3 μm laser beam, directed along the z axis, was focused into a ring at a distance F from the entrance to the thermionic converter ($z = 0$) at the center of the gap between the emitter and the collector which comprised two coaxial cylinders of radii r_1 and r_2, respectively. This geometry is selected first to simplify the mathematical description by using axial symmetry and second, having in mind that efficient operation of the converter requires the emitter area to be considerably larger than the collector area. We assumed that the laser radiation is completely reflected by the electrodes and the plasma radiation is completely absorbed by them.

Typical results are plotted in Figs. 1 and 2. The longitu-

dinal dimension of the high-temperature discharge region along the z axis is approximately 2 cm and is appreciably greater than the distance between the electrodes (0.3 cm). The plasma temperature at the center of the gap is approximately 18 kK and drops to 9 kK at the boundaries of the discharge core and the nonequilibrium electrode regions. Refraction of the laser radiation strongly influences the formation of the discharge structure (Fig. 1). A large temperature gradient at the thin ($\sim 10^{-3} - 10^{-2}$ cm) electrode regions gives rise to large ($\sim 10^3$ W/cm^2) heat fluxes transferred by the heavy plasma components from the discharge core to the electrodes. The high plasma temperature at the electrodes is also responsible for large amounts of energy being dissipated in generating ions in the nonequilibrium regions. Nevertheless, under these conditions the main losses of energy from the discharge are attributed to the plasma intrinsic radiation (up to 10^4 W/cm^2).

The plasma in the central part of the discharge core is almost completely ionized whereas in the electrode regions the degree of ionization of the plasma is low (<0.1). The distribution of the electric field potential in the interelectrode gap has a characteristic structure with a large jump near the collector (~ 10 V) and a relatively small drop at the discharge core plasma (~ 1 V). The calculations showed that as the current through the diode increases, the plasma temperature at the emitter increases because the electrons are heated at the emitter potential drop whereas at the collector the plasma temperature decreases. However, these changes in temperature are small because of the strong (exponential) temperature dependence of the energy transferred to the electrodes by the heavy plasma components and also of the energy expended in generating ions in the nonequilibrium electrode regions.

To conclude, we have proposed for the first time an effective approach to the theoretical analysis of the thermionic conversion of laser radiation energy into electrical energy. We have also developed a mathematical model of a continuous optical discharge and calculated the distributions of the

plasma parameters in the interelectrode gap and the energy fluxes to the electrodes.

[1] N. S. Rasor, in *Proceedings of the Laser-Energy Conversion Symposium*, NASA TM X-62, NASA Ames Research Center, 1973, pp. 51–62.

[2] N. P. Kozlov, A. V. Pekshev, Yu. S. Protasov, and V. I. Suslov, *Radiative Plasma Dynamics* Vol. 1 [in Russian], Énergoatomizdat, Moscow (1991), pp. 462–498.

[3] J. F. Waymouth, IEE J. **8**, 380 (1962).

[4] B. Ya. Moĭzhes and F. G. Baksht, Zh. Tekh. Fiz **38**, 709 (1968) [Sov. Phys. Tech. Phys. **13**, 530 (1968)].

[5] F. G. Baksht, I. L. Korobova, and B. Ya. Moĭzhes, Zh. Tekh. Fiz **41**, 387 (1971) [Sov. Phys. Tech. Phys. **16**, 292 (1971)].

[6] S. T. Surzhikov, *Computational Experiment in the Construction of Radiative Models for the Mechanics of an Emitting Gas* [in Russian], Nauka, Moscow (1992).

[7] A. P. Budnik, A. S. Vakulovskiĭ, A. G. Popov, and S. T. Surzhikov, Mat. Model. **8(5)**, 1 (1996).

[8] F. G. Baksht, G. A. Dyuzhev, A. M. Martsinovskiĭ, B. Ya. Moĭzhes, G. E. Pikus, É. B. Sonin, and V. G. Yur'ev, *Thermionic Converters and Low-Temperature Plasma* (US DoE, Springfield, Va, 1978; Nauka, Moscow, 1973, 480 pp.)

[9] A. P. Budnik, P. P. D'yachenko, V. A. Zherebtsov, and A. V. Zrodnikova, Preprint No. 2653 [in Russian], Institute of Physics and Power Engineering, Obninsk (1997), 33 pp.

[10] I. V. Alekseeva, A. P. Budnik, V. A. Zherebtsov, and S. T. Surzhikov, Preprint No. 2679 [in Russian], Institute of Physics and Power Engineering, Obninsk (1998), 23 pp.

Translated by R. M. Durham

Efficient lasing of a mixture of organic dyes at 610 and 670 nm

A. Yu. Ivanov

Institute of Analytical Instrumentation, St. Petersburg
(Submitted October 12, 1998)
Pis'ma Zh. Tekh. Fiz. **25**, 1–7 (April 26, 1999)

The efficiency of the lasing regime of a pulsed tunable laser at the ''exotic'' wavelengths of 610 and 670 nm, which are needed in nuclear physics, is investigated. A method for performing model calculations of the active media for such a laser, i.e., working mixtures of high-molecular-weight dyes, is developed. The conditions specifying a quasiequilibrium window, in which the achievement of high output characteristics is possible for such a mixture at assigned wavelengths, are derived. It is interpreted on the basis of the law of alternating nonequilibria in the theory of nonequilibrium states. The results obtained are verified experimentally: a high-power miniature pulsed laser with an active medium consisting of a mixture of dye solutions with high output characteristics at the assigned wavelengths of 610 and 670 nm is created. © *1999 American Institute of Physics.* [S1063-7850(99)01604-3]

The possible types of lasers widely used in everyday practice include tunable dye lasers. As was noted in a recent survey of the world market of laser technologies,[1] the areas of practical application of these lasers are constantly expanding.

This is attributed to the unique properties of these lasers, which are reliable high-power sources of low-divergence monochromatic coherent radiation that can easily be tuned over the entire visible range, as well as in the near-UV and IR spectral ranges ($\lambda = 0.26 - 1.1$ μm). None of the other types of lasers offers these features.

However, as a rule, these lasers are fairly complicated, cumbersome, and expensive, especially in regard to their principal element, the organic dyes serving as the active laser medium. Therefore, the areas of application of such lasers are restricted. They are usually areas requiring a reliable high-power laser source of radiation with high output characteristics that can be tuned over a fairly broad spectral range or can generate radiation at strictly defined wavelengths which are inaccessible or not cost-effective when other types of lasers are used.

Such situations are encountered fairly often in research experimentation and in medical practice (diagnostics, therapy, and surgery), i.e., where a high degree of selectivity of the working process must be ensured.

For example, in nuclear physics one of the most important problems for the near future is determining the number of short-lived nuclei of the radioactive isotope $^3Li_{11}$ and investigating their characteristics. On the basis of this information, conclusions can be drawn regarding leaks in commercial and research nuclear reactors and their efficiency. Such investigations are usually carried out using multiphoton laser resonance ionization spectroscopy, which was developed by V. S. Letokhov *et al.*[2] Investigating $^3Li_{11}$ by this method requires three high-power laser beams with high output characteristics at $\lambda_1 = 510 - 580$ nm, $\lambda_2 = 610$ nm, and $\lambda_3 = 670$ nm strictly synchronized in space (to within 1 μm) and time (to within 1 ns). While the first of these beams can be ob-

tained fairly easily, for example, from a Cu^+ vapor laser ($\lambda = 510$ and $\lambda = 578$ nm) or from the second harmonic of a solid-state Nd^{3+}–YAG laser ($\lambda = 532$ nm), obtaining the second and third working beams of light is a formidable task. They can be produced only by a pulsed tunable dye laser.

An analysis of the lasing characteristics of known organic dyes[3] showed that these wavelengths, unfortunately, fall on the tails of the lasing curves of the most widely used dyes. Hence the creation of a high-power laser with high output characteristics at $\lambda = 610$ $\lambda = 670$ nm is a fairly complicated task. Thus, apart from the fact that an exotic laser with high output characteristics is needed to solve the problem posed, it must also operate in an exotic regime with an exotic active medium.

A detailed combined analysis of the dynamics of the lasing, photochemical deactivation, and reduction regimes of dye molecules, as well as their laser pumping was given in Ref. 4. It was noted that conditions for the steady operation of a liquid dye layer can be created in this regime under certain conditions when the dye-flow–pump-radiation–cavity system is far from equilibrium and that the deviation of the system from equilibrium is considerably smaller in this quasiequilibrium window[5] than under ordinary conditions. This permits significant improvement of the output characteristics of the laser. A novel dye laser active element[6] was designed on the basis of the effect and was found to exhibit good output and service characteristics. Mixtures of solutions of various dyes in diverse concentrations can be used to create an exotic active medium.[7] Let us consider the conditions and method for designing and preparing such mixtures.

First, the dyes employed as ingredients in such a working mixture must be chemically compatible. Complicated high-molecular-weight biopolymers (rhodamines, oxazines, coumarins, oxadiazoles, phenylamines, etc.) are employed as active laser media, but the latter can also be relatively simple acids (for example, aminobenzoic acids) and salts (for ex-

ample, alkali-metal and alkaline-earth-metal nitrates, brilliant dyes, sulfoflavins, etc.). To simplify the problem, let us calculate the output characteristics of a mixture of two biopolymers with the molecular weights $N_m^{1,2}$, the densities $\rho_{1,2}$, and the kinematic viscosities $\eta_{1,2}$. Let them be chemically compatible, i.e., chemically neutral toward one another and the solvents used. As the latter we shall take a single simple solvent, for example, high-purity ethanol C_2H_5OH.

Second, these two dyes must be spectroscopically compatible, i.e., excited fairly easily by the pump radiation [for example, the fundamental light from a copper laser ($\lambda = 510$ or $\lambda = 578$ nm) or the second harmonic of a neodymium laser ($\lambda = 532$ nm)]. This implies closeness of the absorption band peaks at λ_{1a}^m and λ_{2a}^m with high values of the absorption cross sections σ_{1a} and σ_{2a} at the wavelength of the pump radiation. It is also desirable that the required lasing wavelength of the mixture be on the red tail of the lasing curve of one ingredient and on the blue tail of the lasing curve of the other ingredient and that the fluorescence quantum efficiencies $j_f^{1,2}$ of the possible components of the mixture in the assigned spectral range be fairly high.

When these two conditions are satisfied, the working mixture of two dyes in ethanol should lase efficiently at the assigned wavelength as a result of intermolecular interactions. An analysis of the literature[3,8–10] showed that at $\lambda = 610$ nm mixtures of Rhodamine 6G and Rhodamine 4C perchlorate (R6G and R4CP) or Safranine T (ST) can work on the blue side of the spectrum and that mixtures of phenylamines 166 and 439 (FA166 and FA439) can work on the red side. For $\lambda = 670$ nm the same phenylamines (FA166 and FA439), which have a high fluorescence quantum efficiency j_f in this spectral range, can be the blue components of the mixture, and it is reasonable to employ either oxazine-1 perchlorate (O1P) or the A and B isomers of Nile blue (NA and NB) as the red components of the working mixture.

In addition, as we have already noted above, when a dye-flow–pump-radiation–cavity system is far from equilibrium, it is possible to ensure conditions for the stable stationary operation of dye lasers in this quasiequilibrium window. In the design described in Ref. 6, one of these conditions is matching of the dynamics of the pumping and circulation of our dye mixtures to the dynamics of their photodeactivation and reduction when the stroboscopic effect is eliminated. This condition requires that the angular velocity w of the cell with the dye mixture in the active element of the liquid laser satisfy

$$w \in \left[\frac{10r}{\pi\varnothing_g^2 l_g} \frac{1}{N_a N_m} \xi N_{\text{ph}}, \; \frac{2\pi r}{\varnothing_g^2 \tau_{\text{red}}} \right]^2, \tag{1}$$

where r is the radius of the cell with the dye, $\varnothing_g$ and l_g are the diameter and length of the lasing zone in it, N_a and N_{ph} are Avogadro's number and the number of photons in the pump radiation pulse, and ξ and τ_{red} are the photodeactivation efficiency and reduction time of the working dye molecules under the action of the pump radiation pulse. Hence it can be seen that the molecular weight, photodeactivation efficiency, and reduction time of both components of the working mixture $\{N_m, \xi, \tau_{\text{red}}\}^{1,2}$ must satisfy the condition (1).

Another condition for attaining an efficient lasing regime in a dye laser is laminar flow of the dye in the design under consideration, which is a special case of Couette flow.[11] This condition requires that the Reynolds number Re satisfy

$$\text{Re} = \frac{wr^2}{\eta} \in [0, 2^{\leftarrow} \times 10^4], \tag{2}$$

whence follows the condition of matching of the kinetic viscosities $\{\eta\}^{1,2}$ of the mixture components.

Finally, according to Ref. 4, on the one hand, the photothermodynamic fluctuations of the flow of the working dye mixture appearing under the action of the pump radiation pulse must also lie within a certain quasiequilibrium window, and, on the other hand, the accompanying photoconvection of the dye flow must provide for sufficiently rapid replacement of the deactivated molecules of both components in the mixture. This requires that the intensity of the pump radiation pulse I_0 and the Rayleigh number Ra not exceed certain critical values:

$$\begin{cases} I_0 = \dfrac{4P_0}{\pi\varnothing_g} < I_{0_c}^{1,2} = \left(D \dfrac{\rho c \eta^2}{(\sigma_a N_m) g \beta r^3 \tau_0} \right)^{1,2}, \\[2mm] \text{Ra}^{1,2} = \left(\dfrac{(\sigma_a N_m) I_0 g \beta r^5}{\kappa \chi \eta} \right)^{1,2} < \text{Ra}_c^{1,2} = \left(\dfrac{g^2 \beta r^4}{c \chi \eta} \right)^{1,2}, \\[2mm] D_{1,2} \cong 1; \quad g = 9.8 \dfrac{m}{c^2}. \end{cases} \tag{3}$$

Here P_0 and τ_0 are the power and duration of the pump radiation pulse, $c_{1,2}$ and $\beta_{1,2}$ are the specific heats and volumetric expansion coefficients of the components of the working mixture, and $\kappa_{1,2}$ and $\chi_{1,2}$ are their thermal conductivities and thermal diffusivity. The conditions (3) also impose requirements on the properties $\{c, \beta, \kappa, \chi\}$ of both components of the working mixture.

Thus, as the deviation of the dye-flow–pump-radiation–cavity system from equilibrium increases, the structure of the working mixture changes if the system approaches a quality boundary, where $\lambda \to \lambda_s$, $\tau \to \tau_s$, $\varepsilon \to \varepsilon_s$. The lasing dynamics of this mixture become anomalous, allowing the achievement of high output characteristics for the exotic dye mixture serving as the active working medium of an exotic liquid laser operating in an exotic regime in some quasiequilibrium window,[5] which is specified by physicochemical characteristics $\{c, \rho, \chi, \kappa, \eta, \beta, \xi, \tau_{\text{red}}, c, \lambda_a, \lambda_f, \sigma_a, j_f\}^{1,2}$ of the working components of the mixture, the properties $\{w, r, \varnothing_g, l_g\}$ of the flow of the mixture and the laser design, and the parameters $\{P_0, \tau_0\}$ of the pump radiation. This enables us to solve the problem posed and to obtain high-power beams of laser radiation at the exotic wavelengths $\lambda = 610$ and $\lambda = 670$ nm with good parameters. Such beams are needed to determine the number and explore the characteristics of short-lived $^3\text{Li}_{11}$ nuclei, which are important for nuclear physics. This problem was successfully solved in an experiment with pump radiation from copper-vapor lasers with $\lambda = 510$ and $\lambda = 578$ nm.

Thus, experimental confirmation of the law of alternating nonequilibrium[5] has been obtained, permitting us to obtain an important experimental finding. It is highly probable

that the method considered here can be used to calculate and obtain other exotic lasing wavelengths with high characteristics that are needed to solve specific practical problems.

[1] S. G. Anderson, Laser Focus World , No. 1, 73 (1997); No. 2, 84 (1997).

[2] V. S. Letokhov *Nonlinear Selective Photoprocesses in Atoms and Molecules*, [in Russian], Nauka, Moscow (1988), 408 pp.

[3] *Spectra-Physics Prospectus*, Mountain View, CA (1986), 42 pp.; *Lambda-Physics Prospectus*, Acton, MA (1997), 26 pp.

[4] G. A. Vesnicheva and A. Yu. Ivanov, Zh. Tekh. Fiz. **64**(1), 201 (1994) [Tech. Phys. **39**, 114 (1994)].

[5] G. E. Skvortsov, Pis'ma Zh. Tekh. Fiz. **23**(10), 17 (1997) [Tech. Phys. Lett. **23**(5), 383 (1997)].

[6] G. A. Vesnicheva, A. Yu. Ivanov, and I. V. Skokov, USSR Inventor's Certificate (Patent) No. 1,739,424 (Cl. H01S3/02), priority from 13 January 1989, published 8 February 1992.

[7] M. G. Raymer, Z. Deng, and M. Beck, J. Opt. Soc. Am. B **5**, 1588 (1988).

[8] *Laser Handbook, Vol. 1* [in Russian], A. M. Prokhorov (Ed.), Sov. Radio, Moscow (1973), 504 pp.

[9] A. V. Aristov and V. S. Shevandin, Opt. Spektrosk. **43**, 228 (1977) [Opt. Spectrosc. **43**, 131 (1977)].

[10] T. G. Pavlopoulus and D. J. Golich, J. Appl. Phys. **64**, 521, 560 (1988).

[11] R. J. Donnelly, Phys. Today **11**, 320 (1992).

Translated by P. Shelnitz

Theory of the undulator superradiance of an electron beam pulse in the group synchronism regime

N. S. Ginzburg, I. V. Zotova, and A. S. Sergeev

Institute of Applied Physics, Russian Academy of Sciences, Nizhniĭ Novgorod
(Submitted November 18, 1998)
Pis'ma Zh. Tekh. Fiz. **25**, 8–16 (April 26, 1999)

The properties of the superradiance of a short electron beam pulse moving in an undulator field and exciting a waveguide mode field under group synchronism conditions are analyzed. This regime is shown to be characterized by the maximum growth rate of superradiance instability. The development of such instability results in bunching of the particles and the coherent emission of a short electromagnetic pulse by the beam pulse. © *1999 American Institute of Physics.* [S1063-7850(99)01704-8]

A great deal of attention has recently been focused on the theoretical investigation of the superradiance of spatially localized electron beam pulses.[1–8] Superradiance involves the coherent emission of a considerable fraction of the beam-pulse particles in a zone with dimensions exceeding the wavelength in the general case. This becomes possible as a result of the development of bunching of the particles within the beam pulse, as well as the mutual influence of different parts of the beam pulse due to slippage of the wave relative to the beam pulse. In most of the theoretical studies devoted to this problem it was assumed that this slippage is due to the difference between the group velocity of the wave and the translational velocity of the beam pulse.[2,3] At the same time, there is special interest in the case of group synchronism, in which the translational velocity of the beam pulse coincides with the group velocity of the wave, $V_\parallel \approx V_{gr}$. In this case the mutual influence of the electrons, as well as the flow of electromagnetic energy out of the interaction space, are caused by dispersive spreading of the wave packet. Moreover, as was shown in Refs. 8–10, the group synchronism regime is optimal for observing the cyclotron mechanism of superradiance. Experiments on the generation of ultrashort microwave pulses in such a regime when an electron beam pulse moves in the field of a helical undulator were described in Ref. 11. The radiation propagated in a cylindrical waveguide, and the electron beam pulse had a cylindrical shape and was focused by a uniform magnetic field. The present paper is devoted to a theoretical analysis of the features of undulator superradiance in the group synchronism regime.

Let us consider the emission from an electron beam pulse, whose particles move along helical trajectories in the field of an undulator of corresponding symmetry:

$$\mathbf{H}_u = \mathrm{Re}(A_u \hat{\mathbf{H}}_u \exp(ik_u z)), \quad \hat{\mathbf{H}} = \psi_u \mathbf{z}_0 + ik_u^{-1}\nabla_\perp \psi_u, \quad (1)$$

where $\psi_u = I_1(k_u r)\exp(i\varphi)$ is the membrane function, $k_u = 2\pi/d$, d is the undulator period, and $I_1(x)$ is a modified Bessel function.

In the group synchronism regime the dispersion characteristics of the waveguide mode $h = c^{-1}\sqrt{\omega^2 - \omega_c^2}$ and the electron flux $\omega - hV_\parallel = \omega_u$, where ω_c is the cutoff frequency

and $\omega_u = k_u V_\parallel$ is the oscillation frequency of the particles, exhibit tangency (Fig. 1a). The interaction of the electrons with the magnetic field in this regime can be analyzed most simply in the local K' reference frame moving with the translational velocity of the beam pulse. Using the Lorentz transformation, we can easily show that the longitudinal wave number h' in the K' frame tends to zero in this case and that the beam pulse emits at a quasicritical frequency in this frame as a result (Fig. 1b).

Assuming that the transverse structure of the radiation field coincides with one of the waveguide modes and choosing the cutoff frequency as the carrier frequency, we represent the radiation field in the form

$$\mathbf{E}'_s = \mathrm{Re}(\hat{\mathbf{E}}_s(\mathbf{r}_\perp)A'(z',t')\exp[i\omega_c t']),$$

$$\hat{\mathbf{E}}_s = \kappa^{-1}[\nabla_\perp \psi_m, \mathbf{z}_0], \quad (2)$$

where the membrane function has the form $\psi_m = J_m(\kappa r)\exp(im\varphi)$ for a cylindrical waveguide, m is the azimuthal mode index, κ is the transverse wave number, and $J_m(x)$ is a Bessel function.

In the local reference frame the undulator field transforms into an electromagnetic wave, whose transverse components are given by the relations

$$\mathbf{H}'_{u_\perp} = \mathrm{Re}(A_u \gamma_\parallel \hat{\mathbf{H}}_{u_\perp}\exp[i(\omega'_u t' + h'_u z')]),$$

$$\mathbf{E}'_{u_\perp} = \beta_\parallel \gamma_\parallel [\mathbf{z}_0, \mathbf{H}_{u_\perp}], \quad (3)$$

where $\gamma_\parallel = (1 - V_\parallel^2/c^2)^{-1/2}$ and $\omega'_u = \gamma_\parallel \omega_u$, $h'_u = h_u \gamma_\parallel$.

Thus, in the K' frame an electron beam pulse, which is stationary as a whole, is subjected to the effects of the pump wave (3), and excites the scattered field (2), whose frequency, like the pump frequency, is close to the cut off frequency. In these fields the averaged equations of motion of electrons, which describe longitudinal bunching, can be written in the form of the equations of a pendulum[12]

$$\frac{\partial^2 \theta}{\partial \tau'^2} = \mathrm{Re}(Ka'_s a_u^* \exp[i\theta]), \quad (4)$$

a

b
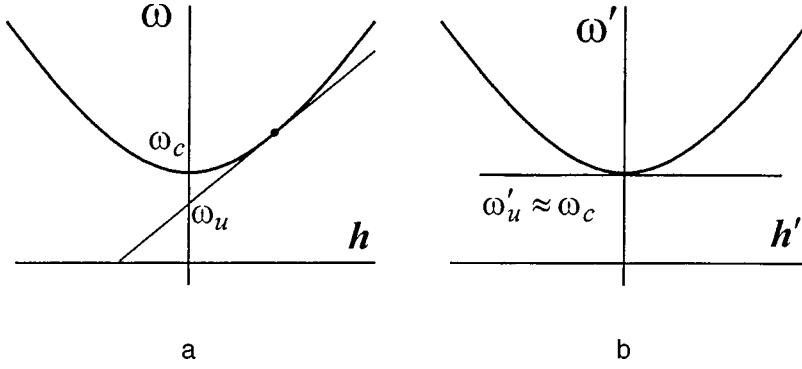
FIG. 1. Dispersion diagrams of the group synchronism regime in the laboratory (a) and local (b) reference frames.

where $\theta = (\omega_c - \omega_u')t' - h_u'z'$ is the combination phase, $\tau' = \omega_c t'$ $a_s' = eA'\gamma_\parallel/2mc\omega_c$, $a_u = eA_u\gamma_\parallel/2mc\omega_u'$, and

$$K = \left\{ \frac{\omega_c}{\omega_c - \omega_H} J_{m-1}(\kappa_s R_0) I_0(k_u R_0) \right.$$

$$\left. - \frac{\omega_c}{\omega_c + \omega_H} J_{m+1}(\kappa_s R_0) I_2(k_u R_0) \right\}$$

$$\times \exp[-i(m-1)\varphi]$$

is the coupling coefficient written under the assumption that the electron beam pulse has a cylindrical shape with a mean radius R_0 and is injected along the guiding magnetic field, whose intensity is far from the resonance value, and ω_H is the gyrofrequency.

When there is emission at the quasicritical frequency, the evolution of the longitudinal profile of the field can be described by the inhomogeneous parabolic equation

$$i\frac{\partial^2 a_s'}{\partial Z'^2} + \frac{\partial a_s'}{\partial \tau'} = 2Ma_u K^* f(Z') \frac{1}{\pi} \int_0^{2\pi} \exp(-i\theta) \, d\theta_0, \qquad (5)$$

where the excitation factor can be found from the solution of the electron equations of motion (4). Here $Z' = \sqrt{2}z'\omega_c/c$, $M = (eI_0/16\pi^2mc^3)d\lambda_c\gamma_\parallel R^{-2}J_m^{-2}(\nu_n)(1-m^2/\nu_n^2)^{-1}$ is the form factor, R is the radius of the waveguide, I_0 is the electronic current in the laboratory frame, and $\lambda_c = 2\pi c/\omega_c$. The function $f(Z')$ describes the longitudinal density distribution of the beam pulse. The boundary and initial conditions for Eqs. (4) and (5) have the form

$$\theta|_{\tau'=0} = \theta_0 + r\cos\theta_0, \qquad \theta_0 \in [0, 2\pi],$$

$$\frac{\partial\theta}{\partial\tau'}\Big|_{\tau'=0} = -\Delta, \qquad a_s'|_{\tau'=0} = 0,$$

where $\Delta = (\omega_u' - \omega_c)/\omega_c$ is the mismatch between the frequency of the electron oscillations in the pump field and the cutoff frequency and the parameter $r \ll 1$ assigns small initial fluctuations of the beam-pulse density.

Let us next explore the case of a relatively short beam pulse satisfying the condition

$$b'^2/\lambda_c cT' \ll 1, \qquad (6)$$

where $b' = b\gamma_\parallel$ is the length of the electron beam pulse and T' is the time for development of the process (the inverse growth rate). In this case we can set $f(Z') = B\delta(Z')$, where

$B = \sqrt{2}b'\omega_c/c$ and $\delta(Z')$ is a delta function. When the condition (6) is satisfied, the length of the beam pulse is significantly shorter than the wavelength of the radiation in the waveguide, but still exceeds the pump wavelength $b'h_u' \gg 1$. For this reason, coherence of the radiation from the entire volume of the beam pulse can be ensured only by means of particle bunching. In the case under consideration, after minimization of the number of independent parameters, the equations are reduced to the form
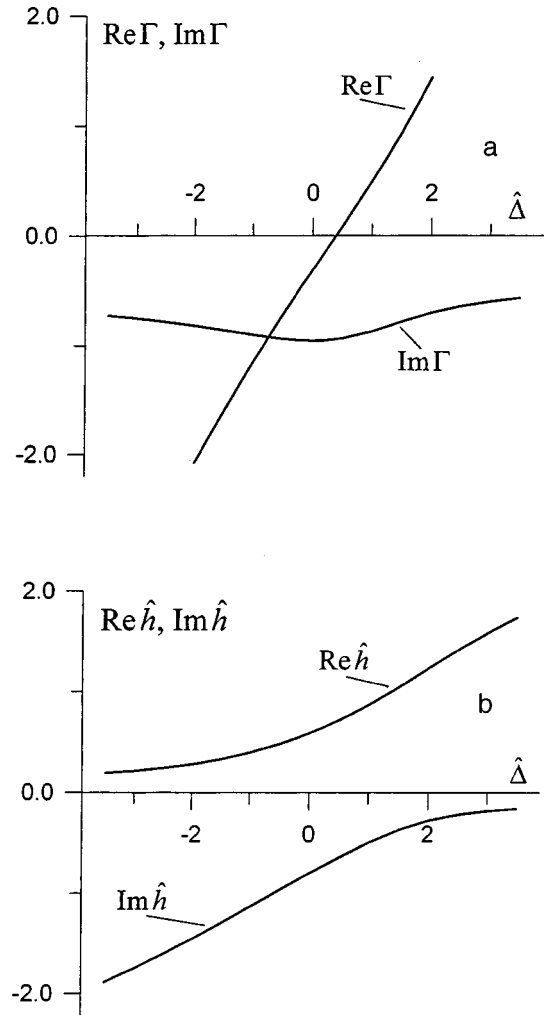
FIG. 2. Growth rate and electron frequency shift (a) and the real and imaginary parts of the longitudinal wave number of the eigenmode excited (b) versus the mismatch parameter.
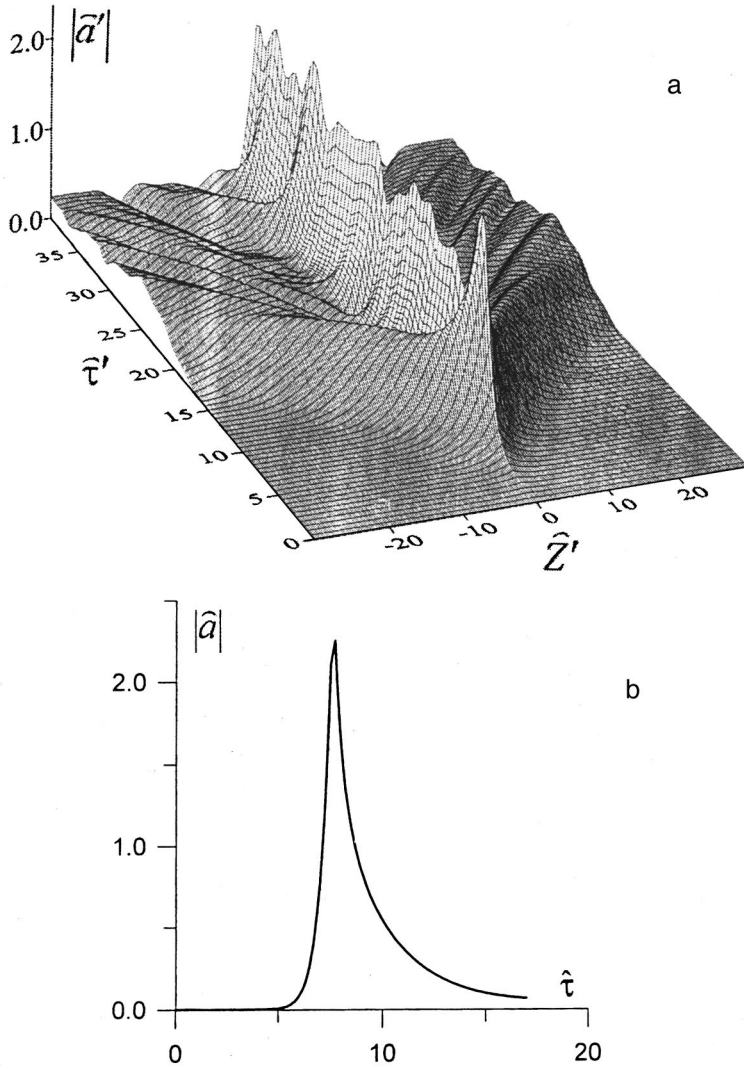
FIG. 3. Distribution of the field in the local reference frame (a) and superradiance pulse received by the detector in the laboratory frame (b).

$$i\frac{\partial^2 \hat{a}'}{\partial \hat{Z}'^2} + \frac{\partial \hat{a}'}{\partial \hat{\tau}'} = \frac{2}{\pi}\delta(\hat{Z}')\int_0^{2\pi}\exp(-i\theta)\,d\theta_0,$$

$$\frac{\partial^2 \theta}{\partial \hat{\tau}'^2} = \mathrm{Re}(\hat{a}'\exp[i\theta]), \qquad (7)$$

where $\hat{\tau}'=\tau'G$, $\hat{Z}'=G^{1/2}Z'$, $\hat{a}=a_s'a_u^*KG^{-2}$, and $G=(MB|a_u|^2|K|^2)^{2/5}$. It is important to stress that Eqs. (7), which describe the superradiance process under group synchronism conditions, are completely analogous to the equations describing the channeling of radiation by a ribbon-shaped stream of electrons.[13]

To investigate the linear stage of superradiance, we present the radiation field in the form $\hat{a}=a_0\exp[i\Gamma\hat{\tau}'-i\hat{h}'|Z'|]$ and linearize Eqs. (7). As a result we obtain the characteristic equation

$$\hat{h}(\hat{h}^2-\hat{\Delta})^2=i, \qquad (8)$$

which specifies complex eigenfrequencies $\Gamma=\hat{h}^2$. In the case of exact group synchronism ($\hat{\Delta}=0$), only one of the five eigenmodes which are solutions of (8) is a mode which grows with time [$\mathrm{Im}\,\Gamma=-\sin(2\pi/5)$] and has an electro-

magnetic energy flux directed from the electron beam pulse toward the external space [$\mathrm{Re}\,\hat{h}>0$]. For this mode it is important to stress that the field amplitude drops fairly rapidly with increasing distance from the beam pulse, $\mathrm{Im}\,\hat{h}<0$. The growth rate of the superradiance instability is determined by excitation of the mode indicated and is given in dimensional quantities by the relation

$$|\mathrm{Im}\,\omega'|=\omega_c\sin\left(\frac{2\pi}{5}\right)$$

$$\times\left[\frac{1}{4\sqrt{2}\pi}\left(\frac{eI_0}{mc^3}\right)\frac{bd}{R^2}\gamma_\parallel^2\frac{|a_u|^2|K|^2}{J_m^2(\nu_n)(1-m^2/\nu_n^2)}\right]^{2/5}. \quad (9)$$

It should be noted that, first, the growth rate is determined by the total charge of the beam pulse and that, second, despite the flow of electromagnetic energy into the external space, the instability has a threshold-free character. The latter is due to the infinite lifetime of the particles within the beam pulse.

Plots of the growth rate, the electron frequency shift, and the imaginary and real parts of the longitudinal wave number $\hat{h}$ versus the mismatch parameter $\hat{\Delta}$ are shown in Fig. 2, whence it follows that a deviation from the group synchro-

nism regime reduces the growth rates. It is noteworthy that the simple mode under consideration does not allow for space charge, whose inclusion should shut off the instability at fairly large negative values of $\hat{\Delta}$, where the electron oscillation frequency is significantly smaller than the cutoff frequency. At the same time, the instability continues to exist at arbitrary positive values of $\hat{\Delta}$. In this case there is a drop in the instability growth rate with a simultaneous increase in the flow of energy into the external space, which is caused by a rise in the group velocity due to an increase in Re $\hat{h}$.

Figure 3a presents the results of numerical simulation of the nonlinear stage on the basis of Eqs. (7). The evolution of the profile of the electric field amplitude in the local reference frame is shown. In this frame the electron beam pulse radiates isotropically in the $\pm z'$ directions along the waveguide axis. At the same time, in the laboratory frame, if the translational velocity of the beam pulse exceeds the group velocity of the wave, both components of the radiation propagate in the positive direction of the z' axis. To find the field received by a detector in the laboratory K frame, the line $z' + V_\parallel t' = \text{const}$, along which the detector moves in the local K' reference frame, should be constructed in the (z',t') plane. The detector signal obtained using such a procedure will have the form of a fairly short pulse (Fig. 3b). The peak power in the pulse is given by the expression

$$P = 2\pi^2 (m^2 c^5/e^2)(|\hat{a}'|^2/|\hat{a}_u|^2)G^4 J_m^2(\nu_n)$$
$$\times (1 - m^2/\nu_n^2)R^2 \lambda_c^{-2}\beta_\parallel. \tag{10}$$

In conclusion, let us use the relations obtained to evaluate the results of the experiment in Ref. 11, in which the beam-pulse current was 250 A, the beam-pulse length was $b = 4.5$ cm, the particle energy was 200 keV, the undulator field strength was 2.2 kOe, the guiding field strength was 13 kOe, and the TE_{11} mode was excited at 28 GHz in a waveguide with a radius of 0.5 cm. From Eq. (9), for the growth rate we have 7×10^9 s^{-1}. This value is consistent with the fact that the undulator length of 25 cm, which was traversed by the particles in 1 ns, was sufficient for observing super-

radiance. The superradiance pulse duration for the parameters just indicated should be of the order of 350 ps, in agreement with the experimental data. Formula (10) gives an estimate of roughly 15 MW for the absolute power of the superradiance pulses in the saturation regime. The experimentally recorded peak power was of the order of 250 kW. The reason for the significant disparity may be that the undulator length was insufficient for observing the saturation regime, as well as the influence of the velocity spread of the particles. It should also be noted that this disparity is partially attributable to the errors (in the downward direction) in the measurement of the absolute power of ultrashort subnanosecond microwave pulses.

[1] V. V. Zheleznyakov, V. V. Kocharovskiĭ, and Vl. V. Kocharovskiĭ, Usp. Fiz. Nauk **159**(2), 193 (1989) [Sov. Phys. Usp. **32**(10), 835 (1989)].

[2] R. Bonifacio, C. Maroli, and N. Piovella, Opt. Commun. **68**, 369 (1988).

[3] R. Bonifacio, N. Piovella, and B. W. J. McNeil, Phys. Rev. A **44**, 3441 (1991).

[4] N. S. Ginzburg, Pis'ma Zh. Tekh. Fiz. **14**(5), 440 (1988) [Sov. Tech. Phys. Lett. **14**(3), 197 (1988)].

[5] N. S. Ginzburg and A. S. Sergeev, Pis'ma Zh. Tekh. Fiz. **16**(20), 9 (1990) [Sov. Tech. Phys. Lett. **16**(10), 768 (1990)].

[6] L. A. Vaĭnshteĭn and A. I. Kleev, Dokl. Akad. Nauk SSSR **301**, 862 (1990) [Sov. Phys. Dokl. **35**, 359 (1990)].

[7] D. A. Jarosynski, P. Chaix, N. Piovella *et al.*, Phys. Rev. Lett. **78**, 1699 (1997).

[8] N. S. Ginzburg, I. V. Zotova, and A. S. Sergeev, JETP Lett. **60**, 513 (1994).

[9] N. S. Ginzburg, I. V. Zotova, A. S. Sergeev *et al.*, JETP Lett. **63**, 331 (1996).

[10] N. S. Ginzburg, I. V. Zotova, A. S. Sergeev *et al.*, Phys. Rev. Lett. **78**, 2365 (1997).

[11] N. S. Ginzburg, A. S. Sergeev, I. V. Zotova *et al.*, Nucl. Instrum. Methods Phys. Res. A **393**, 352 (1997).

[12] V. L. Bratman, G. G. Denisov, N. S. Ginzburg, and M. I. Petelin, IEEE J. Quantum Electron. **QE-19**, 282 (1983).

[13] N. S. Ginzburg and A. S. Sergeev, Zh. Tekh. Fiz. **60**(8), 40 (1990) [Sov. Phys. Tech. Phys. **35**, 896 (1990)].

Translated by P. Shelnitz

Longitudinal chromatic aberration of an accelerating gap

A. M. Tron'

Moscow State Engineering-Physics Institute (Technical University), Moscow

An expression for the longitudinal chromatic aberration of an accelerating gap with an arbitrary distribution of the electrostatic field along the electron trajectory is presented, and a method is proposed for reducing it in time-transforming chronographs to values of order 10 fs. © *1999 American Institute of Physics.* [S1063-7850(99)01804-2]

The main factor restricting the temporal resolution of a time-transforming chronograph of the streak camera type is the longitudinal chromatic aberration of its accelerating gap,[1] which is defined here as the spread of the time of flight of electrons across the gap due to their initial distribution with respect to the longitudinal component of the velocity. This paper explores the possibility of reducing this aberration to the smallest possible values. For this purpose we first determine the expression for the time of flight of a nonrelativistic electron across a gap, which is formed in the general case by a cylindrical emitter and a flat electrode.

Let an emitter of circular cross section with an arbitrary radius R be at a potential $-U_0$ relative to an electrode, and let an electron move along the x coordinate axis, which coincides with the line of intersection of two orthogonal symmetry planes of the field. Then, in a system of units in which the electron charge equals -1 and its energy is given in electron volts, the familiar expression[2] for the time of flight across a gap takes the form

$$t = \frac{1}{c}\sqrt{\frac{W_0}{2}}\int_{U_0}^{0}\frac{1}{E}\frac{dU}{\sqrt{W-U}}, \tag{1}$$

where c is the speed of light; W and W_0 are, respectively, the total energy and the rest energy of the electron; and U and E are the potential energy of the electron and its rate of variation along the x axis, which are numerically equal to the absolute values of the potential and field intensity, respectively, in the specified system of units.

The integrand function $1/E$ is continuous and monotonic in its domain of definition $U \in [U_0, 0]$. Then, according to the second mean value theorem in integral calculus,[3] this integral can be represented in the form

$$\int_{U_0}^{0}\frac{1}{E}\frac{dU}{\sqrt{W-U}} = \frac{1}{E_m}\int_{U_0}^{U_\xi}\frac{dU}{\sqrt{W-U}} + \frac{1}{E_h}\int_{U_\xi}^{0}\frac{dU}{\sqrt{W-U}}, \tag{2}$$

where E_m and E_h are, respectively, the maximum value of the field intensity at the emitter and the field intensity at the electrode at the end of the gap of length h under consideration and U_ξ is a value which must be determined.

In the electrode system under consideration E_m and E_h equal

$$E_m = -\frac{U_0}{h}k = -\frac{U_0}{h}\frac{\sqrt{m(m+2)}}{\ln(m+1+\sqrt{m(m+2)})}, \tag{3}$$

$$E_h = \frac{2}{m+2}E_m, \tag{4}$$

where $m = h/R$ and k is the field intensity amplification factor at the emitter.

To simplify and make the representation of the ensuing expressions more explicit, we determine U_ξ from Eq. (2) under the assumption that $W = U_0$ holds here. We multiply both sides of Eq. (2) by $1/\sqrt{\alpha - U_0}$ and integrate over U_0 from 0 to α. Then, setting $\alpha = U_0$, we obtain an algebraic equation in U_ξ, whose solution is

$$\xi \equiv \frac{U_\xi}{U_0} = 2\frac{k-1}{m}. \tag{5}$$

With consideration of the definition (5) and the representation (2), the integration in (1) gives an expression for the time of flight of an electron with the initial energy W_{0i} across a gap:

$$t(W_i) = t_0\frac{2}{k}\left\{\sqrt{1+W_i}-\sqrt{W_i}+\frac{m}{2}[\sqrt{1+W_i}-\sqrt{1-\xi+W_i}]\right\}, \tag{6}$$

where $t_0 = (h/c)\sqrt{W_0/(2U_0)}$ and $W_i = W_{0i}/U_0$.

Then the longitudinal chromatic aberration of the gap is defined as

$$\Delta t = t(W_1) - t(W_2), \tag{7}$$

where we assume $W_2 > W_1$, and W_1 and W_2 are defined as the boundaries of the confidence interval from the initial energy distribution of the electron, which corresponds to its distribution with respect to the longitudinal component of the velocity.

As a rule, $W_i < 0.01$. Then, expanding the square roots in formula (6) into series in powers of W_i, we simplify (7) and represent it in an explicit form:

$$\Delta t \cong t_0\frac{2}{k}\left\{\sqrt{W_2}-\sqrt{W_1}-\left[1+\frac{m}{2}\left(1-\frac{1}{\sqrt{1-\xi}}\right)\right]\frac{W_2-W_1}{2}\right\}. \tag{8}$$
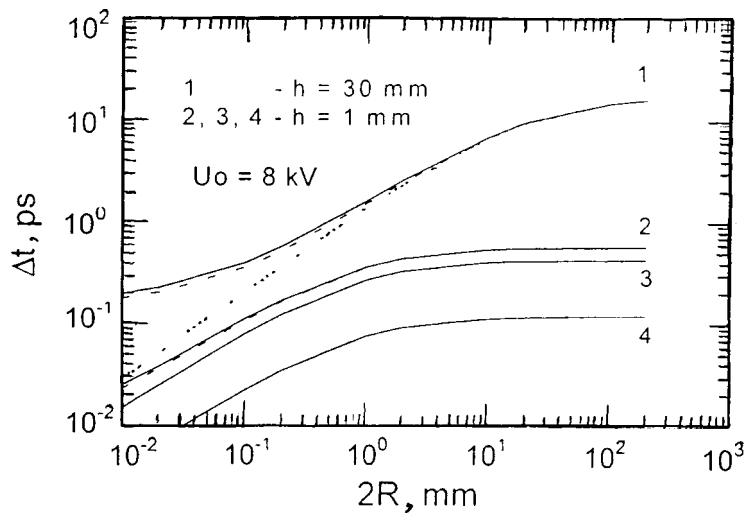
FIG. 1. Dependence of the longitudinal chromatic aberration of an accelerating gap on emitter radius. The notation is explained in the text.

Figure 1 presents the dependence of the aberration on the emitter radius for two values of the gap width h, 1 and 30 mm, and an accelerating voltage equal to 8 kV, where the solid lines are plots of the results obtained by numerical integration of the relativistic equation of motion,[4] the dashed lines are plots of the results obtained from formula (8), and the points are the results obtained from formula (8) without consideration of the expansion term which is linear with respect to W_i. At large values of R these lines essentially coincide for the same initial energy spread, which is indicated in the figure by the numbers of the curves: 1 and 2 — $W_{01} = 0.335$ eV and $W_{02} = 3.925$ eV, which correspond to a secondary-electron emitter in a monitor of the phase distribution of particles in a beam pulse;[4] 3 — $W_{01} = 0$ and $W_{02} = 1.1$ eV for the case of the photocathode of a chronograph for x radiation; 4 — $W_{01} = 0.5$ eV and $W_{0.2} = 1$ eV, as an example for the case of a chronograph for electromagnetic radiation in the visible region of the spectrum. It follows from the plots presented that the error of the calculations based on formula (8) is negligibly small and that reduction of the longitudinal chromatic aberration of the gap by one to two orders of magnitude down to a value of the order of 10

fs is possible when emitters with a small radius of curvature are employed. We note that the use of such emitters is most efficient in instruments with longitudinal modulation of the electron beam.[4]

We thank I. G. Merinov for assisting in the numerical calculations.

[1] E. K. Zavoĭskiĭ and S. D. Fanchenko, Dokl. Akad. Nauk SSSR **226**, 1062 (1976) [Sov. Phys. Dokl. **21**, 107 (1976)].

[2] L. D. Landau and E. M. Lifshitz, *Mechanics*, 2nd ed., Pergamon Press, Oxford–New York (1969) [Russ. original, Nauka, Moscow (1965), 204 pp.].

[3] V. I. Smirnov, *A Course of Higher Mathematics, Vol. 2: Advanced Calculus*, Addison-Wesley, Reading, Mass. (1964) [Russ. original, Gostekhizdat, Moscow–Leningrad (1967), 627 pp.].

[4] A. M. Tron and I. G. Merinov, in *Proceedings of the 18th Linear Accelerator Conference, 21–26 August 1966, Geneva*, CERN (1996), pp. 514–517.

Translated by P. Shelnitz

Influence of a thin layer with arbitrary conductivity on the characteristics of acoustic waves in potassium niobate

Yu. V. Gulyaev, I. E. Kuznetsova, B. D. Zaĭtsev, S. G. Joshi, and I. A. Borodina

Saratov Branch of the Institute of Radio Engineering and Electronics, Russian Academy of Sciences, Saratov; Marquette University, Milwaukee, WI 53210, U.S.A.
(Submitted December 10, 1998)
Pis'ma Zh. Tekh. Fiz. **25**, 21–26 (April 26, 1999)

The influence of a thin layer of arbitrary conductivity on the characteristics of acoustic waves in potassium niobate is investigated theoretically. The conductivity of a thin layer on the surface of a potassium niobate crystal or plate is shown to have a significant influence on the damping and velocity not only of symmetric Lamb waves and quasi-shear-horizontal waves but also of Gulyaev–Bleustein waves. It is found that a relative change in velocity as large as 50% can be achieved for quasi-shear-horizontal waves by altering the surface conductivity. The results obtained reveal great prospects of using potassium niobate to create acoustoelectronic devices with controllable characteristics. © *1999 American Institute of Physics.* [S1063-7850(99)01904-7]

Papers devoted to the investigation of the characteristics of both surface acoustic waves (SAWs; Ref. 1) and waves in thin plates of potassium niobate (KNbO$_3$; Ref. 2) have recently been published. This new acoustic material has very high piezoelectric, electro-optic, and nonlinear-optical coefficients.[3] It was shown in Ref. 1 that the square of the electromechanical coupling coefficient K^2 of surface waves in the X direction of a Y-cut KNbO$_3$ crystal has a value of 53%, which is roughly 10 times greater than the corresponding parameter for LiNbO$_3$. As has been reported,[4] a thin conducting layer has an effect on the characteristics of surface acoustic waves with an efficiency that depends on the electromechanical coupling coefficient of the waves. In a previous investigation of quasi-shear-horizontal (QSH) waves and symmetric (S_0) and antisymmetric (A_0) Lamb waves propagating in thin potassium niobate plates, we discovered that K^2 can reach values of 100, 60, and 20%, respectively.[2] At such high values of the electromechanical coupling coefficient it can be expected that the conductivity of a thin layer on a KNbO$_3$ surface will have a more significant effect on the characteristics of acoustic waves than will thin layers on other less piezoelectrically active crystals. This paper is devoted specifically to exploring of this question.

It was discovered as a result of the experiments performed that a wave with $K^2 = 53\%$ propagating in the X direction of a Y-cut crystal is a weakly inhomogeneous Gulyaev–Bleustein wave, rather than a Rayleigh wave, as was reported in Ref. 1. This paper describes a theoretical analysis of the influence of a thin layer of arbitrary conductivity on the damping and velocity of Gulyaev–Bleustein waves, QSH waves, and symmetric Lamb waves in potassium niobate.

The problem was solved using the standard equations of motion of an elastic medium and the Laplace equation:

$$\rho \frac{\partial^2 u_i}{\partial^2 t} = C_{ijkl} \frac{\partial^2 u_l}{\partial x_j \partial x_k} + e_{kij} \frac{\partial^2 \Phi}{\partial x_j \partial x_k}, \tag{1}$$

$$\varepsilon_{jk} \frac{\partial^2 \Phi}{\partial x_j \partial x_k} - e_{jlk} \frac{\partial^2 u_l}{\partial x_j \partial x_k} = 0, \tag{2}$$

where u_i is the displacement of the particles in the medium; x_j are the spatial coordinates; t is the time; Φ is the electric potential; ρ is the density of the medium; and C_{ijkl}, e_{kij}, and ε_{jk} are the elastic, piezoelectric, and dielectric constants of the medium, respectively.

The waves propagated along the x_1 axis, and the x_3 axis was directed into the interior of the medium. The material constants of potassium niobate needed for the calculations were taken from Ref. 3.

The mechanical and electrical boundary conditions used to analyze the propagation of Gulyaev–Bleustein waves in a semi-infinite crystal with a thin layer of arbitrary conductivity on its surface were vanishing of the mechanical stresses, continuity of the electric potential, and a jump in the normal component of the induction due to the surface charge δ on the free boundary with the vacuum:

$$\delta = -\sigma_s i \omega \Phi / V^2,$$

where σ_s is the surface conductivity, i is the unit imaginary number, and ω and V are the frequency and velocity of the acoustic wave.

When the propagation of acoustic waves in a plate was analyzed, these boundary conditions were supplemented by the conditions for the other boundary with the vacuum. Since there is no thin conducting layer on this boundary, the normal component of the induction was assumed to be continuous, and the other conditions were assumed to be identical to the conditions on the first boundary. The system of equations written together with the boundary conditions was solved by a known method.[5]
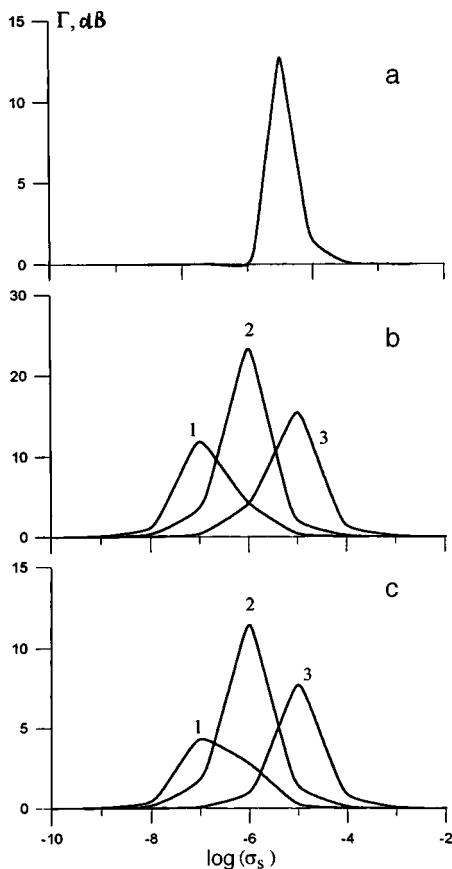
FIG. 1. Dependence of the damping of acoustic waves on the surface conductivity: a — Gulyaev–Bleustein waves ($\phi=0°$, *Y*-cut crystal), b — QSH waves ($\phi=0°$, *Y*-cut crystal), c — S_0 waves ($\phi=50°$, *Y*-cut crystal). *1* — $h/\lambda=0.01$, *2* — $h/\lambda=0.05$, *3* — $h/\lambda=0.5$.

FIG. 2. Dependence of the relative change in the velocity of acoustic waves on surface conductivity: a — Gulyaev–Bleustein waves ($\phi=0°$, *Y*-cut crystal), b — QSH waves ($\phi=0°$, *Y*-cut crystal), c — S_0 waves ($\phi=50°$, *Y*-cut crystal). *1* — $h/\lambda=0.01$, *2* — $h/\lambda=0.025$, *3* — $h/\lambda=0.1$, *4* — $h/\lambda=0.25$, *5* — $h/\lambda=0.5$.

The calculations performed yielded the dependences of the damping of Gulyaev–Bleustein waves (Fig. 1a), quasi-shear-horizontal waves (Fig. 1b), and symmetric Lamb waves (Fig. 1c) on the surface conductivity of a thin layer at the boundary for the directions characterized by the largest electromechanical coupling coefficient. In the case of the QSH and S_0 waves an analysis was performed for various thicknesses of the potassium niobate plate h/λ (h is the plate thickness, and λ is the acoustic wavelength).

The absorption maxima observed in the figure are attributed to the fact that at small values of the surface conductivity the layer does not have any influence on the acoustic waves and does not introduce damping, but at large values of σ_s the layer becomes an ideal conductor.

Figure 2 presents plots of the dependence of the relative change in the velocity of Gulyaev–Bleustein waves (a), QSH waves (b), and S_0 Lamb waves (c) on the conductivity σ_s of the thin layer on the potassium niobate surface.

It is seen that the velocity of the acoustic waves decreases with increasing conductivity and that it achieves saturation at a certain value of σ_s. The maximum value of the velocity change corresponds to the electromechanical coupling coefficient.

Thus, it can be concluded on the basis of the experiments performed that the creation of acoustoelectronic devices with controllable characteristics is possible. In addi-tion, when such devices are operated, the waves in the plates can be used in the low-frequency range, and the surface acoustic waves can be used in the high-frequency range.

[1] K. Yamanouchi, H. Odagawa, T. Kojima, and T. Matsunura, Electron. Lett. **33**, 193 (1997).

[2] I. E. Kuznetsova, B. D. Zaitsev, S. Joshi, and I. A. Borodina, Electron. Lett. **34**, (1998).

[3] M. Zgonik, R. Schlesser, and I. Biaggio *et al.*, Appl. Phys. **74**, 1287 (1993).

[4] B. D. Zaĭtsev, I. E. Kuznetsova, and I. S. Nefedov, Pis'ma Zh. Tekh. Fiz. **20**(4), 60 (1994) [Tech. Phys. Lett. **20**(2), 159 (1994)].

[5] M. K. Balakirev and I. A. Gilinskiĭ, *Waves in Piezoelectric Crystals* [in Russian], Nauka, Novosibirsk (1982), 237 pp.

Translated by P. Shelnitz

Photoluminescence of porous-silicon/diamondlike-carbon-film structures subjected to rapid thermal annealing

A. G. Rozhin, N. I. Klyuĭ, Yu. P. Piryatinskiĭ, and V. A. Semenovich

Institute of Semiconductor Physics, Ukrainian National Academy of Sciences, Kiev, Ukraine; Institute of Physics, Ukrainian National Academy of Sciences, Kiev, Ukraine
(Submitted October 29, 1998)
Pis'ma Zh. Tekh. Fiz. **25**, 27–32 (April 26, 1999)

The influence of rapid thermal annealing on the photoluminescence properties of porous-silicon/diamondlike-carbon-film structures is investigated. Redistribution of the radiation from the long-wavelength to the short-wavelength region is discovered. Models of the processes observed are presented. © *1999 American Institute of Physics.* [S1063-7850(99)02004-2]

The intense photoluminescence (PL) characteristic of the visible emission region of porous silicon (PS) has aroused enormous interest in this material.[1] Despite the considerable amount of research that has been performed, there are still some open questions. They pertain primarily to the mechanisms of PL and the degradation of its intensity. The studies exploring the influence of various surface treatments on stabilization of the optical properties of porous Si are of special interest.[2,3] The results in Refs. 4 and 5 attest to the prospects of using various forms of carbon as a modifying material. At the same time, the research aimed at studying the influence of thermal treatments on the surface layer of porous Si is interesting. Shin *et al.*[6] showed that oxygen annealing at $T = 1100$ K for $t = 200$ s causes PL quenching, while annealing in an argon atmosphere ($T = 1100$ K and $t = 60$ s) causes a red shift of the PL peak (~150 nm) and a significant drop in its intensity.[7]

In the present work time-resolved PL methods were used to investigate the dynamics of the PL spectra of porous-silicon/diamondlike-carbon-film (PS/DLC-film) structures subjected to rapid thermal annealing at $T = 1100$ K in an inert atmosphere. Fairly intense PL is still observed after such anneals.

The samples of porous Si were obtained via the usual procedure for the electrochemical etching of silicon. Wafers of *p*-Si(100) with a resistivity equal to 10 $\Omega \times$cm (KDB-10) were used. An aluminum ohmic contact was deposited on the rear side of the wafers before preparing porous Si, and the porous Si layers were formed in a Teflon cell with a platinum electrode. The etching was carried out in the dark in a 48% HF:C_2H_5OH solution with a 1:1 component ratio. The porous Si samples were prepared with a current density equal to 50 mA/cm^2 and etching times equal to 5 min.

The diamondlike carbon films were deposited from the plasma of a capacitive rf discharge (13.56 MHz) at a low pressure (0.8 Torr) with the substrate at room temperature (300 K). A CH_4:H_2:N_2 gas mixture with a 10% nitrogen content was used. During the deposition process the substrate was under an rf potential equal to 1900 V. The thicknesses of the diamondlike carbon films were measured on an LÉF-3M laser ellipsometer at a wavelength of 632.8 nm and varied in the range 50–100 nm.

The samples were annealed in a rapid thermal annealing system in an argon atmosphere at 1100 K for 30 s.

Photoluminescence was excited by a nitrogen laser ($\lambda = 337.1$ nm) with a duration of the exciting pulse equal to 10 nm and a pulse power equal to 5 kW. A stroboscopic detection system capable of recording PL spectra with a time delay and investigating the kinetics of their variation was employed. The PL spectra were recorded with nanosecond and microsecond time delays relative to the maximum of the laser pulse at room temperature.

Figure 1a shows the PL spectra of the original samples of porous Si, a diamondlike carbon film on silicon, and a PS/DLC-film structure before thermal treatments. As can be seen (Fig. 1a, curves *1–2*), the deposition of a diamondlike carbon film on a porous Si surface causes a small blue shift of the integrated PL spectra from 675 nm (porous Si, curve *1*) to 650 nm (PS/DLC-film, curve *2*). Curve *3* (Fig. 1a) is the nanosecond PL spectrum of a diamondlike carbon film deposited on polished silicon. This spectrum is similar to the PL spectrum of finely dispersed diamonds.[8] The dominant feature in the spectrum is the emission peak at 440 nm, which can be assigned to the luminescence of diamondlike (sp^3) carbon formations. Curves *4* and *5* (Fig. 1a) are the nanosecond PL spectra of porous Si and a PS/DLC-film structure, respectively. A comparison of the nanosecond spectra reveals that the nanosecond spectrum of the PS/DLC-film system is the result of the superposition of the nanosecond PL spectra of porous Si (with a peak at ~550 nm), nanoclusters of diamondlike carbon in silicon pores (with a peak at ~470 nm), and their interaction products on the PS/DLC-film interface.

Figure 2 presents the PL spectra of porous Si and PS/DLC-film samples measured with microsecond time resolution. Curves *1*, *2*, and *3* correspond to the PL spectra of the original porous Si measured with time delays of 0, 5, and 15 μs. A comparison of the integrated PL spectrum (Fig. 1a, curve *1*) with the microsecond spectra (Fig. 2, curves *1*, *2*, and *3*) shows that the PL peak shifts from 690 nm in the integrated spectrum to 630 nm in the microsecond spectrum. As the delay time is increased from 0 to 15 μs, a red shift to 650 μm is observed. These spectral changes are characteristic of manifestations of a quantum-size effect,[9] which results
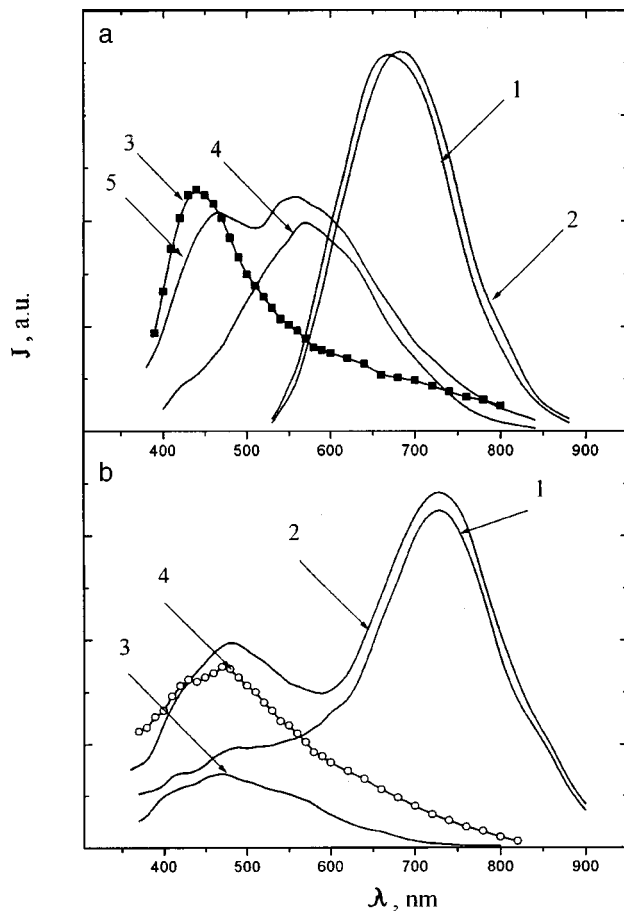
FIG. 1. a — Photoluminescence spectra of the systems before thermal treatments: *1* — integrated spectrum of the original porous Si, *2* — integrated spectrum of the PS/DLC-film system, *3* — nanosecond spectrum of a diamondlike carbon film on polished silicon, *4* — nanosecond spectrum of porous Si, *5* — nanosecond spectrum of the PS/DLC-film system. The intensity of curves *3*, *4*, and *5* has been enhanced by a factor of 17. b — Photoluminescence spectra of the systems after rapid thermal annealing in an argon atmosphere at $T = 1100$ K for 30 s: *1* — integrated spectrum of the porous Si, *2* — integrated spectrum of the PS/DLC-film system, *3* — nanosecond spectrum of porous Si, *4* — nanosecond spectrum of the PS/DLC-film system.

FIG. 2. Photoluminescence spectra of the systems measured with microsecond resolution: *1*, *2*, *3* — spectra of the original porous Si with time delays equal to 0, 5, and 15μs, respectively; *4*, *5*, *6* — spectra of PS/DLC-film structures with time delays equal to 0, 5, and 15 μs; *7*, *8*, *9* — spectra of PS/DLC-film structures with time delays equal to 0, 5, and 15 μs after rapid thermal annealing in an argon atmosphere at $T = 1100$ K for 30 s. The intensity of curves *7*, *8*, and *9* has been enhanced by a factor of 16.

from redistribution of the emission from quantum filaments of small diameter to filaments of larger diameter because of the difference between the lifetimes of the excited states. The microsecond spectra of the PS/DLC-film system (Fig. 2, curves *4–6*) exhibit a ~10-nm blue shift relative to the corresponding microsecond spectra of porous Si. Note the small drop in the PL intensity for the PS/DLC-film structures relative to the PL intensity of the original samples observed when the delay time is increased.

Curves *7*, *8*, and *9* (Fig. 2) are the microwave PL spectra of PS/DLC-film samples subjected to rapid thermal annealing (RTA) at $T = 1100$ K for $t = 30$ s. As a result of the RTA treatments, the spectral lines in the microsecond component of the original porous Si are redistributed. The intensity of the microsecond PL component for the PS/DLC-film samples drops by a factor of 16. This drop is accompanied by a red shift of the PL peaks of the PS/DLC-film structures amounting to ~120 nm.

As has been reported,[9,10] porous Si has a layered structure, which is manifested by redistribution of the filament diameters from smaller values near the surface to larger values in the inner layers. The lowest layer of porous Si (with filaments of the largest diameter) is more protected by a diamondlike carbon film. The properties of these filaments are modified only slightly by RTA, while the surface filaments of small diameter lose their emissivity during thermal annealing. As a result, luminescence from the lower arrays with filaments of larger diameter is observed. Consequently, the emission in the microsecond spectrum is redistributed from the vicinity of ~610 nm for the untreated PS/DLC-film samples to 730 nm after the RTA treatments. In a certain sense, these findings confirm the influence of the quantum-size effect on the PL.

The hypotheses under consideration are confirmed by measuring the integrated and nanosecond spectra of porous Si and PS/DLC-film samples subjected to RTA. The integrated spectrum of the original porous Si (Fig. 1b, curve *1*) contains an intense band in the vicinity of 720 nm and less intense luminescence at 420–500 nm. The integrated spectrum of the PS/DLC-film system (Fig. 1b, curve *2*) also contains emission at 720 nm, which is associated with the microsecond luminescence of porous Si. At the same time, there is a sharp increase in PL with the formation of a peak at 470 nm, which is characteristic of the luminescence of Si–C compounds.[11] According to the foregoing arguments, this peak is presumably caused by the participation of Si–C formations and, probably, the porous-Si/diamondlike-carbon-film interface in the emission processes. These conclusions are based on an analysis of the nanosecond spectra of porous Si (curve *3*, Fig. 1b) and the PS/DLC-film system (curve *4*, Fig. 1b). Evidently, the nanosecond PL spectra of porous Si

at 450–500 nm are approximately 2.5 times less intense than those of the PS/DLC-film system.

The results obtained allow us to draw the following conclusions:

1. The deposition of thin layers of diamondlike carbon on a porous Si surface gives rise to interaction products of the porous Si and the diamondlike carbon film in the near-surface region of the porous Si.

2. RTA treatments may modify the near-surface layer of porous Si with the formation of Si–C compounds. As a result, stable emission is observed in the long-wavelength region for the luminescence of thermally stable porous Si filaments of large diameter, as well as in the short-wavelength region for the emission of Si–C compounds.

[1] L. T. Canham, Appl. Phys. Lett. **57**, 1046 (1990).

[2] V. Pellegrini, F. Fuso, G. Lorenzi *et al.*, Appl. Phys. Lett. **67**, 1084 (1995).

[3] P. Ziemianski and J. Misiewicz, Electron Tech. **30**, 277 (1997).

[4] Feng Yan, Xi-Mao Bao, Xiao-Wei Wu *et al.*, Appl. Phys. Lett. **67**, 3471 (1995).

[5] Yu. P. Piryatinskii, V. A. Semenovich, N. I. Klyui *et al.*, J. Chem. Vap. Deposition **5**, 207 (1997).

[6] S. Shin, C. Tsai, K.-H. Li *et al.*, Appl. Phys. Lett. **60**, 633 (1992).

[7] S. M. Prokes, J. Appl. Phys. **73**, 407 (1992).

[8] M. E. Kompan, E. I. Terukov, S. K. Gordeev *et al.*, Fiz. Tverd. Tela (St. Petersburg) **39**, 2156 (1997) [Phys. Solid State **39**, 1928 (1997)].

[9] M. E. Kompan, I. Yu. Shabanov, V. I. Beklemyshin *et al.*, Fiz. Tekh. Poluprovodn. **30**, 1095 (1996) [Semiconductors **30**, 580 (1996)].

[10] E. V. Astrova, A. A. Lebedev, A. D. Remenyuk *et al.*, Fiz. Tekh. Poluprovodn. **28**, 493 (1994) [Semiconductors **28**, 302 (1994)].

[11] Xing-Long Wu, Feng Yan, Xi-Mao Bao *et al.*, Appl. Phys. Lett. **68**, 2091 (1996).

Translated by P. Shelnitz

Autostochastic system of coupled microwave generators

R. V. Belyaev, É. V. Kal'yanov, V. Ya. Kislov, B. E. Kyarginskiĭ, and M. N. Lebedev

Institute of Radio Engineering and Electronics, Russian Academy of Sciences (Fryazino Section)

Equations are presented describing a system of coupled generators, taking into account the feedback delay and time lag in each partial generator. The delay in the coupling elements between the generators is also taken into account. A numerical analysis of the dynamics of one, two, and three generators is performed. It is shown that chaotization of the oscillations occurs more readily in a coupled system of two or three generators than in the case of a single generator. This is confirmed by the results of experiments on transistor microwave generators. It is found that noise fluctuations can be obtained in a system of three coupled transistor generators over a broad range of frequencies in the centimeter wavelength range. © *1999 American Institute of Physics.* [S1063-7850(99)02104-7]

The familiar investigations of coupled autostochastic systems pertain mainly to the physics of the processes,[1–5] and experiments have been carried out at low frequencies.[2,5] At the same time, dynamic chaos is of interest for practical applications, particularly in communication systems.[6,7] Large-scale chaotic signals at microwave frequencies are of special interest for communications.[8] The production of such signals should become possible when the recent progress in the field of solid-state electronics associated with the promotion of transistors to the microwave range is utilized. This calls for an investigation of the possibility of creating broadband autostochastic microwave generators. This paper examines transistor microwave generators based on three coupled auto-oscillatory systems. A mathematical model is investigated, which reflects the properties of coupled microwave generators as faithfully as possible, and the results for an experimental autostochastic system of three coupled transistor generators are presented.

The equations of a system of many coupled generators with delay and a time lag including the coupling delay can be represented with consideration only of the capacitive coupling in the following manner:

$$\ddot{x}_i + \frac{\omega_i}{Q_i}\dot{x}_i + \omega_i^2 x_i = \omega_i^2 \left\{ B_i[1-(1-n_i)y_i^{n_i}] \right.$$

$$\times [x_i(t-\tau_i)-y_i]\delta_i^{-1}(1+y_i^{n_i})^{-2}$$

$$\left. + \sum_{j,j\neq i} C_{ji}x_j(t-T_{ji}) \right\},$$

$$\delta_i\dot{y}_i + y_i = x_i(t-\tau_i),$$

where $i,j=1,2,\ldots,k$, and k is the number of partial generators. Each partial generator consists of a nonlinear element, a first-order filter, a delay line, a second-order filter, and a differentiating element, which are assembled to form a ring. The following notation is used: δ_i is the time constant of the first-order filter, τ_i is the delay in the feedback loop, ω_i and Q_i are the resonant frequency and the Q factor of the second-order filter, C_{ji} are the coupling constants, T_{ji} are the coupling delay times, and B_i and n_i are constant coefficients which specify the gain of the respective partial generator in the ring and its nonlinearity, respectively. A dot over a letter denotes differentiation with respect to time.

In accordance with the experiment performed, we confine ourselves to the case where the partial generators differ only with respect to the values of the eigenfrequencies of the oscillatory systems and the gain coefficients. The remaining parameters are assumed to be identical, implying $C_{ji}=C$, $Q_i=Q$, $T_{ji}=\tau_i=\tau$, $n_i=n$, and $\delta_i=\delta$ (for the maximum value $k=3$). In this case Q, n, and δ are taken to be $Q=n=4$ and $\delta=0.1$.

In the case of one generator ($k=1$) the oscillatory process $x(t)$ depends significantly on the delay time τ. For example, if the resonant frequency $\omega=1$ and the gain coefficient lies in the interval $B \in [0,6]$, only regular oscillations occur for $\tau=1.25$. The excitation of oscillations (with a single-turn limit cycle) occurs when $B=1.2$. In the case of a large delay ($\tau=2$) chaotic oscillations appear when $B>4.4$. Oscillations are excited at once (when $B=2.2$) on the basis of a three-turn limit cycle without a regime of one-stroke oscillations.

In the case of two coupled generators the character of the oscillations depends on the value of the coupling parameter. In the case of the resonant frequencies $\omega_1=1$ and $\omega_2=2$ and the gain coefficients $B_1=B_2=5$, the transition to chaotic oscillations occurs when $\tau=1.25$, at which the coupling parameter reaches the value $C=0.2$. In the case of $\tau=2$, where a chaotic regime is realized autonomously in each of the partial generators, an increase in the coupling between the generators changes the character of the chaotic oscillations.

When three generators with different values for the eigenfrequencies of the partial oscillatory systems ($\omega_1=1$, $\omega_2=1.3$, and $\omega_3=1.1$) operate together, the value of the coupling parameter corresponding to chaotization of the os-
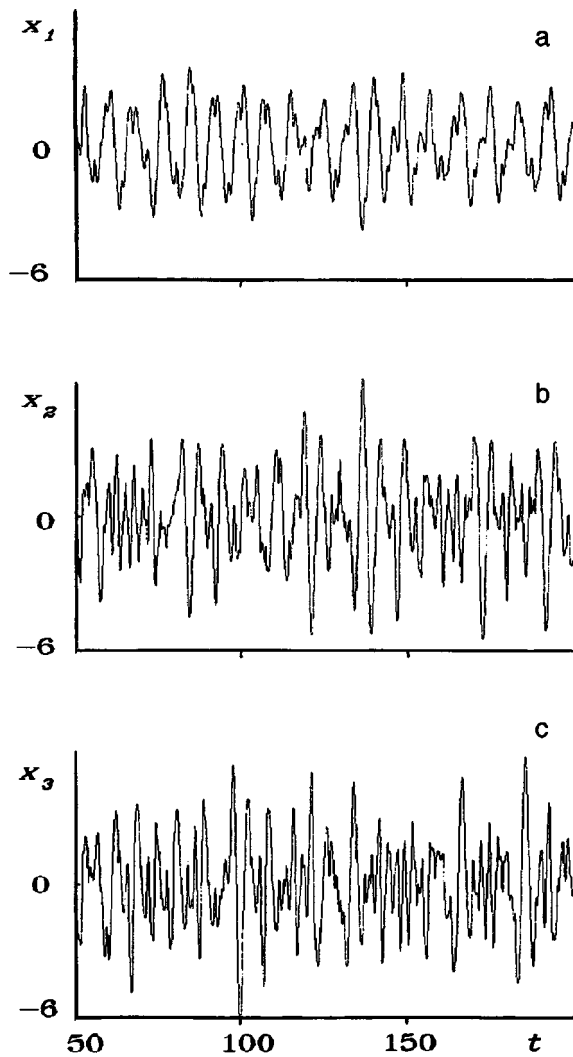
FIG. 1. Realization of oscillatory processes in partial generators for the case of the simultaneous operation of three coupled generators: a — first generator, b — second generator, c — third generator.

cillations for $\tau=1.25$ and $B_1=B_2=B_3=5$ is smaller than in the case of two generators. The chaotic regime persists when $\tau=2$.

Figure 1 presents realizations of the oscillatory processes $x_1(t)$, $x_2(t)$, and $x_3(t)$ obtained in the regime specified by $C=0.2$ for $\tau=2$. It follows from the realizations in Fig. 1 that the oscillatory processes in the different partial generators are not synchronized. It is also seen that the "mean" frequencies of the chaotic oscillations are different and increase in accordance with the values of the eigenfrequencies of the partial oscillatory systems.

The numerical analysis presented provides evidence that the appearance of more "developed" chaotic motions becomes possible as the number of interacting partial generators is increased. Therefore, we can anticipate the possibility of obtaining stable regimes of broad-band chaotic oscillations when a system of several coupled generators is created in practice.

An experimental investigation of a physical model was carried out in the centimeter range using microwave bipolar transistors and a standard microstrip technique. The microwave scheme included three coupled generators differing only with respect to their working frequencies. The oscillatory system of each generator consisted of segments of microstrip lines. The collector-base voltage U_{k-b} of the transistors was chosen as the control parameter in the experiments.

It was found experimentally that the width of the range of variation of the control parameter within which the generation of chaotic oscillations is realized increases as the number of generators included is increased from one to three. The spectral power density (S) of the chaotic oscillations generated is observed to become more uniform and and the spectrum becomes broader.

Figure 2 presents the spectrum of oscillations generated by the system in the centimeter range. The nonuniformity of the spectral power density of the noise in the 2–6 GHz band amounts to ~15 dB.

The results of the experimental investigations are consistent with the theoretical investigations. An autostochastic system which operates stably in a noise generation regime
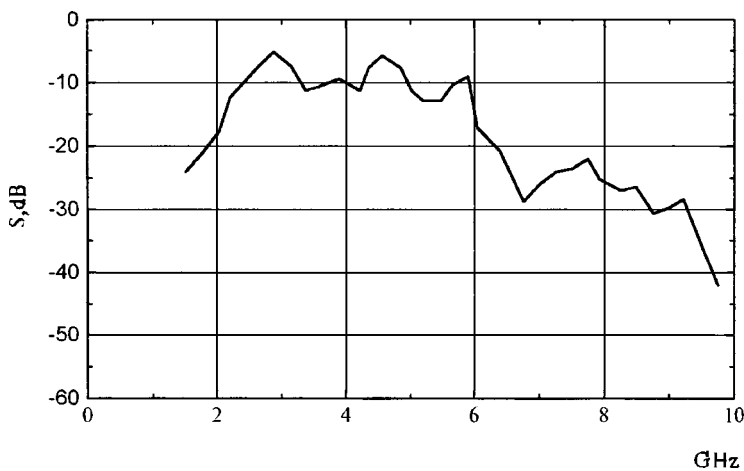
FIG. 2. Variation of the spectral power density of the chaotic oscillations generated as a function of frequency.

was created on the basis of three coupled generators.

The mathematical model of a system of coupled generators presented in this paper allows us to take into account the specific features of microwave generators. In both the mathematical and physical models chaotization of the oscillations in the coupled auto-oscillatory system occurs more readily as the degree of coupling is raised and the delay in the feedback loops of the partial generators is increased. A system of three coupled generators permits the realization of stable regimes of chaotic oscillations, which are not critical with respect to changes in the parameters.

[1] V. S. Afraĭmovich, N. N. Verichev, and M. I. Rabinovich, Izv. Vyssh. Uchebn. Zaved. Radiofiz. **29**, 1050 (1986).

[2] É. V. Kal'yanov and M. N. Lebedev, Radiotekh. Elektron. **8**, 1570 (1985).

[3] V. V. Astakhov, A. N. Sil'chenko, and G. I. Srelkova *et al.*, Radiotekh. Elektron. **41**, 1323 (1996).

[4] É. V. Kal'yanov, Radiotekh. Elektron. **41**, 575 (1996).

[5] V. S. Anishchenko, A. N. Sil'chenko, and I. A. Khovanov, Pis'ma Zh. Tekh. Fiz. **24**(7), 22 (1998) [Tech. Phys. Lett. **24**(4), 257 (1998)].

[6] V. Ya. Kislov, Radiotekh. Elektron. **38**, 1783 (1993).

[7] A. S. Dmitriev, A. I. Panas, and S. O. Starkov, Zarubezhn. Radioélektron., Usp. Sovrem. Radioélektron., **10**, 4 (1997).

[8] V. Ya. Kislov and V. V. Kislov, Radiotekh. Elektron. **42**, 982 (1997).

Translated by P. Shelnitz

Multiple-tip liquid-metal field emitter

O. P. Korovin, E. O. Popov, V. N. Shrednik, and S. S. Karatetskiĭ

A. F. Ioffe Physicotechnical Institute, Russian Academy of Sciences, St. Petersburg
(Submitted December 29, 1998)
Pis'ma Zh. Tekh. Fiz. **25**, 39–44 (April 26, 1999)

A stable field emitter with a large tip density (up to 10^8 cm^{-2}) has been created using track membrane technology. The emitter has been tested in various current collection regimes from a constant current to short pulses of nanosecond duration with a repetition frequency of several kilohertz. The high stability of the emission current at moderate electronic current densities up to 100 mA/cm^2 is attributed to the presence of a large number of emitting tips and the dynamic equilibrium between the repulsive forces of the electric field and the forces due to surface tension. © *1999 American Institute of Physics.* [S1063-7850(99)02204-1]

The results of investigations of liquid explosive electron emitters using tips have been widely discussed in the literature.[1–3] Less attention has been devoted to liquid-metal field emitters, probably because of the ease of the transition of the emission process from a field-emission regime to an explosive electron emission regime.[2]

This paper presents and discusses the results of an investigation of a multiple-tip liquid-metal emitter of a novel design, which operates stably in a field-emission regime. A polyethylene terephthalate track membrane, whose holes are filled with liquid gallium, is used to create the emitter. The gallium film has a common contact with the conductor on the rear side. The use of a track membrane permits the formation of an ensemble of tips with an *a priori* assigned density and ratio between the height and diameter of an individual emitter. The track membranes presently employed in selective clean-up filters are obtained by bombarding a film with heavy ions having an energy of several tens of megaelectron volts. After irradiation, the film is illuminated by ultraviolet light and subjected to chemical etching. The film thickness is usually 10 μm. The diameter of the holes can range from 0.3 to 1 μm, depending on the requirements. The density of the channels in the film can reach 10^8 cm^{-2}. The emitter area is restricted by the dimensions of the film and can, in principle, amount to tens of square meters.

Field emission was investigated in a diode structure with a flat anode. The anode-cathode distance in different experiments was 3–4 mm. In our experiments the cathode area was about 0.25 cm^2, and the channel density was 6×10^7 cm^{-2}. The channel diameter was 0.3–0.4 μm. A sinusoidal voltage U with a frequency of 50 Hz, 440 Hz, or 50 kHz, as well as a constant voltage, or short negative pulses of nanosecond duration were supplied to the cathode. The regimes with an alternating sinusoidal voltage $U(t)$ were investigated most thoroughly. It is these regimes which will be discussed in the present paper.

Figure 1a shows an oscillogram of the voltage U and the emission current I in one of the cases, in which the frequency of $U(t)$ was 440 Hz. The typical ''threshold'' behavior of appearing (and disappearing) field emission is observed. The amplitudes of $U(t)$ and $I(t)$ are relatively low in this case.

The maximum field intensity E achieved is insufficient for exciting an appreciable ion current due to field evaporation in the backward half-wave. The position of the $I(t)$ curve relative to $U(t)$ is symmetric. It was the same at 50 Hz and at 5×10^4 Hz, indicating the lack of a delay in the variation of the shape [in response to $U(t)$] of the emitting surface at the frequencies investigated. Figure 1b shows a typical current–voltage characteristic obtained from one of the positive voltage half-periods. The trace of the characteristic in Fig. 1b is nearly exponential.

Figure 2 reveals the stability of the emission current over long times. The mean spread of the current amplitude does not exceed 5%. The maximum currents collected could be increased to several milliamperes by increasing the voltage amplitude U_{max} without a loss of stability for a long time (hours).

A further increase in U_{max} led to a situation in which high current spikes appeared from time to time (more frequently as U_{max} increases) superposed on a background of stable periodic current pulses. The oscillograms revealed that the times of these high spikes are much shorter than the period of $U(t)$ or $I(t)$. We attribute these spikes to the excitation of explosive electron emission. We intend to describe these less stable regimes in greater detail later on. It is important to note that at values of U_{max} below the values corresponding to regimes with current spikes, field emission was stable and long-lived, yielding a current density averaged over a period greater than 0.1 A/cm^2. When infrequent spikes of explosive emission occurred, field emission was restored to its previous form with respect to all parameters after each spike. In contrast, multiple-tip systems of solid emitters operating in a field emission regime are known not to recover their former parameters after explosions of individual tips and gradually degrade.

Thus, the liquid-metal field-emission cathode under discussion is distinguished by its good stability and long lifetime at a moderate mean current density j in a vacuum with a residual pressure on the level of 10^{-6} Torr. Other advantages of such a good and delay-free cathode include the possibility of increasing its area and the possibility of employing essentially any cathode orientation and configuration. A film
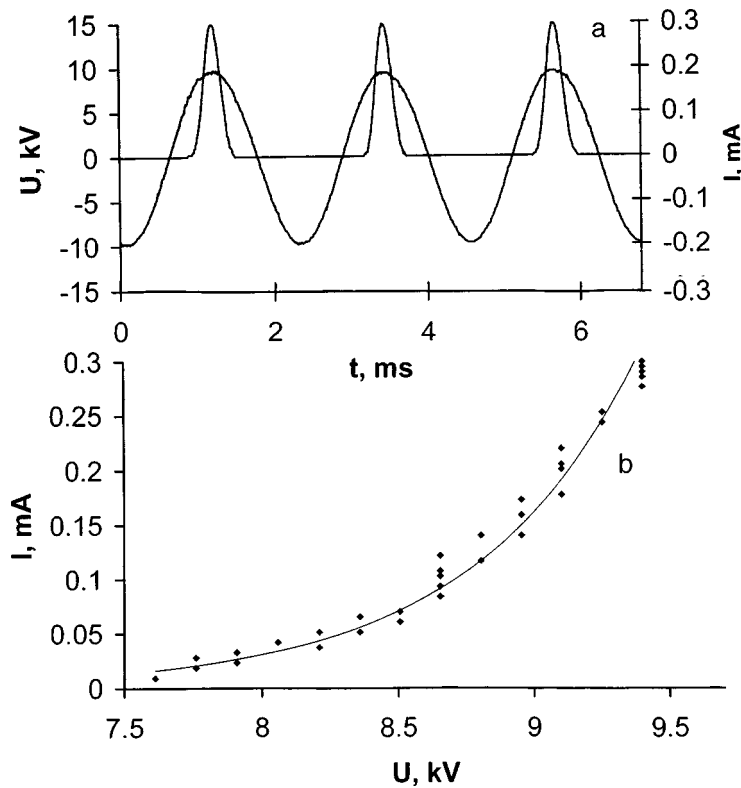
FIG. 1. Oscillogram of the voltage U and the emission current I (a) and current–voltage characteristic recorded using a computer and an analog-to-digital converter (b).

emitter can be either flat or bent into a ring, a tube, or a more complicated figure, as required.

It would be interesting to evaluate the parameters of individual tips and to explain the high reproducibility of the current in the cathode under discussion. The stability of emitters in regimes without explosions is due to negative feedback, which does not allow the tips to sharpen without bound or the emission current to grow without bound. In our case this feedback is most probably provided by the surface tension of the liquid, which tends to blunt the point of an individual tip. As $U(t)$ increases, the electric field intensity E at the rounded end of the gallium column increases. At some moment the electrostatic pressure of the field p_E (which draws and sharpens the emitters) becomes equal to the compressive pressure of the forces due to surface tension p_σ. Under the assumption that an individual emitter (tip) is a

solid of revolution and its end surface is a hemisphere of radius r, the conditions for equilibrium between p_E and p_σ give[4]

$$\frac{E_0^2}{8\pi} = \frac{2\sigma}{r_0},\tag{1}$$

where σ is the surface tension. The subscript 0 distinguishes the equilibrium field and radius. The equilibrium value E_0 from (1) equals

$$E_0 = 4\sqrt{\frac{\pi\sigma}{r_0}}.\tag{2}$$

The equality (1) holds at each moment in time. Measur-
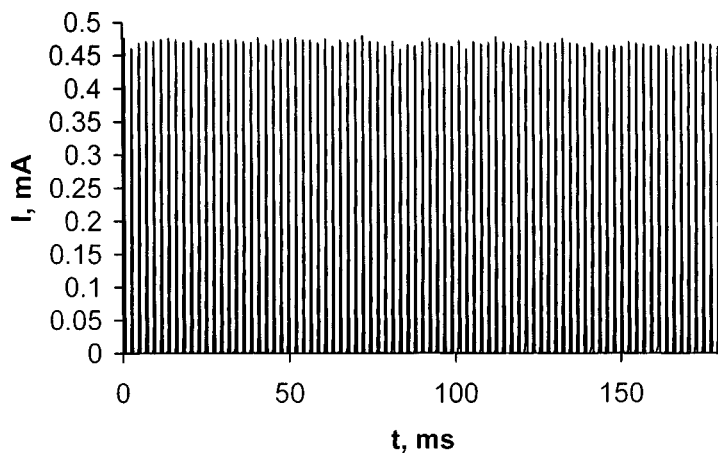
FIG. 2. Emission current as a function of time (each peak corresponds to a current pulse; see Fig. 1a).

ing E_0, σ, and r_0 in V/cm, N/cm, and angstroms, respectively, we rewrite (2) for gallium at room temperature [$\sigma = 7.12 \times 10^{-3}$ N/cm (Ref. 5)] in the form

$$E_0 = 56.76 \times 10^7 \frac{1}{\sqrt{r_0}}. \tag{3}$$

It is not difficult to calculate different values of E_0 in the range of values of r_0 of interest from formula (3). For an assigned value of E and the known work function $\varphi = 4$ eV for gallium[6] it is not difficult to find the relation between the field-emission current density j and r_0 using the formula for j in Ref. 7. If j is measured in A/cm^2 and r_0 in angstroms, we obtain

$$j = 1.766 \times 10^{13} \frac{1}{r_0} 10^{-0.3975 \sqrt{r_0}}. \tag{4}$$

Setting the emitting surface equal to r_0^2 (which is perfectly correct for an estimate), we can calculate the emission current I_0 from one tip, and if the number of working tips n is known (or somehow assigned) we can calculate the total current $I_0 n$ and compare it to the measured value.

The stable currents (without ''explosions'') had amplitudes below 15 mA. If we set n equal to 10^7, which is close to the highest possible value in our case, a current of 15 mA sustains tips with a radius of about 485 Å in equilibrium with respect to the forces of surface tension. In this case the current density $j \approx 64\ 6$A/cm^2 is relatively low for field emission. If $n = 10^6$ is assumed, an ensemble of tips with r_0 equal to about 370 Å and $j \approx 10^3$ A/cm^2 is required for a total current of about 15 mA. For $n < 10^6$ a further increase in j can lead to self-heating of the tips and to the development of explosive emission. Therefore, we assume that stable operation of our cathode is achieved for j no greater than 10^3 A/cm^2 and minimum radii of the ''pulsating'' tips in the range 350–500 Å.

Thus, the observed stable and reproducible emission of the cathode under discussion is attributed to the fact that a field-emission cathode with physically reliable negative feedback operates at values of the current density j that are relatively low for field emission. On the other hand, a significant total current is created by the large number (n) of simultaneously operating tips. In this case the problem of equalizing an ensemble of tips, which is significant for a solid-state cathode, does not exist. Liquid tips are equalized automatically as a result of capillary equilibrium, whose establishment is promoted by the small initial radius of the liquid column assigned by the small channel diameter.

[1] G. A. Mesyats and G. N. Furseĭ, in *Cold Cathodes* [in Russian], M. I. Elison (Ed.), Sov. Radio, Moscow (1974), pp. 284–286.

[2] G. N. Fursey, L. A. Shirochin, and L. M. Baskin, J. Vac. Sci. Technol. **15**, 410 (1997).

[3] G. N. Furseĭ and V. M. Zhukov, Zh. Tekh. Fiz. **44**, 1280 (1974) [Sov. Phys. Tech. Phys. **19**, 804 (1974)].

[4] C. Herring, *Structure and Properties of Solid Surface*, R. Gomer and C. S. Smith (Eds.), Chicago, University of Chicago Press (1953), pp. 5–72.

[5] *Chemical Encyclopedia* [in Russian], Sovetskaya Éntsiklopediya, (1988), Vol. 2, p. 479.

[6] V. S. Fomenko, *Electronic Properties of Materials. A Handbook* [in Russian], Naukova Dumka, Kiev (1984).

[7] V. N. Shrednik, in *Cold Cathodes* [in Russian], M. I. Elison (Ed.), Sov. Radio, Moscow (1974), pp. 166–169.

Translated by P. Shelnitz

Nature of the anomalous dispersion of particles in fullerite–alkali-metal-halide composites

V. A. Reznikov and A. A. Sukhanov

St. Petersburg State University, St. Petersburg
(Submitted December 26, 1998)
Pis'ma Zh. Tekh. Fiz. **25**, 45–49 (April 26, 1999)

The occurrence of a solid-phase reaction between powders of the fullerite C_{60} and potassium halides under the conditions of mechanical grinding is established. The electrostatic potential and surface-active properties of C_{60} molecules are considered as causes of the anomalously high degree of dispersion of the particles within a composite. © *1999 American Institute of Physics.* [S1063-7850(99)02304-6]

KBr–C_{60} composites are widely used to record the vibrational spectra of fullerene. The standard sample preparation method includes grinding the powders in a vibratory ball mill, in which a uniformly colored composite with linear dimensions of the particles equal to 3–5 μm forms during a period of 5–30 min.

When similar methods are used to disperse a coarse-grained K-Hal powder, the linear dimensions of the particles usually decrease to 20–50 μm, whereas the degree of dispersion of K-Hal particles achieved as a result of grinding together with C_{60} is characteristic of the use of disintegrators or electropulsing dispersion methods. It would be reasonable presumption that the inclusion of fullerite particles in the mixture promotes the increase in the degree of dispersion of K-Hal.

The occurrence of a reaction between the original components within the composite is indicated, in particular, by the water solubility of all of the composite material and the separation of a brown amorphized phase upon subsequent evaporation, which, according to x-ray fluorescence data, contains potassium and the halogen in equal concentrations. The amorphized phase can be extracted from the composite material by weakly polar organic solvents, for example, dichlorobenzene (DCB). Precipitation of the material upon evaporation of the solvent yields a fractally aggregated phase of K-Hal and reddish orange or reddish brown particles composed of carbon, which match the morphology of fullerite and fullerides. The volumetric concentration of the fullerite particles in the precipitate is 5–10% when the initial concentration of C_{60} within the composite is 1.0–1.5%.

In addition, at about 100–120 °C thermally induced recrystallization is manifested in compacted samples of the composites by the formation of black particles of cubic habit in KCl–C_{60} pellets and a surface ''growth'' of light brown octahedral crystals in KI–C_{60} pellets. Thermolysis of the KCl–C_{60} amorphized phase at $100-150$ °C or the KBr–C_{60} amorphized phase at $300-340$ °C yields equivalent volumetric concentrations of fullerite and K-Hal. A quantitative estimate of the mass of fullerite obtained as a result of thermal decomposition of the amorphized phase matches the original mass of fullerite in the composite or is 10–15% smaller.

The characteristic rate of the solid-phase interaction of polymorphous semiconductor materials (which include C_{60}) is about 10^{-8} cm/s and can rise in the region of a structural phase transition or as a result of an increase in the total area of the phase boundaries when the linear dimensions of the interacting particles are diminished.[1] The formation of a two-component amorphized phase during a period of order 10^2 s presupposes a decrease in the linear dimensions of the particles by a factor of $10^3 - 10^4$, which may be associated only with fullerite. A similar estimate of the size of the fullerite particles can be obtained from a model of the uniform coating by C_{60} molecules of K-Hal particles with linear dimensions of 3–5 μm when the initial relative concentration of fullerite is 1.0–1.5%.

The dispersion of fullerite to the molecular or supramolecular level during mechanical grinding together with a powdered dielectric indicates that there are several causes of fracture of the particles.

The formation of aqueous dispersions of C_{60} during the ultrasonic treatment of a fullerite powder in water has been reported.[2] It can occur as a result of cavitation on the particle surfaces, as well as when current pulses pass due to the formation of local fields of high intensity on the gas–liquid interfaces (the Margulis effect). The stability of suspensions under these conditions can be specified by the polarization of π and $\pi-\sigma$ bonds[3] and the interaction of C_{60} with mobile H^+ and OH^- groups,[4,5] as well as the Coulomb adsorption of dipolar molecular complexes on the gas–liquid phase boundaries.

The electropulsing dispersion mechanism is confirmed by obtaining an optically transparent suspension of C_{60} particles that is stable for 10–25 h when powdered fullerite is subjected to electric pulses. The absorption spectrum of an aqueous suspension of C_{60} is distinguished from the spectra of C_{60} by redistribution of the intensity of the π band (334 nm) and the structured band at 450–650 nm in favor of the latter, which, according to Ref. 6, corresponds to enhancement of the intermolecular interactions as a result of cluster–cluster aggregation[7] and is confirmed by the fractal precipitation pattern with $D = 1.68$.

It would, therefore, be reasonable to postulate a decisive

role for electrostatic discharges in the dispersal of fullerite particles. This is indirectly indicated by the dependence of the dispersion efficiency on the moisture content of the K-Hal powder. A significant role in the structure of fullerite is played by the intermolecular electrostatic interaction, whose damping in an electric field unavoidably leads to higher mobility of the molecules.

The electropulsing model of the dispersal of fullerite particles in a mixture with dielectric particles was tested by introducing powdered AgI particles into a fullerite–K-Hal mixture, as well as by replacing the K-Hal powder by an AgI powder, which simulates Ag-Hal photographic-sensitivity centers and for which metallization has been established under the action of current pulses obtained as a result of an electrostatic separation of charges.[8,9] Similar mechanical treatment of K-Hal–AgI powders, including subsequent irradiation of the mixture, does not produce a photographic effect.

InAgI–C_{60} and KI–AgI–C_{60} composites, pronounced metallization of the AgI particles and an 8–12-fold decrease in their linear dimensions, as well as the formation of a similar colored amorphized phase, are observed. Subsequent irradiation of the AgI–C_{60} composites is accompanied by photolysis of the AgI particles. Within the crystallization model of the photoprocess in AgHal (Refs. 10 and 11), this result corresponds to the formation of a complex salt on the AgI surface, which performs the function of sensitivity centers. The relatively small decrease in the linear dimensions of the AgI particles in comparison to K-Hal can be attributed to an increase in the role of the covalent interaction and to the polymorphism of AgI, where fracture of the particles along the basal plane, i.e., a decrease in the concentration of surface macrodefects, is possible. It is thus reasonable to allow a decisive role for the fullerene molecules in the anomalously high degree of dispersion of the K-Hal particles and disintegration of their surfaces, where the latter follows from the excessive dissolution of K-Hal in DCB relative to the composition of the amorphized phase as a result of the aggregation of particles of molecular size around C_{60} molecules, which act as colloid-forming centers.

The energy expended on the straining and fracture of crystals as a result of the development of microcracks and scratches upon abrasion and impact decreases when they interact with surfactants (the Rebinder adsorption effect[12]), while disintegration of the surface of an ionic crystal can result from the directed diffusion of vacancies to the surface, as well as the adsorption of particles with a large dipole moment on the surface, which distort the distribution of the electron density in the local coordination environment. The known properties of C_{60} (see Refs. 3, 7, 13, and 14) allow us to regard them as the natural and main cause of the processes indicated. In particular, the polarity of K-Hal–C_{60} complexes follows from the dissolution of the amorphized phase in HCl, and polarization of the π-electronic subsystem of C_{60} on a K-Hal surface follows from the modification of the absorption spectrum of C_{60} molecules extracted from the KCl–C_{60} composite together with weakly bound KCl toward closer correspondence to the spectral features of C_{70} (the appearance of a band at 382 nm and quenching of the band at 407 nm, as well as a 200–280 meV hypsochromic shift of the long-wavelength structured band).

Thus, C_{60} particles of molecular size, which exhibit the properties of surfactants capable of breaking up an ionic crystal, form as a result of electromechanical grinding.

[1] A. R. West, *Solid State Chemistry and Its Applications*, Wiley, Chichester–New York (1984) [Russ. transl., Mir, Moscow (1988), Part 1, p. 555].

[2] N. O. Petrossyan, V. K. Klochkov, and G. V. Andrievsky, J. Chem. Soc., Faraday Trans. **93**, 4344 (1992).

[3] Yu. M. Shul'ga and A. S. Lobach, Fiz. Tverd. Tela (St. Petersburg) **35**, 1092 (1993) [Phys. Solid State **35**, 557 (1993)].

[4] A. G. Lipson and V. A. Kuznetsov, Zh. Tekh. Fiz. **66**(6), 26 (1996) [Tech. Phys. **41**, 535 (1996)].

[5] K. S. Suslik, Sci. Am. **260**(2), 62 (1989) [V Mire Nauki, **4**, 54 (1989)].

[6] M. A. Terekhin, N. Yu. Svechnikov, V. G. Stankevich et al., Opt. Spektrosk. **78**, 75 (1995) [Opt. Spectrosc. **78**, 66 (1995)].

[7] A. V. Eletskiĭ, Teplofiz. Vys. Temp. **34**, 308 (1996).

[8] V. A. Reznikov, Pis'ma Zh. Tekh. Fiz. **16**(1), 44 (1990) [Sov. Tech. Phys. Lett. **16**, 19 (1990)].

[9] V. A. Reznikov and A. L. Kartuzhanskiĭ, Pis'ma Zh. Tekh. Fiz. **17**(15), 45 (1991) [Sov. Tech. Phys. Lett. **17**(8), 551 (1991)].

[10] V. A. Voll, Zh. Tekh. Fiz. **64**(12), 115 (1994) [Tech. Phys. **39**, 1264 (1994)].

[11] V. A. Voll and O. A. Trofimov, Zh. Fiz. Khim. **70**, 323 (1996).

[12] V. I. Likhtman, E. D. Shchukin, and P. A. Rebinder, *Physicochemical Mechanics of Metals; Adsorption Phenomena in the Process of Deformation and Failure of Metals*, Israel Program for Scientific Translations, Jerusalem (1964) [Russ. original, Izd. Akad. Nauk SSSR, Moscow (1962), p. 363].

[13] V. V. Afrosimov, A. A. Bassilaev, and M. N. Panov, Zh. Tekh. Fiz. **66**(5), 10 (1996) [Tech. Phys. **41**, 412 (1996)].

[14] L. L. Gumanov, G. A. Volkov, A. V. Shastin, and B. L. Korsunskiĭ, Dokl. Ross. Akad. Nauk, No. 4, 814 (1996).

Translated by P. Shelnitz

Long-range gettering of microdefects in silicon single crystals during the formation of porous silicon layers on their surface and ion irradiation

V. A. Perevoshchikov and V. D. Skupov

Scientific-Research Physicotechnical Institute, N. I. Lobachevskiĭ Nizhniĭ Novgorod State University, Nizhniĭ Novgorod
(Submitted November 12, 1998)

Experimental data on the dissolution of microdefects in the near-surface regions of silicon single crystals during the electrochemical formation of porous silicon layers followed by argon-ion irradiation are presented. A decrease in the microdefect concentration is detected near the interface with porous silicon and near the opposite surface of the samples. © *1999 American Institute of Physics.* [S1063-7850(99)02404-0]

The purpose of the present work was to investigate the influence of the electrochemical formation of single-crystal–porous-silicon ($Si_m - Si_{por}$) structures and their subsequent irradiation by moderate-energy ions on the microdefect structure across the entire thickness of the substrates. The results of such measurements are important for a deeper understanding of the physical mechanisms of the formation of Si_{por} and the structural transformations in the entire $Si_m - Si_{por}$ system and are of fundamental importance for more complete practical implementation of the highly unique physicochemical properties of $Si_m - Si_{por}$ structures.[1-3]

The experiments were performed on structures formed by the anodic treatment of KDB-0.001 (001) silicon crystals of thickness 360 μm in a 1:1:2 (vol/vol) $HF:H_2O:C_2H_5OH$ solution at an anodic current density equal to 10 mA cm^{-2}. The surface of the original crystals was prepared by the usual technique.[3] The dislocation density in the original substrates was at most 4.1×10^2 cm^{-2}. The thicknesses of the Si_{por} layers with a porosity $C = 30 - 33\%$ were $d = 2$, 10, and 20 μm. The structures were irradiated from the side of the Si_{por} layer by 40-keV argon ions in a dose equal to 6.25×10^{16} cm^{-2}. Before the measurements, the porous silicon layers were removed in a 15% KOH solution. The distribution profile of the microdefect density across the thickness of the structures was constructed from selective chemical etching patterns obtained during layer-by-layer etching of the samples at the rate of 1 μm min^{-1} in a 1:2 (vol/vol) $HF:CrO_3$ solution. In each etching step the mean microdefect density N_{def} was calculated from the number of etching pits detected in at least 15 - 18 fields of view of a Neophot-32 microscope to within ±8% at the 0.90 confidence level.

Experimental distribution profiles of the microdefect density across the thickness of the structures before and after the formation of Si_{por} layers of different thickness are presented in Fig. 1. It can be seen that a decrease in the microdefect density occurs as a result of the electrochemical treatment both near the interface of the single crystal with the Si_{por} layer and near the opposite side of the substrate, i.e., it is manifested as long-range gettering.[4] The number of defects dissolved and the effective depths of the regions freed of them on both sides of the structures increase with increas-

ing thickness of the porous silicon layer. The influence of ion irradiation is illustrated in Fig. 2, which presents distribution profiles of the relative change in the defect density,

$$\delta N_{def} = N_{def}^0 - N_{def} / N_{def}^0,$$

where N_{def}^0 and N_{def} are the microdefect densities before and after irradiation. They clearly reveal, on the one hand, an enhancement of defect dissolution upon irradiation and, on the other hand, a nonmonotonic dependence of the efficiency of this process on the thickness of Si_{por}. The defect-dissolution-stimulating effect of irradiation weakens appreciably near the $Si_m - Si_{por}$ interface for Si_{por} thicknesses greater than 10 μm and near the opposite side of the structure at 2 μm.

According to Refs. 3–5, the formation of a transition region in $Si_m - Si_{por}$ structures and the dissolution of microdefects in dislocation-free silicon are caused by the interaction of components of the original impurity-defect composition with nonequilibrium vacancies appearing near the reaction surface when Si_m dissociates locally during the formation and subsequent irradiation of Si_{por}. Vacancies can also originate from the impurity atmospheres around microdefects, which are displaced from equilibrium by the sign-alternating mechanical stresses of the elastic waves generated in the zones where electrochemical reactions occur and the implanted ions are slowed.[4] The appearance of vacancies during the formation of Si_{por} is naturally associated with the presence of local active centers on the dissolving surface of Si_m, on which electrochemical reactions take place, primarily the formation of SiF_2 and the reduction of Si from it.

Let $U_{act.\,c.}$ be the energy of an active center, which is close to the total activation energy for the formation of Si_{por}, and let $T_{act.\,c.}$ be the local temperature of the crystal lattice at the site of formation of an active center, which is defined as $T_{act.\,c.} = U_{act.\,c.}/k$ (k is the Boltzmann constant). Then the vacancy flux is defined by the expression

$$I_\nu = \pi n_0 c \nu_0 \exp\left(-\frac{U_{act.c.}}{kT}\right) \exp\left(-\frac{E_{f\nu}^s}{kT_{act.c.}}\right).$$
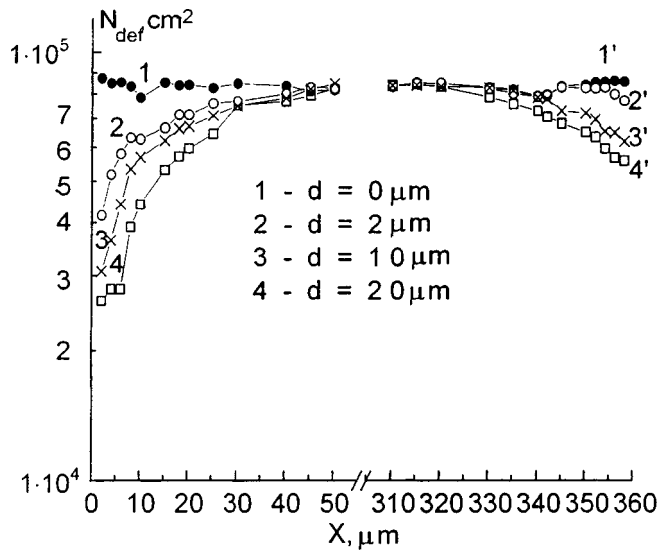
FIG. 1. Distribution profiles of the microdefect density across the thickness before (*1, 1'*) and after (*2, 2'; 3, 3'; 4, 4'*) the formation of porous silicon layers of various thickness; *2, 3, 4* — near the porous silicon layer; *2', 3', 4'* — near the opposite side of the samples.

Here n_0 is the density of Si atoms on the reaction surface (the reticular density); c is the bulk porosity of Si_{por}; ν_0 is the Debye frequency; and E_{fv}^s is the energy of formation of vacancies near the surface, which is almost 2.5 times smaller than the value in the bulk of the crystal.[6] Taking $n_0 \approx 1.4 \times 10^{15}$ cm^{-2}, $c \approx 0.3$, $\nu_0 \approx 10^{13}$ s^{-1}, $U_{act.c.} \approx 0.041$ eV (Ref. 1), and $E_{fv}^s \approx 1$ eV, we obtain $I_\nu \approx 6.4 \times 10^{16}$ cm^{-2} s^{-1}.

The decrease in the defect density near the opposite side of the structures, as in the case of ion irradiation,[3] is a result of the action of elastic waves.[5,7] The amplitude of elastic waves with an oscillation period τ propagating in a crystal at
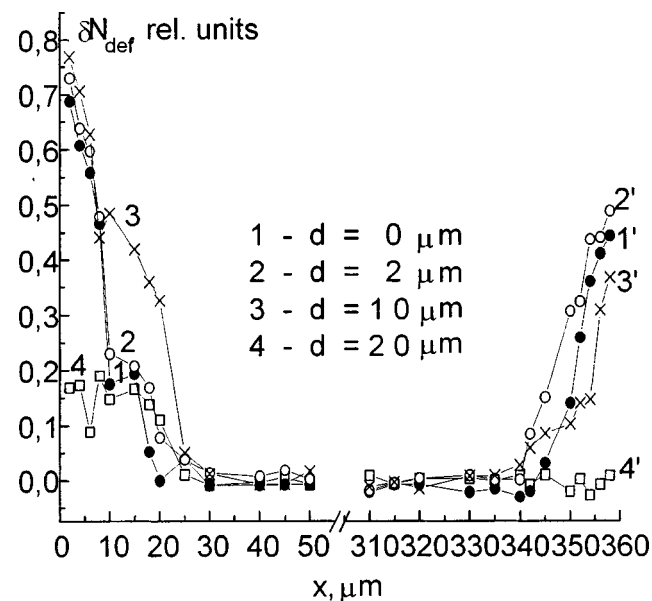
FIG. 2. Distribution profiles of the relative change in the microdefect density as a function of depth in irradiated structures from the side of the porous silicon layers of various thickness (curves *1, 2, 3,* and *4*) and from the opposite side of the samples (curves *1', 2', 3',* and *4'*).

distances from the $Si_m - Si_{por}$ interface satisfying the condition $z > (2\pi I_\nu \tau)^{-\frac{1}{2}}$ can be estimated from the relation[4,6]

$$P = \frac{4G\varepsilon a}{\alpha}(2\pi I_\nu \tau)^{\frac{1}{2}},$$

where ε is the lattice strain accompanying the appearance of a vacancy, α is the coordination number, $a \approx (\alpha\Omega)^{\frac{1}{3}}$ is the effective radius of the elastic wave source (Ω is the atomic volume), and G is the shear modulus. Setting $\tau = \nu_0^{-1} \times \exp(E_{m\nu}/kT)$, where $E_{m\nu}$ is the vacancy migration energy, and using known numerical values of the parameters for Si ($\varepsilon = 0.2$, $\alpha = 4$, and $E_{m\nu} = 0.33$ eV), for the amplitude of the waves on the opposite side of the structures we have $P \approx 4.3$ MPa. Waves with such an amplitude initiate the dissolution of microdefects by creating nonequilibrium vacancies when impurity atmospheres and surface sources are excited.[4,6]

The dissolution of microdefects is mediated not only by vacancies and waves generated by implanted ions, but also by vacancies appearing as a result of the dissociation of vacancy complexes present in single-crystal regions of the Si_{por} layers. The fact that such complexes appear during electrochemical treatment and are then partially ''burned off'' during irradiation is supported by the data from measuring the refractive index of Si_{por} layers on an LÉF-601 ellipsometer ($\lambda = 0.63$ μm). In the as-grown structures the mean value of the refractive index over the Si_{por} surface was 2.435 ± 0.004, and the value after irradiation was 2.709 ± 0.001, i.e., the density of the porous layer increased.[8] As the thickness of the Si_{por} layer increases, the role of sinks for point defects and the damping influence of pores on the propagation of surface waves becomes greater,[8] and the efficiency of long-range gettering consequently decreases (Fig. 2).

[1] V. A. Labunov, V. P. Bondarenko, and V. E. Borisenko, Zarubezhn. Élektron. Tekh., No. **15**, 3 (1978).

[2] L. T. Canham, Appl. Phys. Lett. **57**, 1046 (1990).

[3] A. V. Kulikov, V. A. Perevoshchikov, V. D. Skupov *et al.*, Pis'ma Zh. Tekh. Fiz. **23**(13), 27 (1997) [Tech. Phys. Lett. **23**(7), 507 (1997)].

[4] P. V. Pavlov, Yu. A. Semin, V. D. Skupov *et al.*, Fiz. Tekh. Poluprovodn. **20**, 503 (1986) [Sov. Phys. Semicond. **20**, 315 (1986)].

[5] V. A. Perevoshchikov, V. D. Skupov, and V. G. Shengurov, Poverkhnost'. Rentgenovskie, Sinkhrotron. Neĭtr. Issled., No. **4**, 44 (1998).

[6] V. P. Alekhin, *Physics of the Strength and Plasticity of Surface Layers of Materials* [in Russian], Nauka, Moscow (1983), 280 pp.

[7] O. N. Gorshkov, V. A. Perevoshchikov, and V. D. Skupov, Poverkhnost', No. **7**, 155 (1989).

[8] L. S. Palatnik, P. G. Cheremskoĭ, and M. Ya. Fuks, *Pores and Films* [in Russian], Énergoizdat, Moscow (1982), 216 pp.

Radiation effects in high-electron-mobility transistors

A. E. Rengevich

Institute of Semiconductor Physics, Ukrainian National Academy of Sciences, Kiev
(Submitted November 16, 1998)
Pis'ma Zh. Tekh. Fiz. **25**, 55–58 (April 26, 1999)

The influence of ^{60}Co γ radiation on the current–voltage characteristics of high electron mobility transistors is examined in the dose range from 1×10^4 to 6×10^8 R. No changes are observed up to a total dose of 1×10^7 R, but radiation-induced degradation of the transistors occurs when the dose exceeds 1×10^8 R. The possible causes of the effects observed are discussed. © *1999 American Institute of Physics.* [S1063-7850(99)02504-5]

Despite the abundance of information on radiation effects in gallium arsenide and semiconductor devices based on it, as well as the numerous data on the radiation stability of these materials, the information regarding the influence of radiation on the electrical characteristics of microwave field-effect transistors (FETs) with a Schottky barrier and, especially, high electron mobility transistors (HEMTs) is very limited.[1–3]

This paper examines the influence of ^{60}Co γ irradiation on the low-frequency current–voltage characteristics of HEMTs. The samples were irradiated in an MRX-γ-25M system with a beam intensity equal to 140 R/s in the dose range from 1×10^4 to 6×10^8 R. The temperature in the irradiation zone did not exceed $+40\,°$C. The typical structure of a high electron mobility transistor is shown in Fig. 1.

The measurements showed that in the dose range from 1×10^4 to 1×10^7 R the variation of the parameters is smaller than the instrumental error of the measuring unit (1%). Increasing the γ radiation dose to 1×10^8 R causes variation of the saturation current, slope, and cutoff voltage by no more than 10%. Then there are sharp changes in the parameters, and at a total dose of 6×10^8 R the departure of the parameters from the initial values amounts to $\approx40\%$. Typical dose-dependent changes in the saturation current (a), slope (b), and cutoff voltage (c) of HEMTs are shown as percentages relative to the unirradiated state in Fig. 2.

The samples investigated did not exhibit the expected significant advantage in radiation stability over transistors with a Schottky barrier. The relative changes in the parameters were comparable, but the HEMTs had better parameters for the slope and noise coefficient. At the same time, it is known that the changes in the parameters for similar HEMTs can be as large as 60% of the initial values already at a dose equal to 2×10^5 R.[4,5] The results obtained can be explained, if it is taken into account that the HEMTs and FETs with a Schottky barrier were found to have the same radiation stability.

Since the working layers of the transistors of both types contain gallium arsenide with a dopant concentration $\approx7\times10^{17}$ cm^{-3} and since, according to the experimental data in Ref. 6, the radiation-induced changes occurring in them under the action of ^{60}Co γ quanta appear at doses greater than 7×10^8 R, the effects observed in our experiment in the FETs both with a Schottky gate and with a high electron mobility cannot be attributed to radiation-induced changes in the gallium arsenide. At the same time, even at comparatively low γ radiation doses, the properties of barrier and ohmic contacts on gallium arsenide undergo significant changes associated with radiation-induced mass transport in the contacts, i.e., some ''sharpening'' of the distribution profile of the metal on the metal/GaAs interface (improvement of the parameters is associated with this effect), and with diffusive ''spreading'' of the barrier, which causes degradation phenomena in the contacts.[5] Qualitatively similar changes are observed when FETs are exposed to ^{60}Co γ quanta;[5] therefore, it can be assumed that the observed radiation-induced effects in the HEMTs are attributable to radiation-induced changes in the contacts.
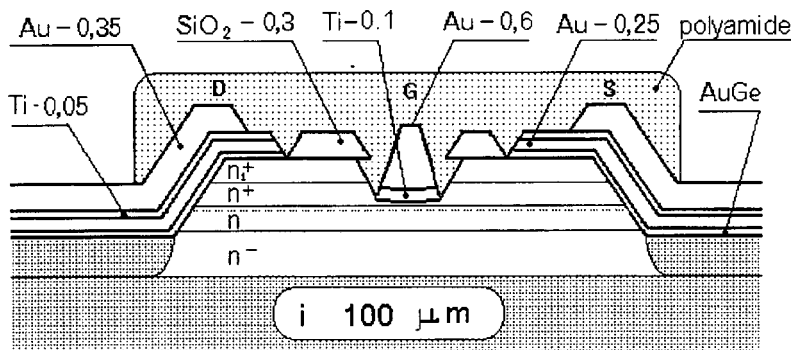
FIG. 1. Structure of field-effect transistors with a high electron mobility: n_1^+ GaAs, 1×10^{18} cm^{-3}, $d=0.5$ μm; n^+ GaAlAs, 1×10^{18} cm^{-3}, $d=0.35$ μm; SpGaAs, $d=0.02$ μm; n GaAs, 7×10^{17} cm^{-3}, $d=0.45$ μm; n^- GaAs, 1×10^{14} cm^{-3}, $d=1$ μm.
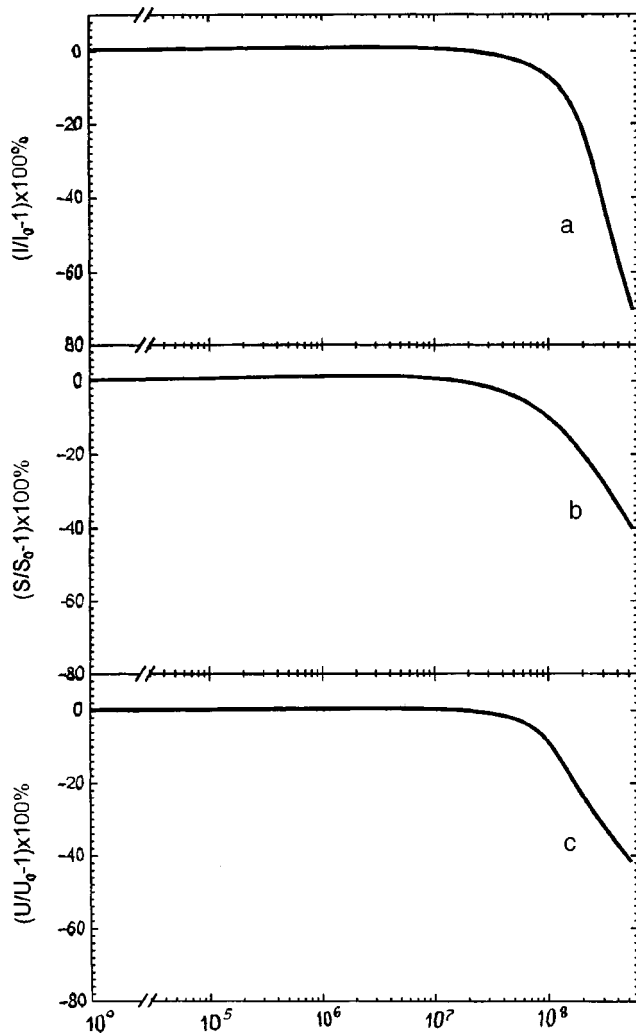
FIG. 2. Typical dose dependences of the saturation current (a), slope (b), and cutoff voltage (c) as percentages relative to the unirradiated state.

[1] R. Zuleeg, Proc. IEEE **777**(3), 389–470 (1989) [Tr. Inst. Inzh. Élektron. Radioélektron. **77**(3), 24–44 (1989)].

[2] S. V. Obolenskiĭ and G. P. Pavlov, Fiz. Tekh. Poluprovodn. **29**, 413 (1995) [Semiconductors **29**, 211 (1995)].

[3] N. V. Demarina and S. V. Obolenskiĭ, Zarubezhn. Radioélektron. No. 4, 66 (1997).

[4] E. F. Venger, I. Yu. Il'in, R. V. Konakova, G. S. Korotchenkov, V. V. Milenin, E. A. Solov'ev, A. E. Rengevich, E. V. Russu, and I. V. Prokopenko, in *Proceedings of the 8th International Crimean Conference on Microwave Techniques in Telecommunication Technologies* [in Russian], Veber Ukraina, Sevastopol' (1998), pp. 109–112.

[5] A. E. Belyaev, J. Breza, E. F. Venger, M. Vesely, I. Yu. Il'in, R. V. Konakova, J. Liday, V. G. Lyapin, V. V. Milenin, I. V. Prokopenko, and Yu. A. Tkhorik, *Radiation Resistance of GaAs-Based Microwave Schottky Barrier Devices. Some Physicotechnological Aspects*, Interpres Ltd., Kiev (1998), 128 pp.

[6] U. Yu. Braĭlovskiĭ, R. V. Konakova, B. P. Masenko, G. N. Semenova, Yu. A. Tkhorik, and V. I. Shakhovtsov, in *Radiation Effects in Solids* [in Russian], Nauk. Dumka, Kiev (1977), p. 180.

Translated by P. Shelnitz

Effect of anodic etching of heavily doped silicon on the location of the plasma minimum

V. B. Shuman

A. F. Ioffe Physicotechnical Institute, Russian Academy of Sciences, St. Petersburg

It is shown experimentally that the minimum in the reflectance spectrum of heavily doped *n*-Si shifts strongly toward lower frequencies when porous Si layers form on it. © *1999 American Institute of Physics.* [S1063-7850(99)02604-X]

Papers proposing the use of porous silicon layers as antireflection coatings on silicon solar cells have appeared in recent years. For example, in Ref. 1 anodizing was carried out without an external current source (as a result of the intrinsic photo-emf), in Ref. 2 it was carried out with an external source, and in Ref. 3 porous silicon layers were formed by stain etching. In these planar solar cells the porous silicon formed from a part of the emitter layer, which was a thin (less than 1 μm), heavily doped *p*- (Ref. 1) or *n*-type (Refs. 2 and 3) layer.

The reflectance spectrum of the surface of the degenerate semiconductor has a minimum in the infrared region at ω_p, whose position is determined by the free-carrier concentration, the effective mass, and the dielectric constant of the semiconductor.[4,5] Since the refractive index is lower in a porous silicon layer than in single-crystal silicon and depends mainly on its porosity,[6] it would be interesting to trace the variation of ω_p after anodizing heavily doped silicon.

The following types of silicon wafers were used to form porous silicon:

a) wafers of $\langle 111 \rangle$ orientation, which were uniformly doped during grown with arsenic or boron to a concentration $\sim 2.3 \times 10^{19}$ cm^{-3},

b) n^+nn^+ and p^+pp^+ structures obtained as a result of the diffusion of phosphorus or boron to a depth of 1.4 μm in lightly doped *n*- or *p*-Si, respectively.

The surface concentration of the impurities in the diffusion layers was estimated from Irvin's curves[7] and from the position of the plasma minimum,[5] both methods giving virtually identical values of $\sim 2.0 \times 10^{20}$ cm^{-3}. Silicon was anodized in a water–ethanol solution of HF (1:1:2) at current densities in the range 2–50 mA/cm^2. The thickness of the porous silicon layer was less than 1 μm. The spectral dependence of the reflection coefficient was determined using an IKS-29 spectrophotometer with an IPO-22 attachment in the range 4000–400 cm^{-1} at room temperature.

Appreciable displacement of the position of the plasma minimum is observed only after the anodizing of *n*-Si and n^+ diffusion layers. The dependence of the position of the plasma minimum on the charge Q flowing during the formation of a porous silicon layer on uniformly doped *n*-Si is shown in Fig. 1. After the formation of porous silicon, ω_p shifts toward lower frequencies. This shift depends linearly on the amount of charge Q and is essentially independent of anodic current density. The same trend is observed after the n^+ diffusion layers are anodized, i.e., the plasma minimum shifts toward lower frequencies. However, this shift is more significant, possibly because the doping level of the diffusion layers is almost an order of magnitude higher than in the case of silicon doped during growth. Thus, the shift for uniformly
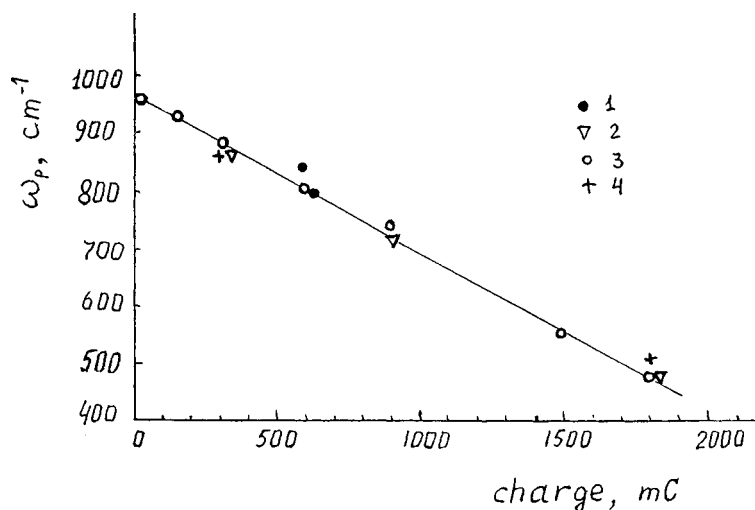
FIG. 1. Dependence of the frequency of the plasma minimum on the charge flowing during the anodizing of silicon with a donor concentration equal to 2.3×10^{19} cm^{-3}. Current density, mA/cm^2: *1* — 2, *2* — 5, *3* — 15, *4* — 50.

doped n-Si at $Q=500$ mC is $\Delta\omega_p \approx 130$ cm^{-1}, whereas for the diffusion layers on $\langle 111 \rangle$ wafers it is $\Delta\omega_p \approx 210$ cm^{-1} and for those on $\langle 100 \rangle$ wafers $\Delta\omega_p \approx 500$ cm^{-1}.

The experimental results presented show that this method can be used for the quick contactless nondestructive testing of the characteristics of porous silicon layers formed as antireflection coatings on the emitter layers of solar cells with an n^+pp^+ structure.

[1] A. Prasad, S. Balakrishnan, S. K. Jain, and G. C. Jain, J. Electrochem. Soc. **129**, 596 (1982).
[2] S. Strehlke, D. Sarti, A. Krotkus, K. Grigoras, and C. Levy–Clement, Thin Solid Films **297**, 291 (1997).
[3] L. Schirone, G. Sotgiu, and F. P. Califano, Thin Solid Films **297**, 296 (1997).
[4] W. G. Spitzer and H. Y. Fan, Phys. Rev. **10**, 882 (1957).
[5] E. E. Gardner, W. Kappallo, and C. R. Gordon, Appl. Phys. Lett. **9**, 432 (1966).
[6] R. W. Hardeman, M. I. J. Beale, D. B. Gasson, J. M. Keen, C. Pickering, and D. J. Robbins, Surf. Sci. **152/153**, 1051 (1985).
[7] J. C. Irvin, Bell Syst. Tech. J. **41**, 387 (1962).

Translated by P. Shelnitz

Investigation of a glow discharge in a mixture of Ar and OH

A. Ya. Vul', S. V. Kidalov, V. M. Milenin, N. A. Timofeev, and M. A. Khodorkovskiĭ

St. Petersburg State University; A. F. Ioffe Physicotechnical Institute, Russian Academy of Sciences, St. Petersburg; ''Applied Chemistry'' State Scientific Center
(Submitted December 24, 1998)
Pis'ma Zh. Tekh. Fiz. **25**, 62–66 (April 26, 1999)

A glow discharge in a mixture of argon and hydroxyl (OH) is investigated experimentally. It is shown that under certain discharge conditions a considerable portion of the electrical energy imparted to the discharge is used to generate resonant emission of OH molecules. The results obtained point to a realistic possibility of creating a new, ecologically friendly source of optical radiation, which can replace mercury lamps in the near future. © *1999 American Institute of Physics.* [S1063-7850(99)02704-4]

Most modern efficient low-pressure sources of optical radiation are based on discharges in mixtures of a readily ionizable impurity and a buffer (inert) gas.

Examples of such light sources include mercury lamps, low-pressure sodium light sources, light sources based on various metal vapors, etc.[1,2] It was shown in Ref. 3 that molecules of hydroxyl OH can serve as the readily ionizable impurity. The present work is a continuation of the research whose results were reported in Ref. 3.

The purpose of the present work was to study the optical and energy characteristics of a discharge in a mixture of Ar and OH formed as a result of the dissociation of water molecules under glow-discharge conditions and to evaluate the role of the elementary processes determining the properties of the plasma obtained. The investigations were carried out in a dc discharge and in a radio-frequency (rf) discharge excited by a 60-MHz electric field. The discharge was created in quartz tubes of various length (from 3 to 10 cm) and diameter (from 1.0 to 4.5 cm). The optical (intensities of spectral lines and bands in the range 200–800 nm) and energy (electric power imparted to the discharge and radiated power in several lines and the resonance band of OH at 306.4 nm) characteristics of an argon discharge with various concentrations of H_2O were measured. The pressure of the inert gas varied in the range 1–30 Torr. The current in the dc discharge varied from 50 to 500 mA, and the current in the rf discharge varied from 5 to 30 mA.

The experiments showed that the discharges of both
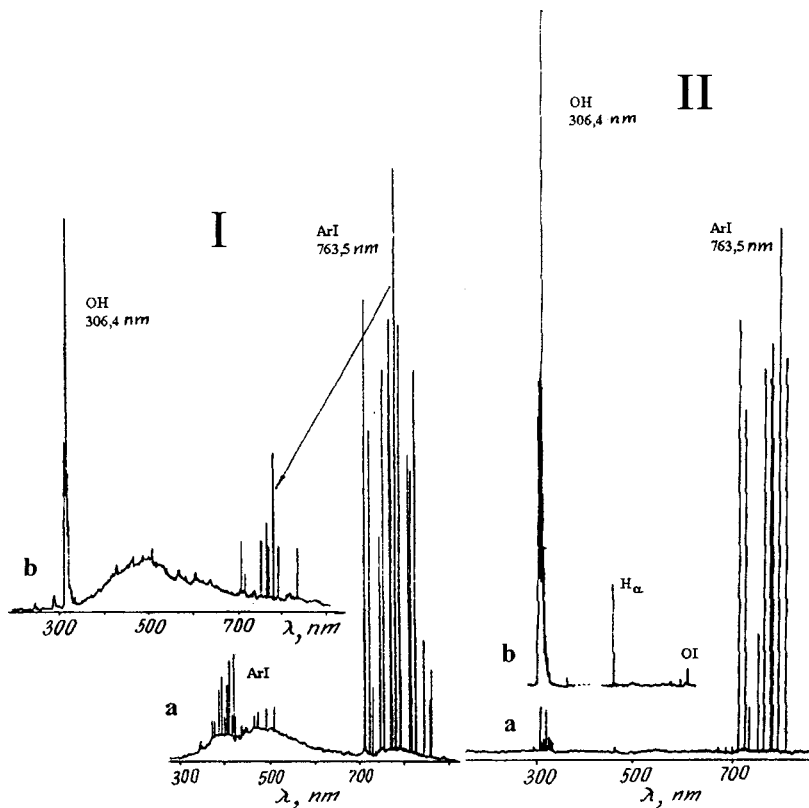
FIG. 1. Emission spectrum of the plasma of a dc discharge (I) and of an rf discharge (II): a — argon discharge, b — Ar+OH discharge.
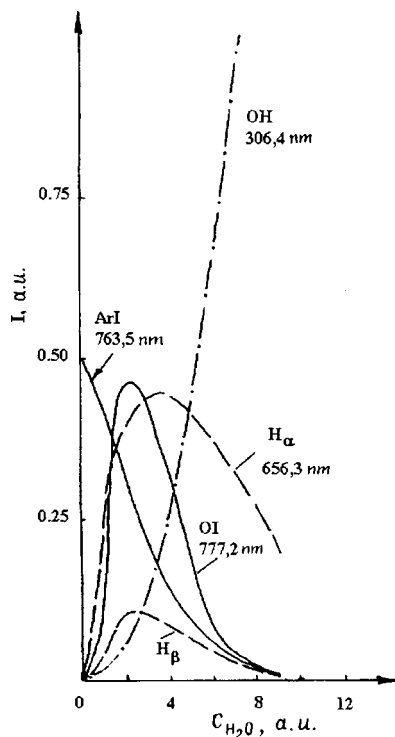
FIG. 2. Intensities of the lines of argon (763.5 nm), atomic oxygen (777.2 nm), and atomic hydrogen (656.3 nm and 486.1 nm) and the resonance band of OH (306.4 nm) as a function of the concentration of water molecules C_{H_2O} in the discharge chamber.

FIG. 3. Intensity of the resonance band of OH at 306.4 nm and of the H_{α} line at 656.3 nm as a function of the argon pressure. The concentration of water molecules is twice as large for the dashed curves as for the solid curves.

types, i.e., the rf capacitive discharge and the dc discharge, have very comparable optical and energy characteristics. Figure 1 presents the emission spectra of these two discharges in pure argon and in pure argon with comparable concentrations of H_2O molecules. It is seen that the pictures are qualitatively identical. This is evidence that the principal elementary and plasma chemical processes determining the properties of the plasma in the discharges under consideration are similar and that conditions under which the intensity of the resonance band of OH at 306.4 nm is far greater than the intensity of the other bands and lines can be achieved in both types of discharges.

As our experiments showed, variation of the concentration of water molecules strongly influences the optical characteristics of the plasma of an Ar+OH discharge. Figure 2 shows the intensities of several atomic lines observed in the discharge investigated [of argon at 763.5 nm, of atomic hydrogen at 656.3 nm and 486.1 nm (H_{α} and H_{β}), and of atomic oxygen at 777.2 nm] and the resonance band of OH as a function of the concentration of H_2O molecules. Emission from other possible products of the plasma chemical reactions (for example, molecular hydrogen) was not observed. It can be seen from the figure that at relatively small concentrations of water molecules an increase in their concentration causes a rapid increase in the intensities of the atomic lines of oxygen and hydrogen. The intensity of the argon lines in the visible portion of the spectrum decreases and rapidly drops below the intensity of the H_{α} line and the line of atomic oxygen at 777.2 nm, which reach their peak

values and then decrease as the concentration of H_2O rises. It is noteworthy that the intensity of the OI line at 777.2 nm decreases far more rapidly than the intensity of the hydrogen lines, although the latter have excitation energies which are appreciably higher (12.09 eV for H_{α} and 12.73 eV for H_{β}) than the excitation energy of the OI line at 777.2 nm (10.74 eV). This decrease can be attributed to a drop in the concentration of atomic oxygen as the dissociation product of the water molecules, since the channel producing atomic hydrogen and OH molecules probably begins to dominate at sufficiently large concentrations of H_2O. This conclusion is confirmed by the sharp increase in the intensity of the resonance band of OH at 306.4 nm.

Variation of the pressure of the inert gas also has an effect on the properties of the discharges investigated: an increase in the argon pressure causes an increase in the intensity of the resonance band of OH and improvement in the relation between the intensity of this band and the intensities of the emission from atomic oxygen and hydrogen. A further increase in the argon pressure may have a positive influence on the properties of the plasma (Fig. 3).

The energy efficiency of the emission of OH at 306.4 nm was evaluated by comparing the intensity of this emission with the emission of a mercury discharge, for which the absolute values of the intensity of most of the lines in the UV and visible portion of the spectrum are known.[1,4] The comparison revealed that the efficiency of the generation of the resonant emission of OH molecules at 306.4 nm by an Ar+OH discharge can be very high. Under the conditions investigated at least 25% of the electrical energy imparted to the discharge is used to generate this band.

[1] G. N. Rokhlin, *Discharge Light Sources* [in Russian], Énergoatomizdat, Moscow (1991), 720 pp.

[2] J. F. Waymouth, *Electric Discharge Lamps*, MIT Press (1971) [Russ. transl., Énergiya, Moscow (1966), 310 pp.].

[3] A. Ya. Vul', S. V. Kidalov, V. M. Milenin, N. A. Timofeev, and M. A. Khodorkovskiĭ, Pis'ma Zh. Tekh. Fiz. **25**(1), 10 (1999) [Tech. Phys. Lett. **25**, 4 (1999)].

[4] M. Koedam, A. A. Kruithof, and J. Riemens, Physica (Amsterdam) **29**, 565 (1963).

Translated by P. Shelnitz

Investigation of the electrochemical coupling coefficient of acoustic waves in thin potassium niobate plates

S. G. Joshi, B. D. Zaïtsev, I. E. Kuznetsova, and I. A. Borodina

Saratov Branch of the Institute of Radio Engineering and Electronics, Russian Academy of Sciences, Saratov; Marquette University, Milwaukee, WI 53210, U.S.A.

The characteristics of antisymmetric and symmetric Lamb waves, as well as quasi-shear-horizontal waves, propagating in thin potassium niobate plates are investigated theoretically. It is found that the square of the electromechanical coupling coefficient of acoustic waves in such plates can reach 100% in certain directions. The results obtained indicate that potassium niobate is a highly promising material for creating various acoustoelectronic devices. © *1999 American Institute of Physics.* [S1063-7850(99)02804-9]

The demand for various high-frequency and broad-band acoustic-wave devices has been continually growing in recent years in connection with efforts to improve electrical communication systems. One of the important parameters of such devices is the electromechanical coupling constant of acoustic waves. Among the most interesting materials is potassium niobate $KNbO_3$, which has very high piezoelectric, electro-optic, and nonlinear-optical coefficients.[1] It was shown in Ref. 2 that the square of the electromechanical coupling coefficient K^2 of Rayleigh surface waves in the X direction of a Y-cut $KNbO_3$ crystal has a value of 53%, which is roughly 10 times the corresponding value for $LiNbO_3$. It was discovered in recent studies[3,4] that the value of K^2 for acoustic waves propagating in thin plates is significantly greater than the value for surface waves.

In the present study we theoretically analyzed the characteristics of quasi-shear-horizontal waves and Lamb waves propagating in thin potassium niobate plates. The problem was solved using the standard equations of motion of an elastic medium, the Laplace equation, and the material equations for mechanical stresses and electric displacement. The waves propagated along the x_1 axis, and the x_3 axis was directed into the interior of the medium. The boundary conditions were the vanishing of the mechanical stresses and continuity of the electric potential and the normal component of the electric displacement on the free boundaries of the plate with free space.

The material constants of potassium niobate needed for the calculations were taken from Ref. 1. The system of equations derived, together with the boundary conditions, was solved by a well known method.[5]

These calculations yield the velocity and the square of the electromechanical coupling coefficient ($K^2 = 2\Delta V/V$) for the zero-order symmetric (S_0) and antisymmetric (A_0) Lamb waves and quasi-shear-horizontal (QSH) waves as functions of the propagation direction in X-, Y-, and Z-cut crystals for various thicknesses of the potassium niobate plate.

Figure 1 presents plots of the dependence of the velocities of A_0, S_0, and QSH waves on their propagation direction

for the most interesting cuts and various plate thicknesses. The Euler angles were determined by the method described in Ref. 6.

It was discovered for certain propagation directions that
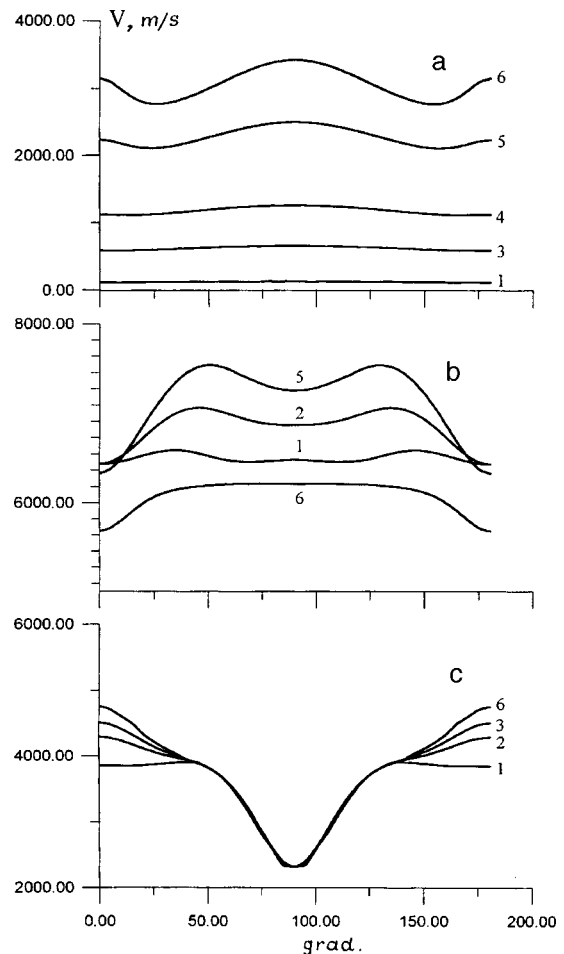
FIG. 1. Dependence of the velocity of acoustic waves on their propagation direction in a $KNbO_3$ plate for various plate thicknesses: a — A_0 wave propagating in a Z-cut crystal, b — S_0 wave, c — QSH wave propagating in a Y-cut crystal. *1* — $h/\lambda = 0.01$, *2* — $h/\lambda = 0.025$, *3* — $h/\lambda = 0.05$, *4* — $h/\lambda = 0.1$, *5* — $h/\lambda = 0.25$, *6* — $h/\lambda = 0.5$.
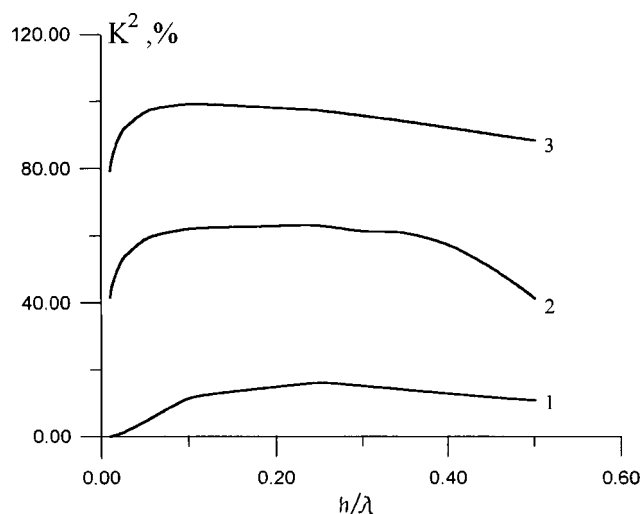
FIG. 2. Dependence of the square of the electromechanical coupling coefficient on the relative thickness of the KNbO$_3$ plate: *1* — A_0 wave ($\psi=0°$, Z-cut crystal), *2* — S_0 wave ($\phi=50°$, Y-cut crystal), *3* — QSH wave ($\phi=0°$, Y-cut crystal).

the square of the electromechanical coupling coefficient of the waves considered can reach extremely high values (up to 100%). Figure 2 presents the dependence of K^2 on the relative plate thickness h/λ (h is the plate thickness, and λ is the acoustic wavelength) for the propagation directions of A_0, S_0, and QSH waves characterized by the largest value.

The results obtained allow us to conclude that this material is highly promising for creating various acoustoelectronic devices. In addition, acoustic waves propagating in the thin plates can be utilized when such devices are operated in the low-frequency range, and surface waves can be utilized in the high-frequency range.

[1] M. Zgonik, R. Schlesser, I. Biaggio *et al.*, J. Appl. Phys. **74**, 1287 (1993).
[2] K. Yamanouchi, H. Odagawa, T. Kojima, and T. Matsunura, Electron. Lett. **33**, 193 (1997).
[3] S. G. Joshi and Y. Jin, Ultrasonics **34**, 507 (1996).
[4] B. D. Zaitsev, S. G. Joshi, and I. E. Kusnetsova, Smart Mater. Struct. **6**, 739 (1997).
[5] M. K. Balakirev and I. A. Gilinskiĭ, *Waves in Piezoelectric Crystals* [in Russian], Nauka, Novosibirsk (1982), 237 pp.
[6] V. A. Il'in and E. G. Poznyak, *Analytical Geometry* [in Russian], Nauka, Moscow (1968), 232 pp.

Translated by P. Shelnitz

Gas-sensitive properties of copper-containing fullerene membranes

V. F. Masterov, A. V. Prikhod'ko, O. I. Kon'kov, M. V. Shakhraĭ, and A. A. Shaklanov

St. Petersburg State Technical University; A. F. Ioffe Physicotechnical Institute, Russian Academy of Sciences, St. Petersburg

The gas-sensitive properties of copper-doped polycrystalline fullerene members are studied in the temperature range 280–360 K. The presence of isopropanol vapor in the surrounding air is found to increase the microwave absorption of the samples examined. The sensitivity of the samples is temperature-selective and depends on the relative orientation of the crystals, as well as the vector of the electric component of the electromagnetic microwave field.　© *1999 American Institute of Physics.* [S1063-7850(99)02904-3]

Semiconductor oxide materials are widely employed in the fabrication of gas sensors. Films of SnO_x have become widely employed.[1] In addition, thin films of copper-doped amorphous carbon have been investigated.[2] The gas-sensitive properties of thin fullerene films have also been investigated.[3] Their gas-sensitive properties are manifested as variation of the dc resistivity in the presence of various gases.

In the present work we investigated copper-containing fullerene membranes prepared according to the technology described in Ref. 4. Each such membrane is a polycrystal consisting of oriented single crystals of graded composition, which gradually varies along the growth axis from pure C_{60} on the substrate side to pure C_{70} on the opposite side. The mean copper concentration in the sample obtained is of the order of 10^{-3}% (Ref. 4). Figure 1 presents a general schematic view and a photograph of a membrane slice. The direction of the growth vector n is from I to II (the slice measures 2 mm in the I–II direction).

The microwave absorption of the sample was investigated at 41 GHz in gaseous media. The sample was placed in a waveguide module attached to the output of a G4-141 microwave generator. The module permitted cooling and heating of the sample in a gas atmosphere. The power P transmitted through the sample was recorded by an S4-27 spectrum analyzer. The measurements were performed with continuous heating of the sample in the temperature range 260–360 K at the rate of 10 K/min. During the measurements the sample was exposed to the gas five to eight times for 10–30 s. When a series of successive measurements was performed, the sample was cooled for 5 min to the initial temperature. The vapors formed when air was bubbled through liquid isopropanol (C_3H_7OH) served as the gas.

The measurements showed that in an atmosphere of isopropanol vapor the absorption of the microwave field by the sample increases relative to air $\Delta P = P_0 - P$ (where P_0 corresponds to air). The gas fed into the waveguide without the sample did not cause any change in the transmitted signal. Measurements were performed for two orientations of the

sample relative to the electric vector of the microwave field: with the growth axis of the single crystals (n) parallel and perpendicular to the vector of the electric component of the microwave field (E). Figure 2a presents plots of the tem-
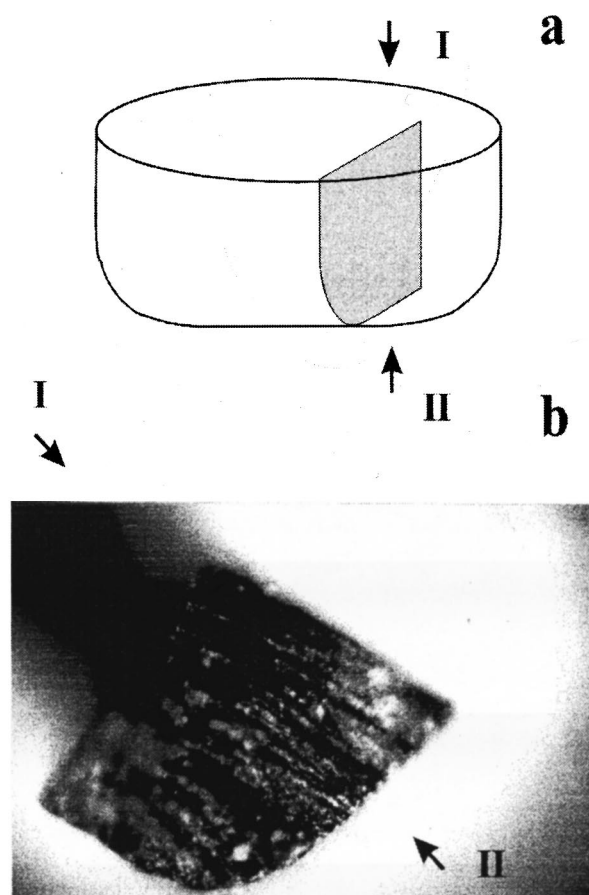
FIG. 1. Schematic view (a) and photograph of a membrane slice (b).
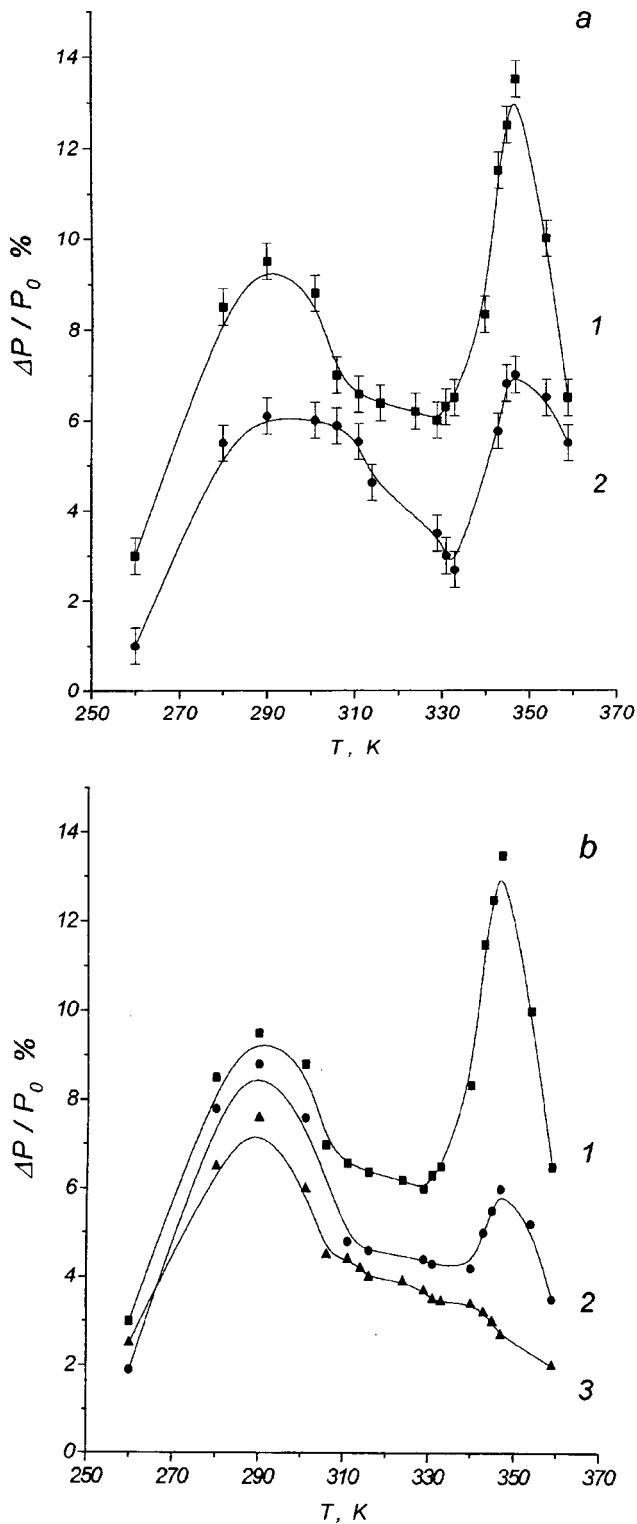
FIG. 2. a — Temperature dependence of the relative change in the signal transmitted $\Delta P/P_0$ for two sample orientations ($1 — n\|E, 2 — n\perp E$). b — Influence of thermal cycling on the gas-sensitive properties of a membrane: 1 — first thermal cycle, 2 — second thermal cycle, 3 — third thermal cycle.

perature dependence of the relative change $\Delta P/P_0$ in the transmitted signal (compared with air) in the range 260−360 K for two orientations of the sample ($1 — n\|E$, $2 — n\perp E$). It is seen that the sensitivity is $1.5−2$ times higher for the sample oriented parallel to the field. Subsequent measurements were performed for this orientation. A distinct sensitivity peak is detected at a temperature of about 350 K for both sample orientations. In addition, a weaker maximum is detected at 290 K.

The sample was investigated in a regime of successive measurements, in which it was repeatedly subjected to continuous heating and cooling back down to the initial temperature (thermal cycling). The results of these measurements are shown in Fig. 2b. The numbers $1–3$ correspond to the numbers of the successive heating cycles. The figure shows how the sensitivity peak at 350 K is gradually smoothed, while the other peak at 290 K remains stable. In the last measurement the sensitivity of the sample approaches 1% at 350 K.

The results obtained permit comparison of the gas-sensitive properties of the samples investigated with those already known. In the temperature range considered the sensitivity of the copper-containing fullerene membranes surpasses that of both pure and antimony-doped SnO_x thin films,[1] as well as both pure cupric oxide thin films and similar films doped with amorphous carbon.[2]

It can be theorized from a comparison with Ref. 2 that the sensitivity of samples similar to those considered will increase with increasing copper concentration.

[1] G. Gaggiotti, A. Galdikas, S. Kačiulis, G. Mattogno, and A. Šetkus, J. Appl. Phys. **76**, 4467 (1994).
[2] A. Galdikas, A. Mironas, A. Šetkus, L. Dapkus, V. Kazlauskiene, J. Miškinis, A. V. Prikhodko, and V. I. Ivanov-Omskii, Lithuan. J. Phys. **95**, 314 (1995).
[3] A. W. Synowczyk and J. Heinze, ''Application of fullerenes as sensor materials,'' in *Electronic Properties of Fullerenes (Series Solid State Science 117)*, H. Kuzmany, J. Fink, M. Mehring, and S. Roth (Eds.), Springer-Verlag, Berlin (1993), pp. 73–77.
[4] V. F. Masterov, A. V. Prikhod'ko, T. R. Stepanov, V. Yu. Davydov, and O. I. Kon'kov, Fiz. Tverd. Tela (St. Petersburg) **40**, 580 (1998) [Phys. Solid State **40**, 535 (1998)].

Translated by P. Shelnitz

Photovoltaic properties of semiconductor-protein heterocontacts

V. Yu. Rud', Yu. V. Rud', and V. Kh. Shpunt

St. Petersburg State Technical University; A. F. Ioffe Physicotechnical Institute, Russian Academy of Sciences, St. Petersburg
(Submitted May 15, 1998)
Pis'ma Zh. Tekh. Fiz. **25**, 76–80 (April 26, 1999)

It is found that heterocontacts consisting of a semiconductor (e.g., InSe) and a natural protein exhibit a broad-band photovoltaic effect and do not display an appreciable short-wavelength drop in the spectral range from 1.2 to 3.7 eV. The maximum photosensitivity of such structures, which reaches 2 mA/W at $T = 300$ K, is observed when they are illuminated on the protein side. It is concluded that the structures created can be employed as broad-band photosensors of optical radiation. © *1999 American Institute of Physics.*
[S1063-7850(99)03004-9]

The research on optoelectronic phenomena in heterostructures containing a direct contact between two semiconductors of different atomic composition or semiconductors with other media (a metal, electrolyte, living tissue, etc.) has been expanding continuously, providing for both improvement of the parameters of conventional semiconductor devices and the discovery of new functional relationships, which have initiated the development of new devices and systems.[1–5] This paper reports the first observation of a photovoltaic effect appearing when a semiconductor (e.g., InSe) is in contact with a natural protein.

The measurements of the photoelectric properties were performed on structures which were created by depositing a fresh natural protein on the surface of cleaved wafers of the layered semiconductor InSe with thicknesses from 10 to 50 μm and perfectly smooth planes. The indium selenide single crystals were electrically homogeneous with a free-electron density $n = 2 \times 10^{15}$ cm^{-3} and a Hall mobility of about 70 cm^2/(V·s) at $T = 300$ K. Transparent thin layers of metals (Ni, Mo) deposited by vacuum thermal sputtering onto quartz glass plates with thicknesses equal to $0.1 - 0.2$ mm served as electrical contacts to the protein. The final form of the structures was a semiconductor/liquid-protein/metallized-glass sandwich. To hold the components in place, an insulating varnish was applied to the metallized glass surface up to the perimeter of the InSe wafer. The varnish fixed the position of the semiconductor relative to the metal contact, preventing desiccation of the protein and precluding contact between the metal and the semiconductor. The protein filling the gap between the parallel planes of the InSe wafer and the metallized glass had a thickness of $0.05 - 0.1$ mm.

The measurements of the stationary current–voltage characteristics (IVC's) showed that the structures obtained in the manner indicated have a clear-up rectifying ability. A typical IVC of one of these structures is shown in Fig. 1. We note that the electrical parameters of the structures obtained did not display appreciable signs of degradation and that the transmission direction always corresponded to negative polarity of the external voltage at the semiconductor.

When the structures obtained are illuminated, a photovoltaic effect appears. Its sign does not vary in response to changes in the wavelength and the location of the light probe on the surface of the structures, but the magnitude of the photoresponse is greater when the structures are illuminated on the protein side. The photovoltage is characterized by negative polarity of the semiconductor in all the structures, in agreement with the transmission direction of the IVC. As the measurements showed, a short-circuit photocurrent in the InSe/protein structures flows in the transmission direction over the entire spectral region with photosensitivity. This means that the photosensitivity of the structures is determined only by processes on the semiconductor/protein interface. Therefore, the photogenerated charge carriers are separated in the electric field of this potential barrier, and a photovoltage consequently appears. The maximum current photosensitivity for the best structures is $S_I = 2$ mA/W, and the voltage photosensitivity is $S_U = 10^4$ V/W at $T = 300$ K. It can be assumed that optimization of the design of the structures will make it possible to surpass the parameters just cited, which even at this point can be regarded as fairly good, since this is the initial stage of the first investigations of a new generation of structures.
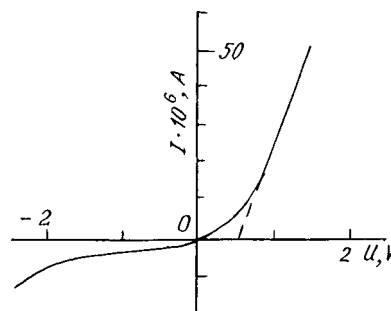
FIG. 1. Steady-state current–voltage characteristics of an n-InSe/protein structure at $T = 300$ K. (The transmission direction corresponds to negative polarity of an external bias voltage on the semiconductor plane and the contact area is $s = 0.1$ cm^2).
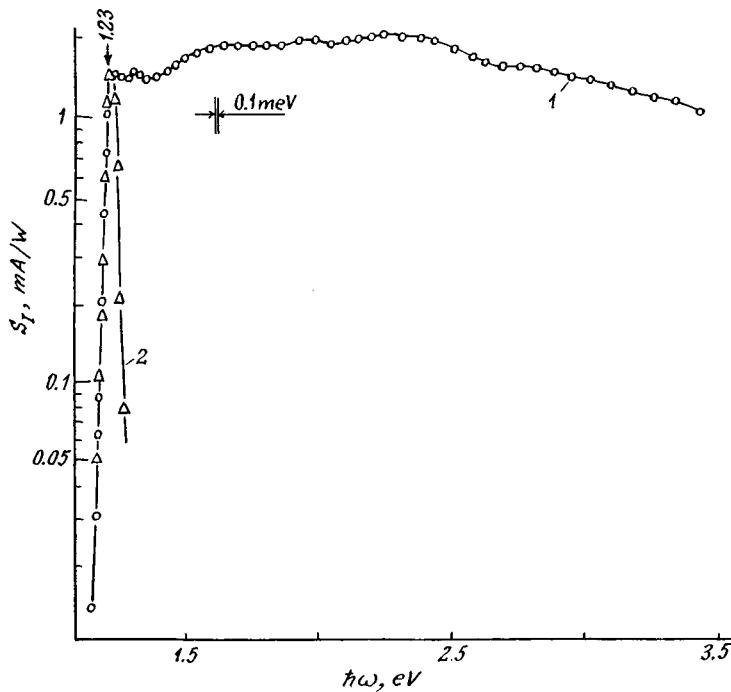
FIG. 2. Spectral dependence of the current photosensitivity of an *n*-InSe/protein structure at $T = 300$ K (*1* — illumination on the protein side, *2* — illumination on the semiconductor side).

A typical spectral dependence of the current photosensitivity, which is defined as the ratio of the short-circuit photocurrent to the number of incident photons, for one of the structures obtained is presented in Fig. 2. It follows from it that the window effect with respect to the intensity of natural light, which is characteristic of ideal heterojunctions,[1] is observed when the structure is illuminated on the protein side (Fig. 2, curve *1*), while an even sharper short-wavelength boundary appears on the spectral dependence when the structure is illuminated on the semiconductor side. Therefore, the photosensitivity becomes narrowly selective in such a photodetection geometry (the half-width of the spectra at half-maximum is $\delta_{1/2} = 30-40$ meV) due to the sharp increase in optical absorption in the InSe wafer when direct interband transitions take place and the layer of photogenerated carriers is separated from the active region of the structure by distances exceeding the diffusion length of photoholes in InSe. The slope of the long-wavelength exponential photosensitivity edge in the structures obtained $S_1 = 80$ eV^{-1} corresponds to direct optical transitions in the semiconductor, and the energetic position of the discontinuity at the photon energy $\hbar\omega = 1.23$ eV (Fig. 2, curve *1*) or the maximum at the same photon energy (curve *2*) is consistent with the value of the gap width of InSe and the features of the spectral dependence of the photosensitivity in other types of structures fabricated from the same semiconductor.[4-7] It can be assumed that the spectral dependence of the photosensitivity of the *n*-InSe/protein structures has the form characteristic of ideal semiconductor heterostructures.[1]

When the structures are illuminated on the protein side, the photosensitivity of the proposed heterostructures remains at a high level over a broad spectral range, and no appreciable short-wavelength drop in the photocurrent is observed up to 3.7 eV (Fig. 2, curve *1*). The full width at half-maximum of the S_I spectra reaches 2.2 eV in this case. Such a broad-band photovoltaic effect allows us to assign the role of the broad-band component in these structures to the protein. For the protein layer thicknesses used the absence of pronounced features in the spectral dependence of the photosensitivity also allows us to assume that the losses due to absorption in the broad-band window of these structures do not prevent their use as broad-band photoconverters of natural light. The absence of an appreciable short-wavelength drop in photosensitivity in these structures can also serve as a basis for concluding that such a heterocontact is of a high quality with respect to current transfer and the recombination of nonequilibrium charge carriers.

In conclusion, we stress that the photoelectric properties of semiconductor-protein heterocontacts have been found to be very close to the known properties of semiconductor-electrolyte contacts.[2,8] This similarity suggests that the role of the protein in photoelectric phenomena in such structures is similar to the role performed by classical electrolytes.[2] The higher viscosity of proteins and the absence of the corrosive effects on semiconductor surfaces inherent to electrolytes[2] favor applications of proteins in investigations of the photosensitivity of new materials for quickly creating such contacts and in the creation of photosensors. We also note the possibilities of studying the dynamics of processes in the proteins themselves using observations of the spectra of the photovoltaic effect when the heterocontacts are illuminated on the protein side.

Thus, as in the case of other substances of a biological nature,[4,5] a contact consisting of a semiconductor (e.g., InSe) and a protein displays a photovoltaic effect, which can be used to develop broad-band photosensors of optical radiation.

[1] Zh. I. Alferov, Fiz. Tekh. Poluprovodn. **32**, 3 (1998) [Semiconductors **32**, 1 (1998)].

[2] Yu. A. Gurevich and Yu. M. Pleskov, *Photoelectrochemical Semiconductors* [in Russian], Nauka, Moscow (1983).

[3] J. Simon and J.-J. Andre, *Molecular Semiconductors: Photoelectrical Properties and Solar Cells*, Springer-Verlag, Berlin–New York (1985) [Russ. transl., Mir, Moscow (1988)].

[4] V. Yu. Rud', Yu. V. Rud', and V. Kh. Shpunt, Fiz. Tekh. Poluprovodn. **29**, 438 (1995) [Semiconductors **29**, 225 (1995)].

[5] V. Yu. Rud', Yu. V. Rud', and V. Kh. Shpunt, Pis'ma Zh. Tekh. Fiz. **21**(3), 88 (1995) [Tech. Phys. Lett. **21**(2), 127 (1995)].

[6] I. V. Bondar', V. Yu. Rud', and Yu. V. Rud', Fiz. Tekh. Poluprovodn. **28**, 2137 (1994) [Semiconductors **28**, 1175 (1994)].

[7] I. V. Bodnar, V. Yu. Rud, and Yu. V. Rud, Cryst. Res. Technol. **31**, 261 (1996).

[8] N. N. Konstantinova, V. D. Prochukhan, Yu. V. Rud', and M. A. Tairov, Fiz. Tekh. Poluprovodn. **22**, 1699 (1988) [Sov. Phys. Semicond. **22**, 1072 (1988)].

Translated by P. Shelnitz

Optical properties of thin films of amorphous vanadium oxides

D. O. Kikalov, V. P. Malinenko, A. L. Pergament, and G. B. Stefanovich

Petrozavodsk State University
(Submitted October 12, 1998)
Pis'ma Zh. Tekh. Fiz. **25**, 81–87 (April 26, 1999)

The results of an experimental investigation of the optical properties of anodic vanadium oxide films are presented. It is shown that films of different phase composition (VO_2, V_2O_5, or a mixture of two phases) can be obtained, depending on the oxidation regime, and that the absorption and transmission spectra are modified significantly in accordance. The optical properties of the oxides, whose composition is close to stoichiometric vanadium dioxide, demonstrate the occurrence of a metal–semiconductor phase transition in the amorphous films. The results presented are important both from the standpoint of technical applications of thin film systems based on anodic vanadium oxides and for more detailed understanding of the physical mechanism of the metal–semiconductor phase transition and the influence of structural disorder on the transition. © *1999 American Institute of Physics.* [S1063-7850(99)03104-3]

The study of the optical properties of vanadium oxides is of considerable interest from the standpoint of various technical applications. In particular, the abrupt and reversible changes in the optical properties of vanadium dioxide associated with the metal-semiconductor phase transition together with the interference phenomena in thin films permit the use of this material as a reversible medium for recording and storing optical information, controllable mirrors with variable reflectivity, visualizers and detectors of IR and microwave radiation, and other devices.[1] In addition, the fabrication of highly sensitive efficient bolometers based on vanadium oxides, i.e., both VO_2 and the highest oxide (V_2O_5), as well as films composed of a mixture of VO_2 and V_2O_5 phases, was reported in Ref. 2. In the latter case it is possible to attain the unique combination of optical and electrical properties in a material needed to optimize the parameters of IR detectors. Amorphous V_2O_5 also displays an electrochromic effect,[3] which is utilized in electrochromic displays, controllable filters, and optical media with variable transmission (''smart windows'').[2]

One of the convenient methods for obtaining thin films of metal oxides is electrochemical (anodic) oxidation. As a rule, anodic oxide films are structurally disordered, and their stoichiometry (when transition metals with variable valence are oxidized) corresponds to the highest oxide. However, in the case of the anodic oxidation of vanadium, the phase composition of the oxide film has been identified in some studies as V_2O_5 and in others as VO_2 or a mixture of V_2O_5 with the lower oxides (see, for example, Ref. 3 and the references therein). Preliminary results, which show that the phase composition of the anodic oxide of vanadium can be controlled by selecting appropriate oxidation regimes and conditions (electrolyte composition, anodic current density, and oxidation time), i.e., that the oxygen stoichiometry of the oxide film can be varied from VO_2 to V_2O_5, were presented in Ref. 4.

This paper describes the results of an investigation of the optical properties of thin films of vanadium oxides. The samples investigated were obtained by anodically oxidizing vacuum-deposited layers of metallic vanadium on quartz, glass, and glass-ceramic substrates. Two different oxidation regimes[4] were used, and two types of samples were accordingly obtained: essentially stoichiometric VO_2 (type I) and films with an increased content of the V_2O_5 phase (type II). The transmittance T and the reflectance R were measured spectrophotometrically in the range from $\lambda = 300$ to 2000 nm.

Figure 1 presents the transmission spectra of four samples obtained under different conditions. Just as in the case of many applications in optical devices, films on transparent substrates are needed to measure T. This means that during the anodizing the vanadium layer must be oxidized down to the substrate. It turned out, however, that in this case the composition of the anodic oxide corresponds mainly to the highest oxidation number of vanadium (V_2O_5), regardless of the oxidation regime employed, i.e., regardless of whether a film of type I or type II is obtained. The presence of a considerable quantity of vanadium pentoxide is also evidenced both by the electrophysical properties of such samples (the relatively high resistivity and the absence of a metal–semiconductor phase transition) and by the $T(h\nu)$ curve. The latter exhibits a sharp drop in transmission in the region between 2 and 2.5 eV (curve *1* in Fig. 1), which corresponds to the fundamental absorption edge of V_2O_5 (Ref. 5).

This effect clearly occurs because further oxidation of the lower oxides to V_2O_5 in the growing anodic oxide takes place when it reaches the boundary with the dielectric substrate. This process can be avoided either by leaving a semitransparent vanadium layer during the oxidation process or by employing a transparent conducting coating (for example, SnO_2) as an underlayer between the substrate and vanadium. The transmission spectrum for one such sample is illustrated by curve *2* in Fig. 1. The presence of interference extrema
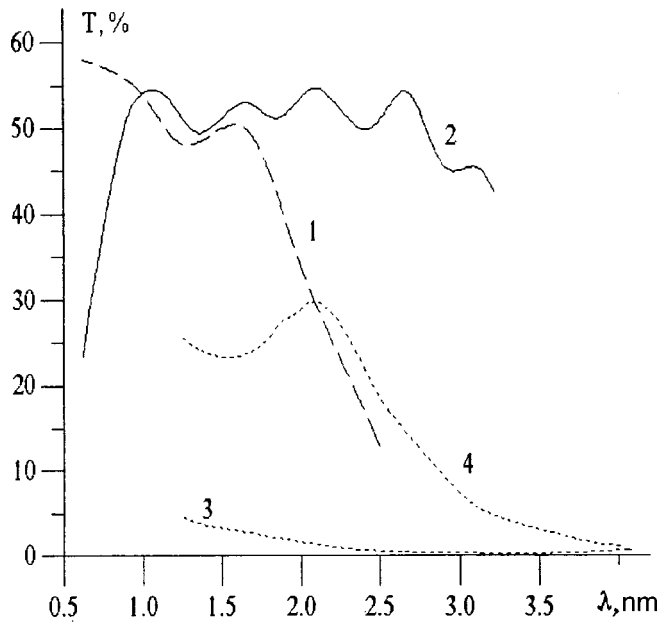
FIG. 1. Transmission spectra of anodic oxides of vanadium: *1–4* — samples obtained using different technologies (see the discussion in the text).

with $\Delta(h\nu) \sim 0.26$ eV is associated with a relatively thick ($d \sim 600$ nm) layer of tin dioxide. Spectra *2*, *3*, and *4* in Fig. 1 belong to samples of type I, i.e., samples obtained under oxidation conditions which ensure the growth of a film with a relatively large content of vanadium dioxide. This is evidenced both by the electrophysical properties of these samples and by direct investigations of the phase composition using Auger spectroscopy. It is further confirmed by the absence of the absorption characteristic of vanadium pentoxide at 2–2.5 eV on curve *2*.

It is noteworthy that it is difficult to evaluate the optical properties of the samples and their relationship to the phase composition from the transmission spectra alone. More detailed information regarding the optical properties of the material can be obtained from an analysis of its absorption spectrum $(A = 1 - T - R)$, whence the linear absorption coefficient α can easily be obtained using the Bouguer–Lambert law. However, in the case of anodic oxides of vanadium the interpretation of data on $A(\lambda)$ is complicated by the presence of additional layers (V or SnO_2), which must be introduced for the reasons discussed above. Therefore, we determined the optical constants n and k (and $\alpha = 4\pi k/\lambda$) by a method based on measurements of the reflection coefficients for polarized light R_p and R_s, from which n and k can be calculated numerically using known relations.[6] A problem similar to the inverse problem of ellipsometry is actually solved. The only difference is that R_p and R_s are measured in the experiment instead of the ellipsometric angles Ψ and Δ. The results for three samples are presented in Fig. 2a. For comparison, the figure also shows the spectra of single crystals of VO_2 (Ref. 7) and V_2O_5 (Ref. 5) and crystalline films of VO_2 (Ref. 8) (Fig. 2b).

The absorption spectrum of the samples of type I (curve *1* in Fig. 2a) corresponds to pure vanadium dioxide and qualitatively mimics the course of the $\alpha(h\nu)$ curve of a VO_2 single crystal. Therefore, the absorption band with $h\nu = 1$ eV can be assigned to the band gap of VO_2 (Ref. 1), and the relatively broad peak beginning in the vicinity of 2 eV is caused by "$2p \rightarrow 3d$" transitions.[7] This band with $h\nu = 2 - 3$ eV may not be observed in some cases, for example, in VO_2 films when the oxygen stoichiometry is varied[8] (see Fig. 2b, curve *4*). The observed differences are attributed to modification of the electron spectrum of the amorphous anodic film in comparison to a single crystal.
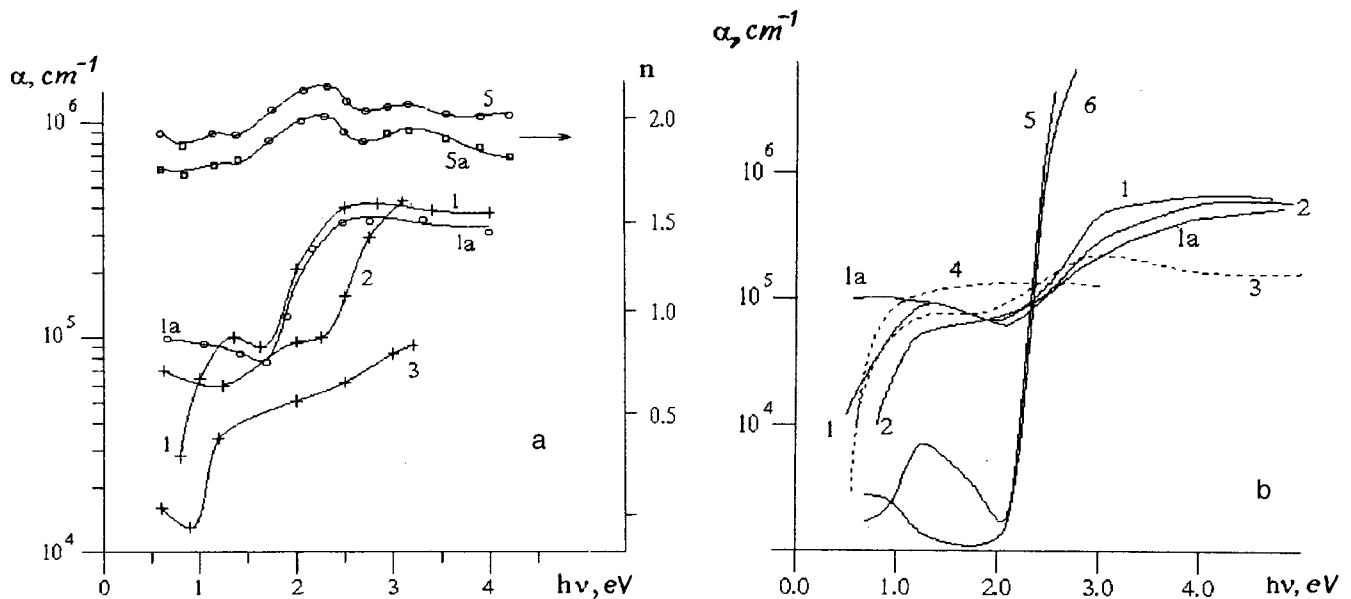
FIG. 2. a — Spectral dependence of the refractive index and the absorption coefficient of disordered VO_2: *1, 1a, 5, 5a* — sample of type I (*1, 5* — semiconductor phase, *1a, 5a* — metallic phase); *2, 3* — samples of type II. b — Spectral dependence of the absorption for vanadium oxides: *1a, 2* — single-crystal VO_2 (*1* — $E\|a_2$, *2* — $E\|a_1$, semiconductor phase; *1a* — metallic phase);[7] *3, 4* — VO_2 films (*3, 4* — films with different stoichiometry);[8] *5, 6* — single-crystal V_2O_5 (*5* — $E\|a$, *6* — $E\|c$, where E is the electric field intensity).[5] The values of α for V_2O_5 have been magnified by 100.

The transition to the samples of type II is accompanied by alteration of the absorption spectra (Fig. 2a, curves *2* and *3*), particularly a decrease in the absolute value of α and the appearance of the feature at $h\nu \sim 2.5$ eV, which are associated with the appearance of a certain quantity of a V_2O_5 phase. It is known from independent Auger electron spectroscopic and x-ray diffraction studies of the phase composition and structure of anodic oxide films on vanadium[9,10] that the samples of type I consist of amorphous vanadium dioxide with a transition layer on its outer boundary, which is enriched with oxygen and close in composition to V_2O_5. The samples of type II are also amorphous to x rays, but the outer vanadium pentoxide layer thickens when we go over to this oxidation regime. This also accounts for the observed transformation of the absorption spectra of the anodic oxide of vanadium.

Note that the use of the model of a single-layer homogeneous film to calculate the optical constants is not entirely correct in the case at hand: the values of *n* and *k* thus obtained are not true characteristics of the material, but effective global parameters. However, as can be seen from the results presented, the character of the spectral dependence of these parameters corresponds to the behavior of the true optical constants of vanadium oxides and faithfully reflects the presence and quantitative ratio between the VO_2 and V_2O_5 phases.

Thus, the anodic oxidation of vanadium gives thin films of various oxides, such as VO_2, V_2O_5, or a two-phase VO_2–V_2O_5 system. The phase composition is controlled by selecting appropriate oxidation regimes. It should be stressed that the metal–semiconductor transition is preserved in amorphous vanadium dioxide obtained by anodic oxidation, although its properties are modified somewhat in comparison to crystalline VO_2 (Ref. 10). This is important from the standpoint of technical applications of thin-film systems based on anodic oxides of vanadium and for a detailed understanding of the physical mechanism of the metal–semiconductor phase transition and the influence of structural disordering on it. In this regard there would be interest in a further investigation of the optical properties of amorphous VO_2, which could be used to evaluate the electron energy spectrum of this material in the absence of long-range crystallographic order.

[1] A. A. Bugaev, B. P. Zakharchenya, F. A. Chudnovskiĭ, *The Metal-Semiconductor Transition and Its Applications* [in Russian], Nauka, Leningrad (1979), 183 pp.

[2] H. Jerominec, F. Picard, D. Vincent, Opt. Eng. (Bellingham) **32**, 2092 (1993).

[3] J. L. Ord, S. D. Bishop, D. J. DeSmet, J. Electrochem. Soc. **138**, 208 (1991).

[4] F. A. Chudnovskii, A. L. Pergament, and G. B. Stefanovich, ''Anodic oxidation of vanadium,'' in *Seventh International Symposium of Passivity and Passivation of Metals Semiconductors. Abstracts*, Clausthal, Germany (1994), p. 149.

[5] N. Kenny *et al.*, J. Phys. Chem. Solids **27**, 1237 (1966).

[6] V. I. Pshenitsyn, M. I. Abaev, N. Yu. Lyzlov, *Ellipsometry in Physicochemical Investigations* [in Russian], Khimiya, Leningrad (1982), 152 pp.

[7] V. G. Mokerov and V. V. Saraĭkin, Fiz. Tverd. Tela (Leningrad) **18**, 1801 (1976) [Sov. Phys. Solid State **18**, 1049 (1976)].

[8] G. A. Nyberg *et al.*, Thin Solid Films **147**, 111 (1987).

[9] G. B. Stefanovich, ''The metal–semiconductor phase transition in structurally disordered vanadium dioxide,'' Dissertation for the Degree of Candidate of Physical and Mathematical Sciences, Petrozavodsk (1986), 185 pp.

[10] F. A. Chudnovskii and G. B. Stefanovich, J. Solid State Chem. **98**, 137 (1992).

Translated by P. Shelnitz

Influence of heating of the active region in InGaAsP/InP injection lasers on their spectral characteristics

L. Ya. Karachinskiĭ, A. M. Georgievskiĭ, N. A. Pikhtin, S. V. Zaĭtsev, I. S. Tarasov, and P. S. Kop'ev

A. F. Ioffe Physicotechnical Institute, Russian Academy of Sciences, St. Petersburg
(Submitted December 22, 1998)
Pis'ma Zh. Tekh. Fiz. **25**, 88–94 (April 26, 1999)

Spectral and spatial characteristics of the output of InGaAsP/InP separate-confinement double heterostructure laser are investigated. The measurements are performed in quasicontinuous and continuous pumping regimes at room temperature. These lasers are shown to be spatially single-mode over the entire working range of currents. The broadening of the longitudinal modes under quasicontinuous pumping is attributed to heating of the active region of the lasers. The pump pulse duration at which heating of the active region of the lasers can be neglected is estimated. © *1999 American Institute of Physics.* [S1063-7850(99)03204-8]

Injection heterostructure lasers based on InGaAsP quaternary solid solutions are the main sources of radiation for reading, processing, and transmitting information in fiber-optic communication lines. Attention has been focused on increasing the output power of such lasers under both continuous and pulsed pumping. The main criterion in such endeavors has been the retention of stimulated emission only in the zeroth-order transverse mode.[1]

The present work was devoted to an experimental investigation of the spectral and spatial characteristics of the emission of InGaAsP/InP injection lasers with an output wavelength equal to 1.3–1.55 μm. The purpose of this study was to demonstrate the spatially single-mode nature of the output of the lasers investigated for the case of a multiple-frequency lasing regime. The measurements were performed over a broad range of currents for the cases of both continuous and quasicontinuous pumping.

The separate-confinement double heterostructure was grown by a modified liquid-phase epitaxial method.[2] The laser design described in Ref. 3 with a mesa/stripe width $W = 4 \mu$m and a thickness of the active region equal to 200 Å was used. The laser diodes were mounted on a copper heat conductor with the stripe facing downward to ensure more efficient heat removal. The maximum radiated power in the continuous pumping regime was 50 mW at a current equal to four times the threshold value ($4I_{th}$).

The output spectra of the lasers were investigated with quasicontinuous pumping (rectangular pulses with a duration of 0.5–10 μs and an off–on time ratio of order 100) and continuous pumping. The spectra were measured above the lasing threshold at $T = 300$ K. The temperature of the heat conductor was stabilized to within ± 0.2 K.

The output spectra of the lasers recorded with pumping
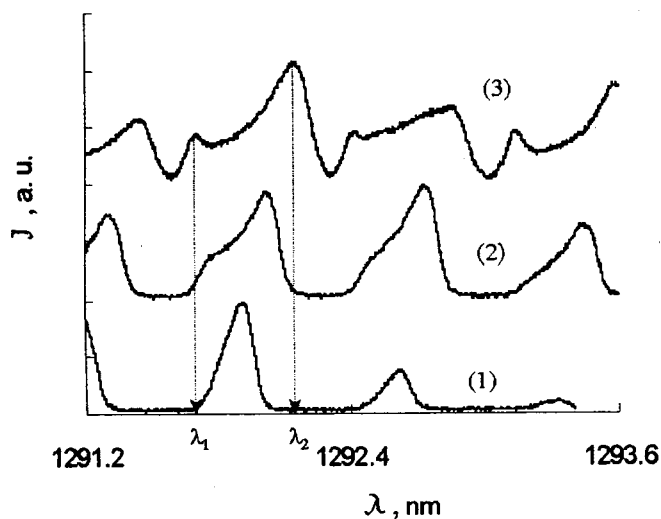
FIG. 1. Output spectra of InGaAsP/InP lasers with pumping by current pulses having a duration of 1 μs and various amplitudes: *1* — $2I_{th}$, *2* — $3I_{th}$, *3* — $4I_{th}$.
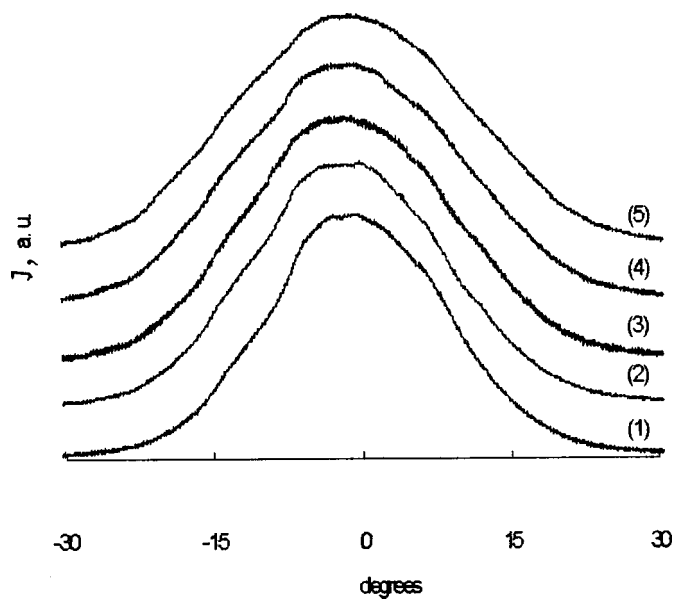
FIG. 2. Long-range radiation field of InGaASP/InP lasers in the plane of the $p-n$ junction at a current equal to $4I_{th}$ for various pump pulse durations: *1* — 0.5 μs, *2* — 1 μs, *3* — 2 μs, *4* — 4 μs, *5* — 8 μs.
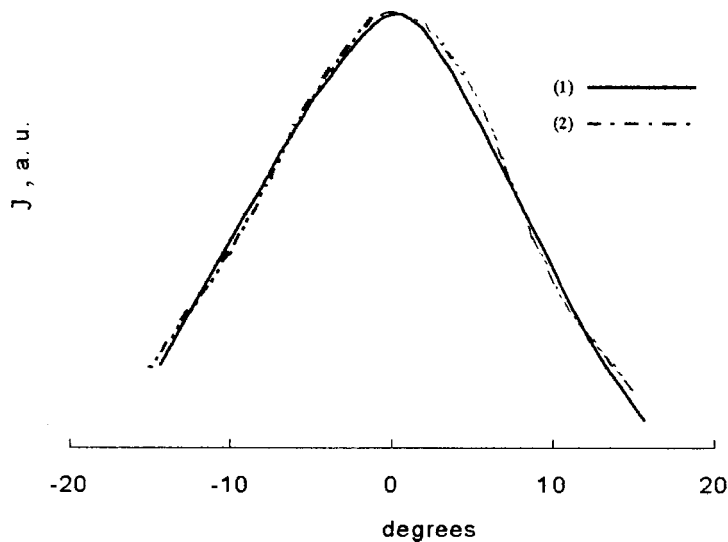
FIG. 3. Long-range radiation field of a laser with spectral resolution in the plane of the $p-n$ junction for $4I_{th}$ and a pulse duration of 1 μs at two peaks in the spectrum of the longitudinal mode (see also Fig. 1): $1 — \lambda_1$, $2 — \lambda_2$.

by current pulses having a duration of 1μs for various injection levels are shown in Fig. 1. Along with the red shift of the longitudinal modes, broadening of the modes toward the short-wavelength portion of the spectrum is observed. In addition, as the pump current is increased at a constant pulse duration, not only broadening of the mode due to displacement of the fundamental peak, but also the generation of a second maximum take place. This spectral behavior suggests that the output spectra of the lasers contain a first-order transverse mode along with the zero-order mode. However, such broadening of the longitudinal modes was not observed in the continuous pump regime. Hence it can be concluded that such changes in the form of the longitudinal mode are a consequence of dynamic processes in the laser and could be caused, say, by competition on the part of transverse modes

of the laser in establishing thermodynamic equilibrium. Measurements of long-range radiation fields of the lasers both in the plane of the $p-n$ junction and in the perpendicular plane at various pump currents and pulse durations did not reveal any variation in the output of the lasers (Fig. 2). The long-range radiation field was also investigated with spectral resolution. The monochromator was tuned to different peaks (λ_1 and λ_2 in Fig. 1) of the broadened mode. A procedure for such an investigation was proposed in Ref. 4. The measurements confirmed that the lasers investigated are spatially single-mode and that both peaks in the spectrum have the same distribution profile (Fig. 3) and correspond to the same transverse mode.

It is commonly assumed (Ref. 5, Part A) that there are two mechanisms that can alter the refractive index in a struc-
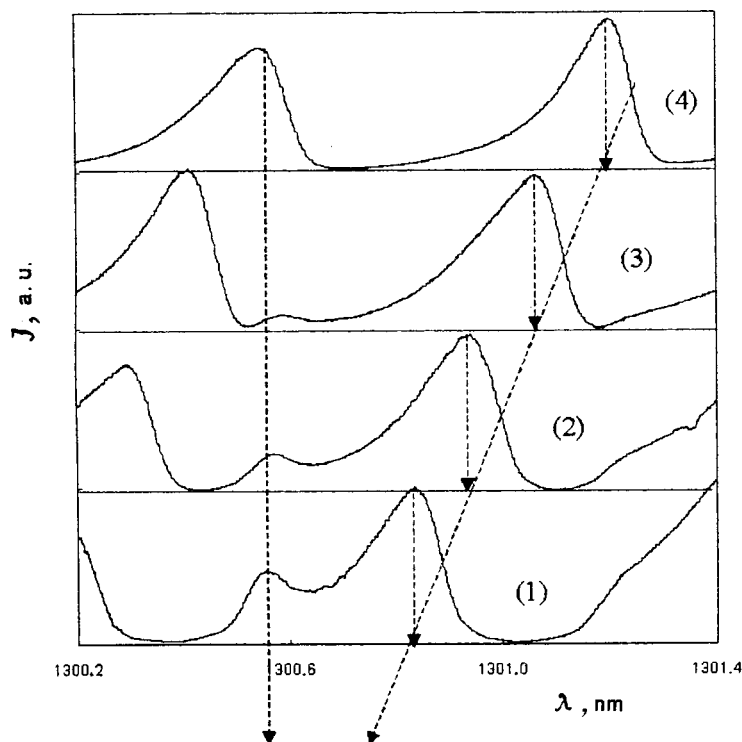
FIG. 4. Output spectra of InGaAsP/InP at a current equal to $3I_{th}$ for various pump pulse durations: $1 — 1$ μs, $2 — 2$ μs, $3 — 4$ μs, $4 — 8$ μs.
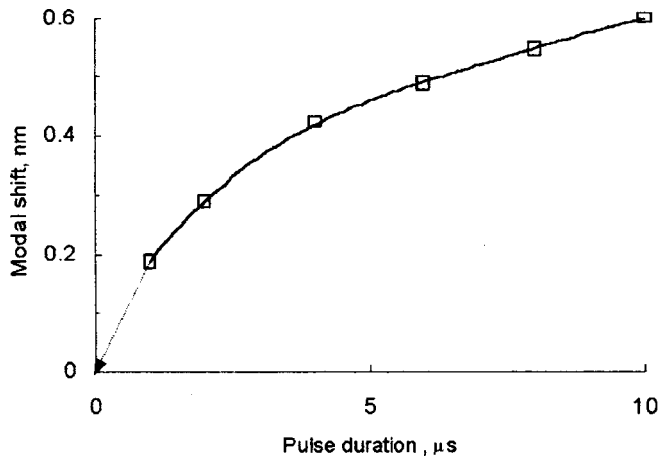
FIG. 5. Shift of the principal peak of the longitudinal mode versus pump pulse duration.

ture and, consequently, cause shifts in the longitudinal modes. The refractive index n can vary due to changes in the temperature of the laser and/or the carrier concentration. The variation of n as a result of variation of the carrier concentration (chirping) can be associated both with relaxation processes in the laser (Ref. 5, Part B) having a characteristic time much shorter than 100 ns and with self-modulation of the radiation in the laser[6] with characteristic times much shorter than 100 ps. The variation of the refractive index associated with heating can be observed over times of the order of tens of microseconds. This difference in time scales allows the influence of heating on the magnitude of the mode shift to be distinguished.

The output spectra of the lasers were measured as a function of the pump pulse duration at a constant value of the pump current (Fig. 4). The measurements were carried out with a constant off–on time ratio for the pulses to avoid displacement of the modes in the output spectrum due to variation of the constant component of the temperature of the active region of the laser. It can be seen from Fig. 4 that the magnitude of the broadening of the longitudinal mode depends on the duration of the pump pulse. The dependence of the shift of the principal peak of the longitudinal mode on pump pulse duration was investigated (Fig. 5). Since the pulse duration was varied from 0.5 to 10 μs, this shift can be attributed to a temperature effect associated with heating of the active region of the laser relative to the heat conductor.

Interpolation of the plot (Fig. 5) by an exponential function (the dotted line) gives essentially zero displacement of the peak of the longitudinal mode for a pump pulse duration tending to zero. This allows us to rule out effects associated with variation of the carrier concentration in the active region of the laser.

Figure 4 schematically shows how interpolation of the shift of the mode peak permits estimation of the times during which the shift is smaller than the width of the longitudinal mode. For this purpose, the spectra are given in a logarithmic progression with respect to the pump pulse duration in the figure. The value of 100 ns obtained for the duration at which the heating of the active region does not produce changes in the output spectrum is fully consistent with the results obtained in Ref. 7.

The results obtained allow us to conclude that the InGaAsP/InP lasers investigated are spatially single-mode in the working range of currents. The presence of the second peak in the broadened longitudinal mode is not a consequence of the presence of a first-order transverse mode in the output spectrum. It can be attributed to redistribution of the intensity between the longitudinal modes during the establishment of thermodynamic equilibrium. It was found that the broadening of the longitudinal modes with increasing pump current and with increasing pulse duration is a purely temperature-induced effect.

[1] D. Z. Garbuzov, I. É. Berishev, Yu. V. Il'in, N. D. Il'inskaya, N. A. Pikhtin, A. V. Ovchinnikov, and I. S. Tarasov, Pis'ma Zh. Tekh. Fiz. **17**(6), 17 (1991) [Sov. Tech. Phys. Lett. **17**(3), 200 (1991)].

[2] D. Z. Garbuzov, I. N. Arsentyev, A. V. Ovchinnikov, and I. S. Tarasov, in *CLEO-88, Anaheim*, Techn. Digest Ser. **7**, 396 (1988).

[3] M. A. Ivanov, Yu. V. Il'in, N. D. Il'inskaya, Yu. A. Korsakova, A. Yu. Leshko, A. V. Lunev, A. V. Lyutetskiĭ, A. V. Murashova, N. A. Pikhtin, and I. S. Tarasov, Pis'ma Zh. Tekh. Fiz. **21**(5), 70 (1995) [Tech. Phys. Lett. **21**(3), 198 (1995)].

[4] N. Yu. Gordeev, A. M. Georgievski, V. I. Kopchatov, S. V. Zaitsev, A. Yu. Egorov, A. R. Kovsh, V. M. Ustinov, A. E. Zhukov, and P. S. Kop'ev, in *Proceedings of the 5th International Symposium ''Nanostructures: Physics and Technology,''* St. Petersburg, Russia (1997), p. 183.

[5] H. C. Casey, Jr. and M. B. Panish, *Heterostructure Lasers, Part A: Fundamental Principles, Part B: Materials and Operating Characteristics*, Academic Press, New York (1978) [Russ. transl., Mir, Moscow (1981)].

[6] S. V. Zaitsev and A. M. Georgievski, in *Proceedings of the International Conference QDS'96*, Jpn. J. Appl. Phys, Part 1 **36**, 4209 (1997).

[7] N. A. Pikhtin, I. S. Tarasov, and M. A. Ivanov, Fiz. Tekh. Poluprovodn. **28**, 1983 (1994) [Semiconductors **28**, 1094 (1994)].

Translated by P. Shelnitz